Spring 1-1-2021

Dynamics And Surface Forces Experienced By An Anisotropic Colloidal Particle Near A Boundary

Aidin Rashidi
Cleveland State University

DYNAMICS AND SURFACE FORCES EXPERIENCED BY AN ANISOTROPIC COLLOIDAL PARTICLE NEAR A BOUNDARY

AIDIN RASHIDI

Bachelor of Science in Chemical Engineering
University of Tehran
November 2002

Master of Science in Chemical Engineering
Sharif University of Technology
January 2006

submitted in partial fulfillment of requirements for the degree at the

DOCTOR OF PHILOSOPHY IN CHEMICAL ENGINEERING

at the

CLEVELAND STATE UNIVERSITY

MAY 2020

We hereby approve this dissertation for

AIDIN RASHIDI

Candidate for the DOCTOR OF PHILOSOPHY in Chemical Engineering degree for the Department of Chemical and Biomedical Engineering

And CLEVELAND STATE UNIVERSITY'S

College of Graduate Studies

Christopher Wirth, Ph.D., Dissertation committee chairperson

Department of Chemical Engineering, CWRU, 05/01/2020

Nolan Holland, Ph.D., Dissertation committee member

Department of Chemical and Biomedical Engineering, 05/01/2020

Dr. Petrus S Fodor, Ph.D., Dissertation committee member

Department of Physics, 05/01/2020

Dr. Geyou Ao, Ph.D., Dissertation committee member

Department of Chemical and Biomedical Engineering, 05/01/2020

Shawn D. Ryan, Ph.D., Dissertation committee member

Department of Mathematics, 05/01/2020

Date of Defense: April 27, 2020

This student has fulfilled all requirements for the Doctor of Philosophy in Engineering degree

---

Dr. Chandra Kothapalli, Doctoral Program Director

DEDICATON

Dedicated to my beloved wife Minoo, to my beloved parents, to my supporter brothers, and my little angel Rose

ACKNOWLEDGEMENTS

I would like to express my deepest appreciation and gratitude to my advisor, Dr. Christopher Wirth, for his constant support and guidance in these years. His attitude toward science and his wonderful mentorship during my Ph.D. career affects my interests and research development. I am grateful for his help, and all the time he spent with me, improving my research, and educating me. I am pleased about spending part of my life in his lab. I would like to thank, my committee members, Dr. Nolan Holland, Dr. Petrus S Fodor, Dr. Geyou Ao, and Dr. Shawn D. Ryan, for their valuable suggestions, comments, and feedback.

I also sincerely thank Dr. Sergio Dominguez Medina, for his friendship helps and advice during the final steps of my research. I would like to thank my friend and colleague, Jiarui Yan, for his collaboration, supports, and discussions during my research. I would like to thank my friends and group members for their help during my Ph.D., Selwin Varghese, Marolla Issa, Mohammad Kalil, Sri Harsha Nuthalapati, Venkateswara Rao Kode, William Ivancic, Cornelius Obasanjo, Payton Lewis, Kenneth Gregg, and TJ Markiewicz.

I want to thank the Cleveland State University Office of Research and National Science Foundation (NSF) for their financial support.

I would like to thank my family for their unlimited support throughout my education and whole life. My parents always encourage me to achieve my goals and always supported my decisions. My brothers Arash, Farid, and Armin for their support and guidance throughout my whole life, and they are always with me. I would like to especially thank my wife, Minoo, for everything she brought to my life, for her unconditional support, for her encouragement, and for being with me these years. And

finally, I want to thank my little angel, Rose, who brought happiness and impetus to our small family.

DYNAMICS AND SURFACE FORCES EXPERIENCED BY AN ANISOTROPIC COLLOIDAL PARTICLE NEAR A BOUNDARY

AIDIN RASHIDI

ABSTRACT

Colloidal interactions play an important role in determining the macroscopic properties of different materials. Recent work in this area has focused on the role anisotropic particles play in these materials. This thesis summarizes work conducted on the dynamics and interactions of an anisotropic colloid particle near a solid wall. Specifically, the methodology for conducting Total Internal Reflection Microscopy (TIRM) on anisotropic colloidal systems near a boundary was developed. This new method is called "Scattering Morphology Resolved – TIRM" (SMR-TIRM).

Simulations of the Brownian motion of a sphere comprising hemispheres of different composition (i.e. a Janus particle) very near a wall were conducted. Trajectories obtained from these simulations were used to construct 3D potential energy landscapes. Results showed that the potential energy landscape of a Janus sphere has a transition region at the location of the boundary between the two Janus halves, which depended on the relative zeta potential magnitude. In this thesis, an experimental technique for the direct and local measure of cap thickness of a coated Janus particle was summarized. It is found that the cap varied in thickness continuously along the perimeter of the particle. To better understand the impact of the coating on the dynamics of Janus particle, Brownian dynamics simulations to predict the translational and rotational fluctuations of a Janus sphere with a cap of non-matching density near a boundary was utilized. The simulation results show that the presence of the cap significantly impacts the rotational dynamics of the particle as a consequence of gravitational torque.

In the last part of this thesis, the SMR-TIRM was used to map scattering from ellipsoid particles. The hypothesis driving this work was that evanescent wave scattering from an ellipsoidal particle depended on both the aspect ratio and orientation. Analysis of the light scattered from the particle showed that both ellipticity and directionality correlated with particle orientation and aspect ratio. In principle, these relationships will allow tracking of the particle's position and orientation via the scattered light morphology.

TABLE OF CONTENTS

LIST OF TABLES

Table Page

LIST OF FIGURES

CHAPTER I

INTRODUCTION

Micrometer scale colloidal particles that are regularly found in nature and technologically relevant applications have a significant impact on various aspects of our life. These types of systems consist of suspended macromolecules or particles in another continuous phase. These suspended particles are often in the range of a nanometer to a micrometer. These particles are in a size range larger than molecules but still sufficiently small that are under the influence of thermal agitation. One suitable technical definition of a colloid can be found in a text by Dennis Prieve as the following:

"A state of mixtures of two immiscible components in which one component is finely divided as bubbles, drops or particles in a second (usually continuous) phase."[1]

Michael Faraday, in 1857, was the first to synthesize colloidal particles, which was a finely divided gold dispersion. He investigated the optical properties of these materials, and since then, significant effort has been invested in research, development, and application of colloidal particles. Note, however, that Faraday did not use the term colloid in his lecture and publication. Thomas Graham later coined the term colloid in 1861[2].

Colloidal particles interact with each other via physiochemical or hydrodynamic mediated interactions in a range of applications such as coatings, filtration, food, cosmetics, home care, personal care, and printing; or engineering applications such as drug delivery, optical display[3], self-assembly[4], microsensors[5], and microfluidic devices[6] and designing foams and emulsions (and their effect on their stabilization), biological adhesion and biofouling[7]. Based on the chemical and physical features of the colloidal particles, they are classified as isotropic or anisotropic particles. The term 'anisotropic' typically refers to a particle having a property that is non-uniform along its surface, while 'isotropic' refers to a particle having no such non-uniform property. In other words, an isotropic particle can be mechanically, geometrically, electrically, or chemically uniform. Isotropic particles served as excellent models systems for researchers over the last few decades. For example, researchers have used an AC or DC electric field to control spherical particles at infinite dilution and also make colloidal crystals on top of an electrode at more concentrated conditions[8–10]. During assembly and control, the mechanisms for motion isotropic particles was primarily a consequence of electroosmotic, electrophoresis, and dielectrophoretic flow. Moreover, significant studies on the behavior of spherical particles such as rotational[11] and translational displacement[12], their interaction with other particles or the neighborhood environment[13] were done. These studies were about a single or concentrated spherical particles dispersed in the bulk[14], near a wall[15] and at the interface[16].

Anisotropic colloid particles have recently gained interest among scientists for both fundamental and industrially relevant applications. An anisotropic particle has a chemical, mechanical, electrical, or geometrical property variation across the surface of the particle. Many micrometer-scale anisotropic colloidal assemblies can be actuated to control their optical, transport, and mechanical properties. Janus particles are one

example of an anisotropic particle. Janus particles, which have halves with dissimilar properties, have been studied in many interfacial interactions. In one study scientists synthesized colloidal muscle-like fibers of Janus ellipsoids by self-assembly[17]. These structures were then actuated to stretch, but then returned to the original structure because of a shape memory feature. Also, Tanaka et al. used mushroom-like Janus polymeric particles (poly(methyl methacrylate) (PMMA)/poly(styrene-2-(2-bromoisobutyryloxy)ethyl methacrylate)-graft-poly(2-(dimethylamino)ethyl methacrylate) (PDM)) as a particle surfactant to stabilize 1-octanol-in-water emulsion droplets[18]. This work complements other studies that showed how bimetallic Janus particles were able to decrease interfacial tension at the oil-water interface more than uniform surfactants[19]. Further, Janus particles were used as stabilizers in the fabrication of polystyrene (PS) beads by emulsion polymerization of styrene and butyl acrylate. The Janus particle in this process had polybutadiene as a core that was covered with PMAA (poly(methacrylic acid)) and PS. The high adsorption energy of this Janus particle as compared to standard polymeric surfactants make them less probable to be aggregated[20]. In another study, Yang et al[21] synthesized a silica-based Janus particle. This Janus particle was made hydrophilic via modification with an amino-containing silane agent and hydrophobic via modification with a silane coupling agent with different carbon chain lengths. They used this Janus particle as an amphiphile to strongly stabilized foam for drilling a high temperature and high calcium geothermal well. Non-spherical, geometrically anisotropy particles are another type of anisotropic particles. In a research[22], scientists were able to synthesize geometrically anisotropic polymer particles. In this study, they synthesized various porous polymers via radical polymerization of methylmethacrylate and styrene. These types of non-spherical polymers can be used for sensor and optoelectronic applications in the future. As

assembling of geometrically anisotropic particles at the interface can be tuned, these types of particles can be used for emulsion foam stabilization. Many types of non-spherical colloidal particles such as polystyrene ellipsoids[23], graphene oxide sheets[24], silica rods[25], cellulose nanocrystals[26], and many other materials have been used as an emulsifier. In a study, Madivala et al[23] used hydrophobic prolate polystyrene ellipsoids to stabilize water-in-oil and oil-in-water emulsions. Their research shows that the aspect ratio and coverage percentage impact the interfacial viscoelastic properties and the surface rheological properties. The shape of anisotropic particles can control the stability of Pickering emulsions. Research describes how the graphene oxide sheet, which is an amphiphilic material with a hydrophobic plane and hydrophilic edges, can act as a surfactant to stabilize Pickering emulsions[24]. The researchers show that the amphiphilicity of the system is controllable by the size of the graphene oxide sheet. In **Figure 1.1**, I show some of the Janus particles, scientist have developed for various purposes.

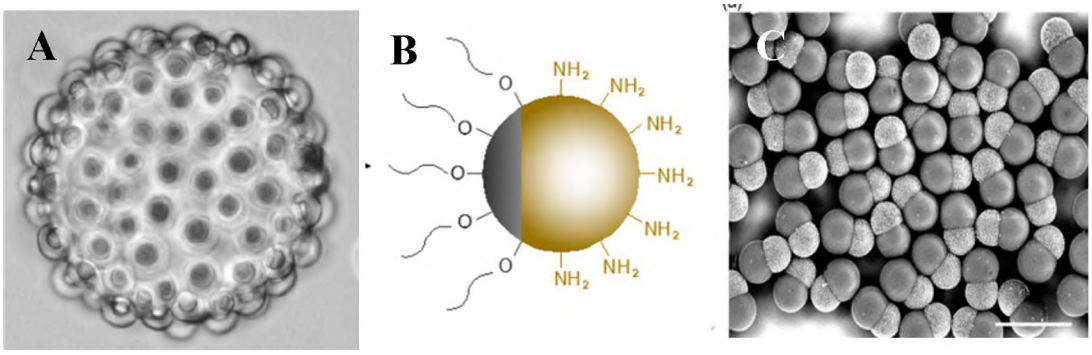

Figure 1.1. Sample of anisotropic particles, (A) Octanol-in-water emulsion droplets stabilized by the Janus particles (PMMA and PDM combination) (Reprinted with permission from ref. 18. Copyright (2010) American Chemical Society), (B) Highly stabilized foam by adding amphiphilic Janus particles for drilling (NH2-SiO2-12C) (Reprinted with permission from ref. 21. Copyright (2019) American Chemical Society), (C) Metal−organic hybrid particles (Reprinted with permission from ref. 19. Copyright (2014) American Chemical Society).

Interaction forces between colloidal particles play an important role in determining the properties and performance of a variety of materials, including

stability, shelf life, and rheology. Thus, measuring and prediction of colloidal interactions is critical to engineering these products. For example, the transport, interaction, and deposition of anisotropic particles in confined geometries such as porous media is an important challenge found in biology and drug delivery within tissues, biofilm formation, the production of safe drinking water, membrane filtering, and deposition of particles on substrates of particle-based surface coatings[7,27–30]. As noted earlier, a crucial feature of colloidal particles that dictate behavior are the surface forces experienced by that particle in its local environment. Surface forces are important for two reasons in typical applications. First, colloidal systems have a large surface area to volume ratio. Second, surface forces are crucial because colloids often interact with boundaries, for instance, in filtration, porous media, or coating applications. Surface forces are typically split into two general categories depending on whether the forces are path independent or dependent. Conservative forces are path independent, while non-conservative or dissipative forces are path-dependent. Commonly encountered conservative forces are electrostatic double-layer repulsion, van der Waals dispersion interactions, solvation or hydration force, hydrophobic force, depletion interaction, steric force, and gravity. Conservative forces most often arise from physiochemical effects. Fluid friction or hydrodynamic forces are non-conservative forces experienced by particles, most relevant when the particle is nearby a substrate or another particle.

Quantitative descriptions of these various forces and associated measurement tools help to engineer and develop new and better-performing materials by tuning these colloidal interactions. Multiple experimental techniques, including atomic force microscopy (AFM), the surface force apparatus (SFA), confocal microscopy, holographic microscopy, and Total Internal Reflection Microscopy (TIRM), have been

developed over the past few decades to probe these interactions. AFM and SFA, modified with a colloidal probe, are robust techniques that have been widely adopted to measure surface forces between the probe and a substrate[31]. Similarly, TIRM has been developed to measure the surface force experienced by a single colloidal particle immersed in a liquid nearby, but not adhered to, a substrate[32]. TIRM tends to be more sensitive than AFM and SFA because TIRM uses a 'thermal' energy scale (i.e., ~ kT, k is Boltzmann's constant).

In contrast, AFM and SFA operate on a mechanical energy scale (i.e., ~ $k_S X^2/2$, k_S is the cantilever spring constant)[31]. Confocal microscopy is another technique that has been used to track colloidal particles and measure their interactions[33–36], but high time and spatial resolution typically cannot be achieved simultaneously. This problem limits the technique to relatively slow dynamics or highly viscous solvents. Holographic microscopy captures a 2D hologram from a particle. The hologram encodes the 3D positional information of that particle. Appropriate analysis of the hologram allows the experimenter to recover this position information[37]. Recent work used this technique for the dynamic tracking of colloidal particles, but in general, the image analysis is complicated and limits the robustness of the technique. Recently, the interactions and dynamics of nano- to micrometer scale "complex or anisotropic" colloidal particles have become of interest. Unfortunately, the developed measurement techniques for surface forces such as AFM, confocal microscopy, and conventional TIRM are typically only suitable for isotropic particles.

Note how the interaction of anisotropic particles is more complicated as compared to isotropic particles. As the physical and chemical properties of these particles are asymmetric, interactions will depend not only on separation distance, but also orientation. Given the complexity of these interactions, even for the simplest

anisotropic particles, the dependence of interaction energies on different anisotropic features, such as non-uniform surface chemistry or geometry, are not readily available for most systems. Thus, developing a technique to measure the interaction of anisotropic particles is crucial.

One fundamental goal of my research group's efforts is to develop an experimental methodology and design for conducting TIRM on anisotropic particles. My role, as detailed in this thesis, was to develop the methodology for applying TIRM to two model anisotropic colloid particles, namely spherical Janus particles and ellipsoids. This effort consisted of both simulation and experimental work to understand either the dynamic behavior of Janus particles near a boundary or how ellipsoidal particles scatter light from an evanescent wave.

Chapter II presents results from Brownian dynamics simulations of a Janus sphere very near a boundary at conditions similar to those of a TIRM experiment[38]. I chose to initially work with Janus spheres because they are the closest departure from an isotropic sphere. In this part, simulations of the trajectory of a Janus sphere with cap density matching that of the base particle very near a boundary were used to construct 3D potential energy landscapes that were subsequently used to infer particle and solution properties, as would be done in a TIRM measurement. ***The main intellectual contribution from this effort was to demonstrate how to assemble a potential energy profile from multivariable trajectory data.***

Chapter III details an experimental technique that utilizes focused ion beam slicing, image analysis, and results for the direct and local measure of cap thickness for Janus spheres with a gold cap[39]. This technique demonstrates a feasible route for direct measurement of Janus particle cap thickness. ***The main intellectual contribution from***

this effort was to show, for the first time, how the thickness of a cap on a Janus particle will vary along its contour.

Chapter IV details more work with a Brownian dynamics simulation tool to predict the translational and rotational fluctuations of a Janus sphere with a cap of non-matching density near a boundary[40]. The presence of the cap significantly impacted the rotational dynamics of the particle as a consequence of gravitational torque at experimentally relevant conditions. In this study, the histogram landscape of translation and rotation of the particle were inverted to obtain the potential energy landscapes, providing a roadmap for TIRM experimental data to be interpreted. ***The main intellectual contribution from this effort was to demonstrate first how significant of an impact the (non-density matched) cap has on Janus particle dynamics and second how to assemble a potential energy profile from multivariable trajectory data in which there was a torque that depended on orientation.***

Chapter V describes in detail how an ellipsoidal particle will scatter light from an evanescent wave at fixed height and orientation. This information is necessary to evaluate the essential features of scattering during TIRM and to generate an experimental approach to probe the orientation and separation distance of the particle. In this part of the thesis I explained a working hypothesis I used to develop the new TIRM technique which is called "Scattering Morphology Resolved – TIRM" (SMR – TIRM) as well as a methodology to create this technique. ***The main intellectual contribution from this effort was to first define the morphology features needed to evaluate scattering from an anisotropic particle and second to show how those features depend on particle aspect ratio, size, and orientation.***

Chapter VI states conclusions and the main paths suitable for future work. Briefly the conclusion regarding investigation of dynamics of matching and non-

matching density of coated the Janus particles near a boundary is presented. Also, result of 3D potential energy profile of Janus particles near a boundary is presented. Furthermore, an algorithm to calculate potential energy landscape for an ellipsoidal particle is proposed. I recommended some ideas including improving experimental mapping process, increasing the data range for the mapping process, and evaluating dynamics of a coated active particle near a wall at different operational conditions.

CHAPTER II

MOTION OF A JANUS PARTICLE VERY NEAR A WALL

2.1 Introduction

Nanometer to micrometer scale colloidal particles are ubiquitous to consumer products, coatings, cosmetics, large and small-scale industrial processes. Colloidal particles dispersed in a liquid interact via surface forces to form microstructure that will have a profound impact on the mechanics and rheology of that liquid. Surface forces arise from physiochemical properties of the particle and liquid medium, such as surface charge, solution pH and salinity, and the presence of other entities, such as surfactant or polymer dispersed in the liquid.[41] Multiple experimental techniques, including Atomic Force Microscopy (AFM), the Surface Force Apparatus (SFA), and Total Internal Reflection Microscopy (TIRM), have been developed over the past few decades to probe these interactions, which could be as weak as a few ~kT. SFA and AFM, modified with a colloidal probe, are robust techniques that have been widely adopted to measure surface forces between the probe and a substrate.[42,43] Similarly, TIRM has been developed to measure the surface force experienced by a single colloidal particle immersed in a liquid nearby, but not adhered to, a substrate. The essence of TIRM is the measurement of stochastic "Brownian" fluctuations of the colloidal particle normal to the nearby substrate.[32,44,45] TIRM tends to be more sensitive than AFM and SFA because TIRM uses a 'thermal' energy scale (i.e. ~ kT), whereas

AFM and SFA operate on a mechanical energy scale (i.e. ~ $k_S X^2/2$, k_S is the cantilever spring constant).

TIRM, employing spherical particles with uniform surface chemistry and composition, has been used to accurately measure both equilibrium and non-equilibrium ~kT scale colloidal interactions, including electrostatic double layer repulsion,[46] van der Waals attraction,[47] steric interactions,[48] depletion interactions,[49] electrophoretic forces,[50] hydrodynamic interactions,[15] and even the Casimir interaction.[51] Recently, the TIRM technique has even been developed to measure interactions of colloidal particles and oil droplets near a water-oil interface, thereby extending the technique to liquid-liquid interfaces from conventional liquid-solid interfaces.[52] These studies illustrate the utility of TIRM as a tool, which complements SFA and AFM, for surface force measurement. One current limitation of the TIRM technique is that only optically isotropic particles (i.e. sphere of uniform composition) have been used for measurements, with the exception of one example where the particle was small enough to assume that anisotropy did not impact scattering.[53] There has been no published experimental technology or methodology development that would allow for the application of TIRM to geometrically or chemically anisotropic colloidal particles.

Surface forces experienced by anisotropic particles are relevant to many natural and synthetic systems, for instance carbon nanotubes, graphene sheets, red blood cells, and clay particles, which are all anisotropic. Anisotropic particles can be locally hard or soft, may have complicated shapes, or have a non-uniform surface charge distribution.[54] Many groups are now able to synthesize model anisotropic particles, such as spherical and ellipsoidal "Janus" particles.[55–57] A significant amount of work has focused on the directed self-assembly of Janus spheres or ellipsoids with different

shapes and dissimilar properties.[17,58–60] Surface forces, and associated particle dynamics, are of central importance to the directed self-assembly and ultimate utility of these materials. Non-uniform or non-symmetric physical and chemical properties typically induce spatially and orientationally dependent colloidal interactions, thereby complicating the measurement, prediction, and control of such interactions among anisotropic particles. Researchers have proposed techniques for tracking the rotational motion of a cluster of colloidal particles[61], copper oxide nanorods[62] and micrometric wires by using holographic video microscopy and 2D video microscopy. Recent work has even demonstrated how to account for particle curvature when calculating surface forces for a non-spherical particle.[63] However, there is currently no experimental technique or methodology for sensitively measuring the surface forces between anisotropic particles and a nearby substrate.

We are working to fill this need by developing the experimental technology, methodology, and design for conducting TIRM on anisotropic particles, including spheroids of arbitrary shape and spheres of non-uniform surface chemistry. In this article, I present results from Brownian dynamics simulations of a Janus sphere very near a boundary at conditions similar to those of a TIRM experiment. An in-house made MATLAB code was developed for this purpose (APPENDIX 2.1). I chose to initially work with Janus spheres because they are the closest departure from an isotropic sphere. As was done previously for isotropic particles,[64] the goal of these simulations was to generate *in silico* data similar to that obtained during a TIRM experiment, allowing us to probe and optimize TIRM parameters that would be implemented for a Janus particle with hemispheres of unequal zeta potential, develop a methodology for calculating potential energy landscapes from multivariable trajectory data, and determine how the interpretation of conservative forces may be impacted by non-equilibrium dynamics. I

combined a well-established Brownian Dynamics stepping algorithm for uncoupled rotational-translational Langevin equation with a meshing technique for application to a Janus sphere. I then applied this meshing technique to simulate the position and rotational trajectories of a spherical Janus particle with unequal zeta potential on each hemisphere. I utilized the simulated position and orientation observations to assemble a 3D potential energy landscape from these multivariable data, a process required for a TIRM experiment. Finally, I used these energy landscapes to calculate system properties, including hemisphere zeta potential, particle size, and the solution's Debye length. The described simulation tool, associated results, and data analysis is the first step in methodology development for applying TIRM to an anisotropic particle.

2.2 Theory

2.2.1 Conservative colloidal interactions

Consider the particle of radius a and separation distance h shown in **Figure 2.1A** The particle is nearby, but not adhered to, the substrate and will remain mobile at conditions where there is a strong electrostatic repulsion between it and the neighboring substrate. The electrostatic repulsive force depends on the solution's Debye length, the size of the particle, and the particle's and substrate's Stern potential, which is typically equated with the zeta potential of each surface. In addition to electrostatic repulsion, I also consider the weight of the particle because experiments typically are conducted on polystyrene or silica particles that have a density not matched water. The colloidal interaction force F_c, which is equal to the negative gradient of the interaction energy, between a spherical particle and a flat plate is given by:

$$F_c = -\frac{d\phi_c(h)}{dh} = \underbrace{\kappa B \exp(-\kappa h)}_{\text{Electrostatic}} - \underbrace{\frac{4}{3}\pi a^3(\rho_p - \rho_f)g}_{\text{Gravitational}} \quad (2.1)$$

$$B = 64\pi\varepsilon_0\varepsilon_f a\left(\frac{kT}{e}\right)^2 tanh\left(\frac{e\zeta_s}{4kT}\right)\ tanh\left(\frac{e\zeta_p}{4kT}\right) \quad (2.2)$$

$$\kappa = \sqrt{\frac{2e^2 C_\infty}{\varepsilon_0\varepsilon_f kT}} \quad (2.3)$$

where κ is the solution's Debye length, B is the electrostatic charge parameter, ρ_p and ρ_f are density of the particle and substrate respectively, g is gravitational acceleration, ε_0 is the electric permittivity of vacuum, ε_f is the relative permittivity of water, e is the charge on an electron, ζ_s and ζ_p are the zeta potentials of the surface and particle respectively, and C_∞ is electrolyte concentration in the bulk. Note that the expressions above can be directly applied to a sphere of uniform zeta potential, but not for the Janus sphere shown in **Figure 2.1A** because of the additional dependence of F_c on θ'. We later describe a meshing technique to account for such a dependence.

2.2.2 Hydrodynamic drag on a particle near a boundary

A TIRM experiment tracks the stochastic fluctuations of a particle in the direction normal to the nearby substrate (z-axis in Figure 2.1A). The translational and rotaional diffusion coefficients, D_z and $D_{r\theta}$ respectively, of a particle decrease when it approaches a boundary due to an increase in the hydrodynamic drag force. The increase in translational hydrodynamic drag for the slow motion of a sphere approaching a wall is well-known and has been confirmed experimentally.[65–67] Note that both normal and rotational mobility will decrease due to the wall. The translational diffusion coefficient for a spherical particle in the direction normal to the boundary is:

$$D_z = \frac{kT}{f_\infty} q(h) = \frac{kT}{6\pi\eta a} q(h) \quad (2.4)$$

$$q(h) = \frac{6h^2 + 2ha}{6h^2 + 9ha + 2a^2} \quad (2.5)$$

where f_∞ is the linear quasi-steady Stokes drag coefficient $f_\infty = 6\pi\eta a$, η is the fluid viscosity, and q(h) is the wall correction factor.

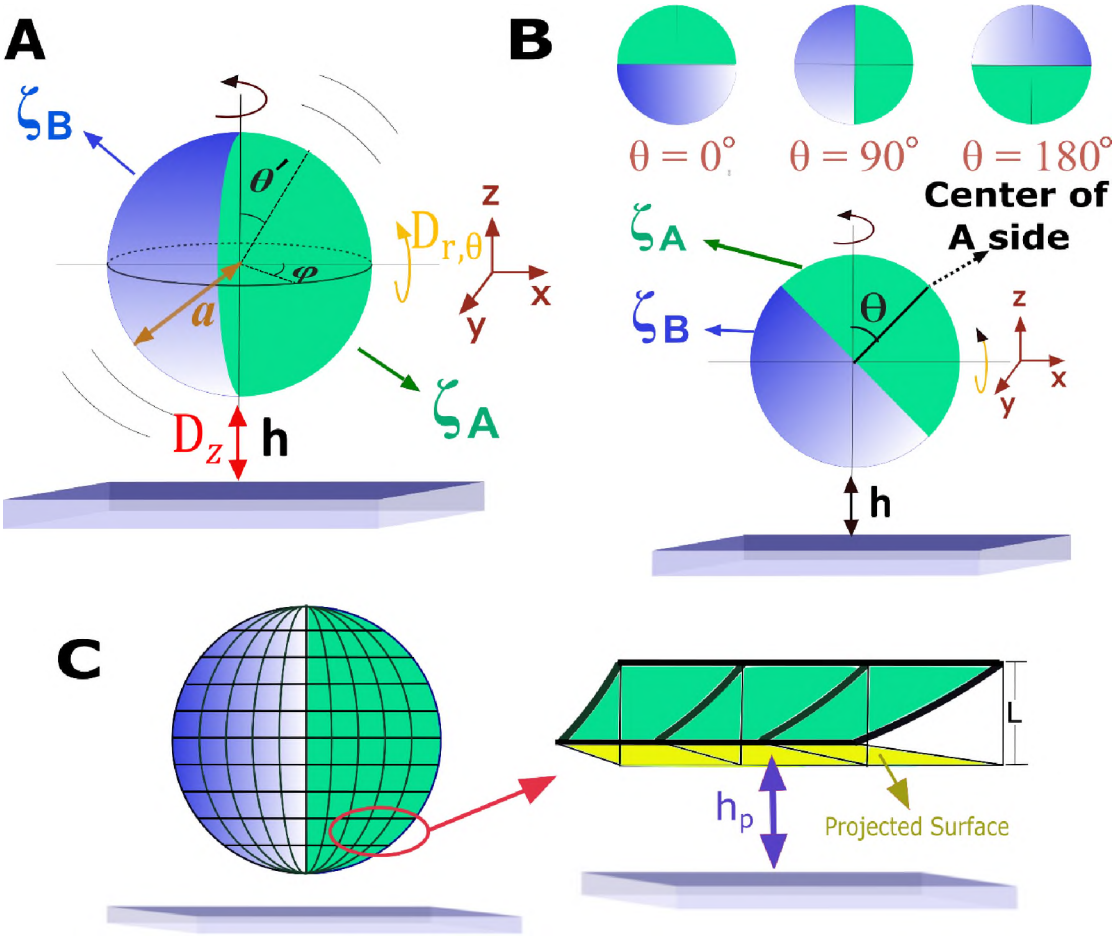

Figure 2.1. (A) Illustration of a spherical Janus Particle with radius a and hemispheres of zeta potential A ζ_A and B ζ_B. The particle is separated a distance h from the nearby boundary. θ' rotation is defined as in the axis parallel to the boundary, while φ rotation is defined as in the axis perpendicular to the boundary. (B) Schematic representation of orientation of spherical Janus particle. The angle θ is defined between the center of side A and the axis perpendicular to the substrate, such that when the center of side 'B' is downward, θ = 0°, and when the center of side 'A' is downward, θ = 180°. θ = 90° occurs when the center of the transition is pointed downward. (C) Particle with surface meshing to account for non-uniform zeta potential. The projected surface from each mesh point was used to calculate the interaction force between the sphere and substrate, which is similar to the Derjaguin approximation.

The exact analytical solution of the Stokes equation for the rotation of a sphere around an axis parallel to a substrate in a creeping flow when the sphere-wall gap is very small has been derived by Dean and O'Neill.[68] Liu et al [12] reported an approximate

solution by Maude[69] for this analytical problem close to the boundary. Goldman[70,71] plotted graphically three different approximations and an exact (corrected Dean and O'Neill) result of the Dean and O'Neill solution. As in our system the dimensionless gap range is between 0.015 and 0.15, the Maude approximation solution is not applicable. To use exact numerical solution (corrected Dean and O'Neill) in our range, I fitted these data in the appropriate range. The fitted expressions are:

$$D_{r,\theta} = \frac{kT}{f_{r,\infty}} / q^{\theta}(h) = \frac{kT}{8\pi\eta a^3} / q^{\theta}(h) \tag{2.6}$$

$$q^{\theta}(h) = 0.9641 \left(\frac{h}{a}\right)^{-0.1815} \tag{2.7}$$

2.2.3 Implementing Brownian dynamic simulations

The motion of a Brownian particle very near a boundary is described by a force balance on the particle with the inclusion of a stochastically fluctuating force. At small Reynolds number, the inertial term in the force balance is zero and there is a well-known numerical solution of the Langevin equation by Ermak and McCammon.[72] The trajectory of a single particle was predicted via:

$$h(t + \Delta t) = h(t) + \frac{dD_z}{dh}\Delta t + \frac{D_z}{kT}F\Delta t + H(\Delta t) \tag{2.8}$$

In this algorithm, h is calculated in each forward time step and $H(\Delta t)$ is a Gaussian random height displacement variable satisfying $\langle H \rangle = 0$. The variance of this noise is $\langle H^2 \rangle = 2D_z\Delta t$. These expressions satisfy the dissipation theorem that defines particle-fluid viscous dissipation as the origin of particle fluctuations in the suspending fluid.[73] Note that **Equation 2.8** allows for the friction coefficient to depend on height. Previous work has shown that if height dependency of the friction coefficient is assumed to be independent of the separation height there will be a systematic error between the real and simulated potential energy profiles.[64] Two conditions must be satisfied to use the stepping algorithm. One is that the time step is sufficiently short

such that force, height, and all other calculated properties are constant. The second condition is that the time step is much longer than the momentum relaxation time of the particle.

The rotational trajectory was predicted with an expression analogous to **Equation 8**. The rotational stepping algorithm is:[74,75]

$$\theta(t + \Delta t) = \theta(t) + \frac{D_{r,\theta} T_{exin} \Delta t}{kT} + G(\Delta t) \quad (2.9)$$

The $G(\Delta t)$ term is stochastic Gaussian standard Brownian rotational displacement. This random noise is defined by the following variance $\langle G^2 \rangle = 2D_{r,\theta}\Delta t$. The T_{exin} term accounts for the time-dependent internal and external torques. External torques may include contributions from both electrostatics and gravity. Electrostatic torque will arise because of the mismatch in electrostatic repulsion very near the boundary between hemispheres A and B. Gravitational torque will arise because of the mismatch in densities of the base particle and cap material. Common examples of cap materials on polystyrene ($\rho = 1.055$ g/cm^3) or silica ($\rho = 2.65$ g/cm^3) particles are gold ($\rho = 19.32$ g/cm^3)[5], silica[76], and carbon[77]. These phenomena will induce torques that will make the middle term on the right-hand side of **Equation 2.9** non-zero. I conducted simulations to isolate the effects of either electrostatic or gravitational torque. I found that electrostatic torque had a negligible effect, with an average root mean squared error of 0.0642 kT when compared with results neglecting the effect. However, I did find that gravitational torque had a significant impact on the rotational sampling of a Janus particle and, consequently, the potential energy landscape. Thus, the cap weight and thickness (even for very thin caps) will affect the potential energy landscape. Herein, I assumed that the time dependent internal and external torques are zero and, thus, our results are applicable only to systems where the cap density matches that of the base particle. Given the very large parameter space, including cap density and thickness, I

plan on exploring the influence of cap weight on rotational dynamics of a Janus particle in a future contribution. All simulations presented in this article were for a polystyrene particle with a cap of matching density.

Note from **Figure 2.1A** that the force felt by the Janus particle will be axisymmetric about φ, the axis perpendicular to the substrate. I utilized this symmetry to make the simulation more efficient by only stepping orientation fluctuations in θ' and ignoring rotation of the particle in the φ direction. **Equations 2.8 & 2.9** were executed for either 2.4 x 10^6 or 4.8 x 10^6-time steps for a single simulation, with each time step Δt = 5 ms, unless otherwise noted. A single simulation provides trajectories in both h and θ', which were then used to prepare histograms as described later in this article. Subsequently, potential energy profiles were calculated from these histograms. The potential energy profiles and landscapes presented later in this article were obtained from averaging ten simulations. At each bin height, the mean and standard deviation of potential energy was calculated and compared with the analytical potential energy profile. The convergence criteria for each height is satisfied if the standard deviation and difference between the meshing method simulation (mean point of 10 sets of simulations) and true potential energy profile are less than 0.3kT. Note that this convergence criteria is similar to that recommended by Sholl et. al.[64]

2.2.4 Accounting for non-uniform surface charge with meshing method

The stepping algorithms described above were implemented for a spherical Janus particle of different zeta potentials on each hemisphere. The sphere was meshed into small parts in both the polar angle θ' and azimuthal angle φ (**Figure 2.1C**) to account for the change in zeta potential upon Janus particle rotation in the θ' direction. After projecting the small curved surfaces parallel to the substrate, the electrostatic double-layer force between each projected flat surface and the substrate were calculated. In the

case of monovalent salt, the electrostatic double layer repulsion pressure of two flat parallel surfaces is:

$$P_{dL}(i) = 64C_{\infty}kT\tanh\left(\frac{e\zeta_s}{4kT}\right)\ \tanh\left(\frac{e\zeta_{mp}(i)}{4kT}\right)\exp\left(-\kappa h_{dL}(i)\right) \quad (2.10)$$

where ζ_s and ζ_{mp} are the zeta potential of the substrate and flat projected surface of the mesh point i. The electric double layer repulsion force between each mesh point and the substrate is proportional to the product of the pressure and the projected surface area for each mesh point:

$$F_{dL}(i) = P_{dL}(i)\,A(i) \quad (2.11)$$

The effective height (h_{dL}) in the pressure equation was equal to the mid-point of the mesh surface height:

$$h_{dL} = h_p + L/2 \quad (2.12)$$

Finally, the total electrostatic double layer repulsion force between the particle and the substrate was calculated by summing the forces at each mesh point:

$$F_{dL-total} = \sum F_{dL}(i) \quad (2.13)$$

Once implemented, the meshing method together with the Brownian Dynamics simulation allows for a direct prediction of particle height and orientation evolving in time very near a boundary for a Janus particle of unequal zeta potential.

The optimum mesh size was determined by comparing the electrostatic portion of the potential energy profile as calculated from **Equation 2.1** (*i.e.* non-meshed particle) to that calculated from **Equation 2.13** (*i.e.* meshed particle) for different mesh sizes, but with uniform zeta potential. The gravitational portion of the force calculation was unnecessary for this comparison because the gravitational force depends on neither the zeta potential of the particle nor the height of the mesh point. I found that increasing the number of mesh points decreased the error in the comparison between a non-meshed and meshed particle. A particle with 30 x 30 meshing (900 total points with 30 points

in θ' and 30 points in φ) had nearly a 22% error when compared with a non-meshed particle with the same properties. A particle with 100 x 100 meshing had less than 1% error when compared with a non-meshed particle with the same properties. **Table 2.1** summarizes these results. I chose a particle with 100 x 100 meshing to have acceptable numerical error for our purposes as using more mesh points severely decreased computational speed, yet did not appreciably increase accuracy.

Table 2.1: Error associated with varying discretization in meshing. Comparing of double-layer repulsion force for optimum mesh size calculations.

Mesh Size	Non-meshed Particle Electrostatic Force (N)	Meshed Particle Electrostatic Force (N)	Error %
20×20	9.68e-16	1.41e-15	46.114
30×30	9.68e-16	9.68e-16	22.013
60×60	9.68e-16	1.00e-15	3.504
80×80	9.68e-16	9.85e-16	1.751
100×100	9.68e-16	9.78e-16	0.983
120×120	9.68e-16	9.74e-16	0.577
140×140	9.68e-16	9.72e-16	0.335

Finally, the orientation and height trajectories of the particle were used to calculate the potential energy landscape. The probability of finding a particle at each height depends on the potential energy at that location. Boltzmann's equation is given by:

$$p(h) = A \exp(-\frac{\phi(h)}{kT}) \tag{2.14}$$

where p(h)dh is the probability of finding the particle between h and h + dh, ϕ(h) is potential energy at that height. The shape of the histogram of particle observations n(h) is same as the shape of the probability density function p(h)[44,45]. In other words, n(h) is directly proportional to p(h) and the potential energy profile can be deduced by inverting **Equation 2.14** to give **Equation 2.15**.

$$\frac{\phi_c(h)-\phi_c(h_m)}{kT} = \ln\frac{n(h_m)}{n(h)} \tag{2.15}$$

Where $\phi_c(h_m)$ is the potential energy of the particle in the most probable height, $n(h_m)$ is the number of particle observation at the most probable height and $n(h)$ is the number of particle observation at that height. Comprehensive details of analyzing data associated with TIRM can be found elsewhere[44]. I included the effect of orientation in assembling the potential energy landscape by calculating a potential energy profile based on height observations (**Equation 2.15**) at each theta interval. In other words, the potential energy profile at each θ was computed assuming a Boltzmann distribution of height at each of those theta. The potential energy profiles at each theta were then assembled to obtain the potential energy landscape for a Janus particle.

In the simulation process, I developed an in-house made MATLAB code (APPENDIX 2.1). In the first part of the code, the particle is meshed into the small pieces. The selected mesh size, as it is explained previously, was 100 by 100 in polar and azimuthal angles. At each time step after the projection of the small curve surfaces, the code calls different functions to calculate double-layer electrostatic force (Eq. 2.11) based on the zeta potential of the specific meshed area. A critical feature of the code is that during rotation of the particle in theta (polar angle) direction, I assumed that the coordinate system is dynamic, and it rotates by rotation of the particle in the polar angle. The reason to apply this feature is that it helps to control the surface area value of each meshed area as the particle rotates. Also, given the axisymmetric nature of the problem, phi does not play a role in these simulations. The relevant forces are gravity, which is fixed, and the electrostatic force, which depends on the height and polar angle of orientation. In the code, after calculating the effective forces at each time step between the particle and the substrate, the new rotational position of each mesh is defined based on the polar orientation of the particle at that specific step to be applied in the next step. At the end of the particle height and rotation calculation, the code converts all theta

positions into the range of 0 and 2π and calculates the height and rotational histogram of the particle.

2.3 Results & Discussions

2.3.1 A Janus particle with equal zeta.

I validated our method by conducting Brownian Dynamic simulations of a meshed spherical Janus particle with zeta potential across each hemisphere assumed to be equal ($\zeta_A = \zeta_B = \zeta_S$ = -50 mV) and subsequently compared the potential energy profile to the known analytical profile of an isotropic sphere. **Figure 2.2** shows the comparison between the potential energy profile obtained by dynamics and the analytical profile. The simulated data shown in **Figure 2.2** is that which converged to >6 kT based on the criteria described in the previous section. These converged data demonstrate the validity of our meshing and stepping algorithms.

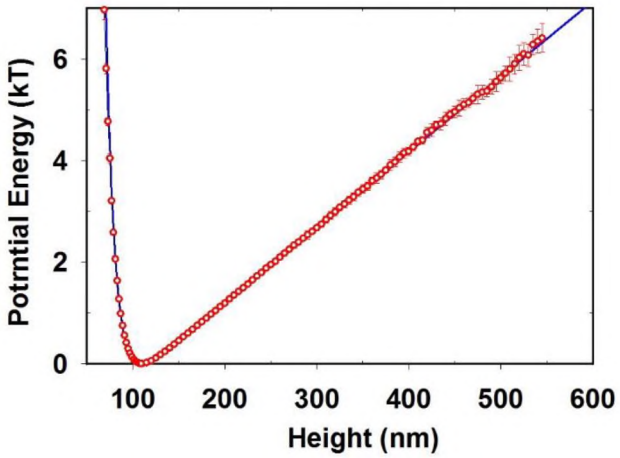

Figure 2.2. Potential energy profiles of a meshed spherical Janus particle with equal zeta potential across each hemisphere (red circles) and the known analytical potential profile from **Equation 2.1** of an isotropic sphere (blue line). All data reported from our simulations has converged to within a 0.3kT of the analytical values. The converged data reaches a maximum potential energy > 6kT, which is the threshold typically used for TIRM experiments. Note that only every fourth point of the simulated profile was reported in this Figure for clarity.

2.3.2 A Janus particle with unequal zeta

Once validated, I used our method to simulate the dynamics of a Janus particle of unequal zeta potential and subsequently calculate the potential energy landscape in both *h* and θ. A Janus particle of radius 3 μm, ζ_A= -5 mV, and ζ_B= -50 mV was simulated for 4.8 x 10^6-time steps. The raw simulated data consisted of the height and orientation of the particle at each time step. **Figure 2.1B** shows the convention I use to define hemisphere orientation with respect to the angle θ. In all of the simulations, the initial orientation of the particle was set to π/2. Potential energy landscapes were calculated from 10 simulations.

2.3.2.1 Janus particle rotational and height fluctuations

Figure 2.3 shows the rotational fluctuations experienced by the Janus particle for a representative simulation. The particle undergoes stochastic fluctuations because of rotational diffusion, rotating between ~0 and ~20 radians. The time scale for rotational diffusion of a micrometer scale particle scales with ~a^{-3} (rather than ~a^{-1} as with D_z) and is quite slow, thereby producing rotational fluctuations over only ~3 revolutions in the 6 hours of simulated time.

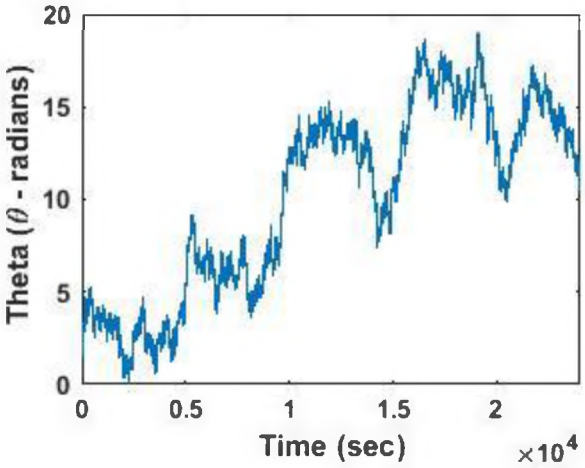

Figure. 2.3. Rotational fluctuations from a representative simulation of a Janus particle with two different zeta potentials (ζ_A= -5 mV, ζ_B= -50 mV) for 4.8 x 10^6 time steps.

Figure 2.4 shows the 3D histogram, as well as cut away panels of the 2D histograms, for height and orientation. The bin size in height was equal to $\Delta h = 1$ nm and the bin size in orientation was equal to $\Delta\theta = 2°$. The histogram of orientation comprising bins between 0° and 180° utilizes the rotational symmetry of the particle in two ways. First, all rotational fluctuations were converted to a confined range, between 0° and 360°, because of the 2π orientation repetition of the particle; for instance, $\theta = 90°$ is identical to $\theta = 450°$. Second, the particle has rotational symmetry such that it is only necessary to consider orientation positions sampled between $\theta = 0$ and $\theta = 180°$. There is a peak in height at each orientation, which is the maximum number of observations or the location of most probable height at that orientation. The location of the most probable height can also be seen in **Figure 2.4A**. Note that the observable peak in **Figure 2.4A** is not sharp (as compared to an isotropic particle), because the most probable height at each orientation, which differs, is being displayed in 2D.

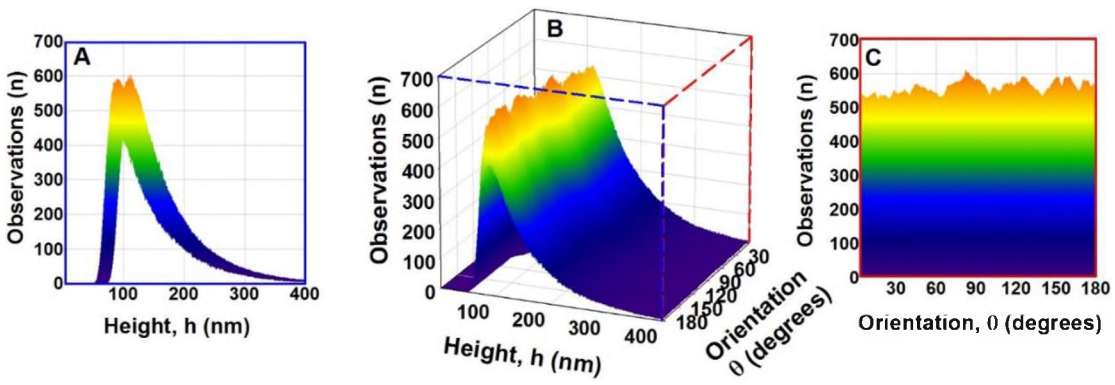

Figure. 2.4. Histogram of position and orientation observations. (A) 2D view of the histogram that shows just height and number of observations. (B) 3D histogram in both height and orientation. (C) 2D view of the histogram that shows just orientation and number of observations.

A distinct difference between **Figures. 2.4A** and **2.4C** is that there is a clear height preference, while no clear orientation preference. One may expect there to be an orientation preference because of the change in mobility associated with lower heights sampled at small zeta potentials. For instance, rotational diffusion is further hindered

when the particle rotates towards the lower zeta surface and samples lower heights. We tested this hypothesis by tabulating the orientation preferences for varying zeta conditions. Over a set of ten simulations, there was no clear preference between the hemispheres with a smaller zeta potential, as compared to the hemisphere with larger zeta potential. However, after averaging those ten simulations, there was a very small preference for the hemisphere with the smaller zeta potential to be orientated towards the substrate. **Table 2.2** summarizes the preference in zeta potential values. Given that there is no direct dependence of orientation fluctuations on the potential energy (via Eq. 2.9), one would not expect there to be a most probable orientation. However, the very weak dependence of rotational diffusion on height could be the origin of the minor preference shown in our results summarized in **Table 2.2**. Note that I expect the presence of a cap with a density not matching that of the base particle to profoundly impact these rotational sampling results.

Table 2.2: Number of particle observation in various positions.

ζ_A [mV]	ζ_B [mV]	No. of Obs. A Down	No. of Obs. B Down
2	20	**2,444,485**	2,355,515
5	50	**2,424,742**	2,375,258
10	60	**2,524,228**	2,275,772
5	100	**2,480,467**	2,319,533

2.3.2.2 Calculating and interpreting the potential energy landscape

Simulated observations of height were used to compute the potential energy profile of the particle at each individual orientation **Equation 2.15**. At each orientation, the maximum number of observations occurs in the most probable height, which appears as $n(h_m)$ in **Equation 2.14**. The bin size of the height was set $\Delta h = 1$ nm and the bin size in orientation was equal to either $\Delta\theta = 1°$ or $2°$. **Figures 2.5A & 2.5B** show the potential energy landscape calculated from simulated data. Note that these reported

data satisfy two conditions for convergence: (1) the standard deviation from 10 sets of potential energy landscapes should be less than 0.3 kT at each point and (2) the difference between the average of 10 sets of potential energy landscapes and the analytical potential energy landscape should be less than 0.3 kT at each point. The analytical potential energy landscape was calculated by fixing the orientation in a specific position, meshing the particle, then using **Equations 2.1 & 2.10 – 2.13**. This process was repeated for all desired heights to obtain the landscape. An analytical potential energy landscape for standard simulation conditions is shown in **Figures 2.5C & 2.5D**. This procedure provided minimum and maximum heights for which the simulation converged in each orientation.

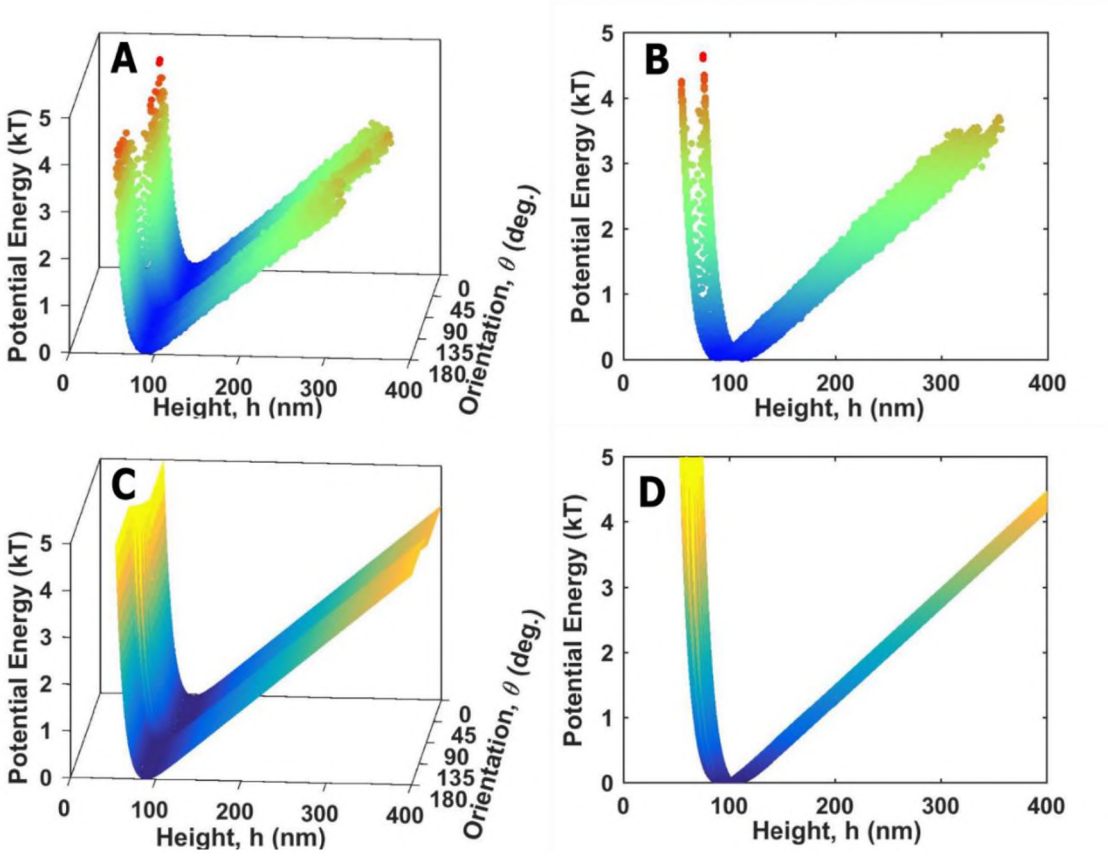

Figure 2.5. Potential energy landscape for a Janus particle with ζ_A= -5 mV and ζ_B= -50 mV. (A) 3D and (B) 2D view of potential energy landscape. The height and orientation bin sizes were 1 nm and 2°, respectively. The potential energy landscape displays the expected expo-linear profile, but with a transition at θ = 90° at the location of boundary between ζ_A and ζ_B. (C) 3D and (D) 2D view of analytical potential energy landscape for Janus particle with ζ_A= -5 mV and ζ_B= -50 mV.

Figure 2.6A shows that the potential energy profile at ($0° \leq \theta° < 2°$) is shifted to larger heights in comparison to orientation that ($178° \leq \theta° < 180°$) in **Figure 2.6C**. The reason for the shift to larger heights at $0° \leq \theta° < 2°$ is that at this orientation hemisphere B, with ζ_B= -50 mV, is wholly exposed to the surface with no contribution from hemisphere A. As a consequence of the relatively stronger electrostatic repulsive force, the particle samples larger heights with a larger most probable height. Conversely, the electrostatic repulsion force at $178° \leq \theta° < 180°$ is orientated such that hemisphere A, with ζ_A= -5 mV, is wholly exposed with no contribution from hemisphere B. This orientation experiences a relatively weaker electrostatic repuslive force and the particle samples smaller heights at this orientation.

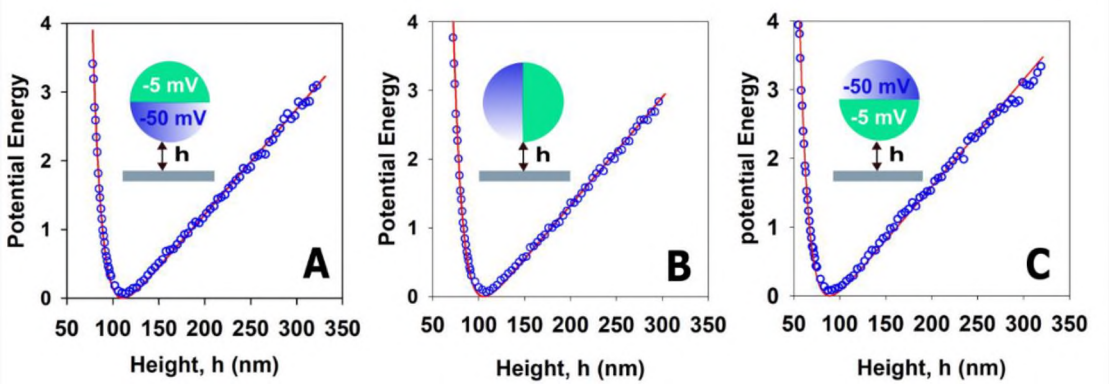

Figure 2.6. The potential energy deduced from simulation data of a 3 μm radius polystyrene Janus sphere with ζ_A= -5 mV and ζ_B= -50 mV in 1 mM NaCl electrolyte (blank blue circles). The simulation conditions are 4.8 x 10^6 iterations and Δt = 5 ms. The selected orientation bin size in this Figure is $\Delta\theta = 2°$; thus, there are 90 orientation positions. The solid red line is a fit to the data as described in the main text. Figure (A) is for θ bin $0° \leq \theta < 2°$, Figure (B) is for θ bin $90° \leq \theta < 92°$, and Figure (C) is for θ bin $178° \leq \theta < 180°$.

Figure 2.7 is a 2D height and orientation view of **Figure 2.5**. The smallest and largest height is a potential energy slice at 3kT . This Figure illustrates the limiting and transitional behavior of the Janus particle as it rotates from large zeta (-50 mV) to small zeta potential (-5 mV). The particle experiences limiting behavior as θ approaches 0° and 180°, with each of these limits having potential energy profiles closely matching

particles with a uniform zeta potential of either – 50 mV (for 0°) or -5 mV (for 180°). The transition region between 80° and 100° is identifiable by the boundary found at the smallest heights, which is where the potential energy is equal to 3kT. The boundary at 3kT transitions from approximtlty 95 nm to 80 nm, while the most probable height transitions from approximtly 110 nm to 90 nm (summarized in **Table 2.3**). This signiture results from the change in magnitude of the surface zeta potential as a consquenque of rotation, as illustrated in the bottom panel of **Figure 2.7**. A change in zeta potential magnitude will induce a change in the magnitude of the electric double layer force. The resolution of the transition will be an important asepct of data analysis for TIRM experiments. These simulations show that even for a perfectly discrete boundary, there is a diffuse transition between hemisphere A and hemisphere B. Further, simulations with 3 μm polystyrene particle (results not shown) demontrated that the shape of the transition was not a strong function of particle size. The potential energy landscape was also used to determine the appropriate time step for such a simulation. The time step was systemically changed for a Janus particle with -5 mV and -50 mV zeta potentials (rows 5 - 10 in **Table 2.3**). Our results showed that landscapes obtained from simulations with time steps of 5 ms, 6 ms, 7 ms and 8 ms have good agreement with analytical, while step times <5 ms and >9 ms are inaccurate.

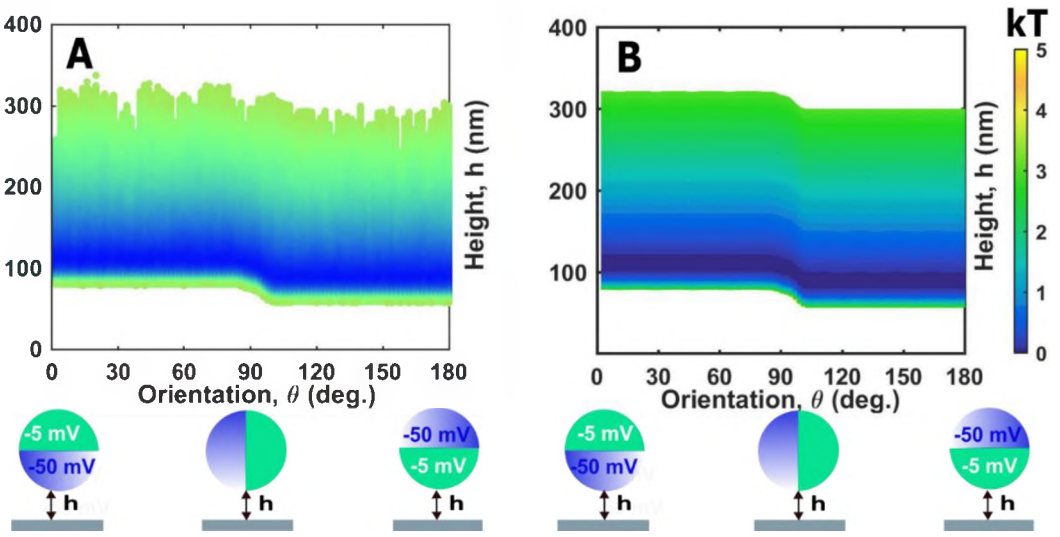

Figure 2.7. (A) 2D Orientation – Height view of potential energy landscape. As can be seen in the figure the position and shape of the Janus spherical particle in this simulation in the $0° \leq \theta < 2°$, $90° \leq \theta < 92°$, and $178° \leq \theta < 180°$ are shown. The potential is slice at 3 kT and the left and right-side boundaries are representing this slice. There is a distinct transition when rotation through past 90°. (B) The 2D view of analytical potential energy profile for standard simulation conditions and bin size equal to 2 degrees. The potential is slice at 5 kT and the left-side and right-side boundaries are representing this slice.

2.3.2.3 Determining particle and solution properties from potential energy landscape.

One outcome of a TIRM measurement is the determination of particle and solution properties from the position and orientation observations and ultimately the potential energy landscape. The simulation described herein is a tool for developing a methodology for determining particle properties from a TIRM measurement on an anisotropic particle. Herein, I fit the potential energy landscapes for a variety of conditions with a non-linear least square method to determine particle and solution properties, which are summarized in **Table 2.3**. The potential energy landscape was used to determine particle and solution properties, including particle radius a, hemisphere A zeta potential ζ_A, hemisphere B zeta potential ζ_B, the solution's Debye length κ^{-1}, and the most probable height h_m, as would be done in a TIRM experiment.

Table 2.3: Parameter fits for various conditions.

	Real Data				Fitting Parameters					
	ζ_A [mV]	ζ_B [mV]	Δt [ms]	Orientation Bin Size	Hm(A) [nm] Error%	Hm(B) [nm] Error%	k [nm] Error%	r [μm] Error%	ζ_A Error%	ζ_B Error%
1	2	20	5	2 degrees	79.89 0.12%	102.3 0.33%	0.1071 2.88%	3.038 1.2%	2.81 40%	23.38 17%
2	10	60	5	2 degrees	95.73 0.3%	112.07 0.35%	0.1049 0.7%	3.05 1.6%	11.6 16%	65.89 9%
3	5	100	5	2 degrees	89.16 0.4%	115.38 0.26%	0.1062 1.9%	3.035 1.1%	6.34 20%	141 41%
4	5	50	5	1 degree	88.61 0.21%	110.4 0.18%	0.1074 3.31%	3.071 2.3%	7.73 54.6%	80.23 60.4%
5	5	50	5	2 degrees	89.07 0.3%	110.81 0.54%	0.1045 0.4%	3.046 1.5%	5.86 17%	52.48 4.8%
6	5	50	2	2 degrees	88.18 0.6%	95.05 13.74%	0.1071 2.9%	2.96 1.2%	10.18 116%	85.87 71.7%
7	5	50	6	2 degrees	89.22 0.48%	110.78 0.53%	0.1042 0.12%	3.038 1.29%	5.64 12.8%	51.72 3.4%
8	5	50	7	2 degrees	89.3 0.57%	110.82 0.56%	0.1044 0.29%	3.035 1.17%	5.41 8.3%	52.28 4.5%
9	5	50	8	2 degrees	89.52 0.8%	110.94 0.67%	0.1027 1.3%	3.045 1.5%	4.87 2.5%	45.67 8.6%
10	5	50	10	2 degrees	89.59 0.9%	111.9 0.8%	0.102 2.06%	3.039 1.33%	4.7 5.8%	41.56 16.8%

The potential energy profile at every orientation (including in the transition region) was fit to determine particle radius and Debye length, while the potential energy profiles only at the limiting conditions were used to calculate the most probable height and zeta potentials. Determining particle and solution properties from a fit of the potential energy landscape requires treating different regions of the landscape because of variations in sensitivity of parameters to the fit. Particle radius and the solution's Debye length are robust to the fitting process because small changes in each of those parameters will produce significant changes in the potential energy profile. However, the particle's zeta potential appears only in the electrostatic parameter B, which itself is a pre-factor to the exponential electrostatic repulsion. Although large changes in zeta potential at our conditions will induce large changes in B, these large changes in B do not produce significant changes in the potential energy profile. This issue was exacerbated at the transition region, where there are contributions from both

hemispheres to the electrostatic repulsion. Consequently, the electrostatic part of the interaction is known to be difficult to determine, even for isotropic particles.[44] Thus, once the transition region was identified, I fit the potential energy profile only at the limiting conditions as $\theta \rightarrow 0°$ or $\theta \rightarrow 180°$. For example, among 90 orientation conditions (with $\Delta\theta = 2°$) the average of first 40 orientations was used to calculate minimum height and zeta potential of the B hemisphere and average of last 40 orientations was used to calculate hemisphere A parameters.

Based on our results summarized in **Table 2.3**, I determined that it would be possible to measure properties of the Janus particle as shown by the good agreement between fitting parameters and real system parameter values (Rows 1-3 & 5 in **Table 2.3**). **Figure 2.6** shows a sample of fitting results for all three orientations. **Figure 2.6A** shows the orientation $0° \leq \theta < 2°$ corresponding to hemisphere B (ζ_B= -50 mV) of the Janus particle on the bottom side and **Figure 2.6C** shows orientation $178° \leq \theta < 180°$ corresponding to hemisphere A (ζ_A= -5 mV) of the Janus particle is on the bottom side.

The accuracy of the parameter fits was impacted by the choice of bin size in orientation. Rows 4 and 5 of Table 5 show that the zeta potential fits are more accurate when choosing $\Delta\theta = 2°$ as compared to $\Delta\theta = 1°$. The origin of this difference is in the number of observations in each bin that is necessary for an accurate fit. Reducing the orientation bin size from $\Delta\theta = 2°$ to $\Delta\theta = 1°$ reduces the number of observation binned into each orientation. The reduction in observations at each orientation reduces the accuracy of the potential energy profile calculated for that orientation. Although operating with larger orientation bin sizes will assist in determining parameters, larger orientation bins reduces the resolution of the transition region, which may be necessary for determining the patterning on the surface and will become especially important for particles with more elaborate patterning or diffuse boundaries. Ultimately, these results

illustrate that there is a balance between fit parameters and potential energy landscape resolution when attempting to resolve non-uniformities along the particle surface, which is one significant difference between a TIRM experiment with an isotropic particle versus one with an anisotropic particle. Further, far more observations will be required given the need to resolve potential energy in *both* h and θ for an anisotropic particle, as compared with just h for an isotropic particle. A typical TIRM experiment on an isotropic particle requires ~10^5 observations, but our simulation results suggest that ~10^6 - 10^7 observations will be required to calculate a potential energy profile comprising data of similar accuracy.

2.4 Conclusions

This article describes the method and results from a Brownian Dynamics simulation suitable for a Janus sphere of unequal zeta potential. Our effort was motivated by the need for guidance and methodology for analyzing data from a TIRM experiment. For this purpose, I have developed a method for meshing a sphere of arbitrarily patterned zeta potential that integrates with a Brownian dynamics simulation tool. Following validation of the meshing method, I simulated the position and rotational trajectories of the particle near a boundary and subsequently calculated potential energy landscapes for the Janus particles. I derived for the first time a 3D potential energy profile landscape for a Janus particle as would be obtained in a TIRM system. This simulation and landscape can predict the behavior of the Janus particle and help us in the optimization of experimental parameters in an experimental TIRM system for a Janus particle. Results show that the potential energy landscape of Janus sphere has a transition region at the location of the boundary between the two Janus halves, which depends on the relative zeta potential magnitude. The potential energy

was accurately fit to obtain parameters including zeta potential magnitude in each hemisphere, particle size, minimum potential energy position and electrolyte concentration or Debye length. Time step and orientation bin size are important parameters in the simulation and data analysis process. Additionally, simulations show that an experiment may require more than 10^6 observations to obtain a suitable potential energy landscape. These results demonstrated the utility of Brownian dynamics simulations as a tool to probe TIRM for anisotropic particles.

CHAPTER III

LOCAL MEASURMENT OF JANUS PARTICLE CAP THICKNESS

3.1 Introduction

Nanometer to micrometer scale particles with chemical or geometric anisotropy have the potential to transform applications in chemical and physical sensing, medical drug delivery, as analogs for molecular scale phenomena, and in consumer products[78–86]. One such anisotropic particle is a patchy or "Janus" particle, typically consisting of a native colloidal sphere with a cap of a second material covering approximately half of the available surface area. Other particles, including rods[87] and sheets[88], can also be made Janus with a variety of synthetic routes. Janus particles have been identified as good candidates for sensing in complex rheological or mechanical environments because the optical signature inherent in a Janus particle, which facilities tracking the rotational or translational diffusion of the particle[86]. Janus particles with engineered ligand surface chemistries may offer a strategy for directed cell entry that particles of uniform chemistry or shape do not. Further, foams and emulsions stabilized by Janus particles that act as solid surfactants are extremely stable [89–91]. Multiphase fluids, regularly found in consumer products and food, would benefit from such a technology by engineering long shelf life and other added value functionalities to products [92].

One route for fabricating Janus particles is to conduct vapor deposition of a cap material onto a monolayer of native particles[93]. Vapor deposition and subsequent

chemical modification was initially used to fabricate Janus particles, with approximately 50% area coverage, but was developed further into a robust technique called Glancing Angle Deposition (GLAD) capable of fabricating particles with patches of various areas and geometry[94,95]. GLAD is now regularly used to produce patchy colloids of varying native particle and patch composition, surface area, and geometry[96]. The nominal patch thickness is typically controlled by the instrument used for the deposition process, while the patch size and shape are controlled by adjusting the substrate inclination angle and the angle with respect to the crystallinity axis. Scanning electron microscopy is effective for measuring the patch surface area and geometry, but there is currently no practical method for measuring patch thickness. The patch thickness is typically assumed to be equal to the nominal thickness along the entire patch contour. Yet, the real patch thickness, as well as the variation of the thickness along the contour of the cap is important for predicting and interpreting the dynamics of patchy colloids at equilibrium, in response to external fields, or swimming in response to local physiochemical gradients.

3.2 Experiment and Methodology

Herein we report the first local measure of patch thickness for Janus particles comprising native polystyrene spheres with a gold patch of approximately 50% area coverage (*i.e.* a Janus cap). In summary, Janus particles were fabricated by deposition of a thin layer of gold in a physical vapor deposition system via thermal evaporation technique on one hemisphere of native polystyrene beads (**Figures 3.1A – 3.1B**). Following the gold coating process, a particle of interest was locally coated with carbon (**Figure 3.1C**). Local measurement was achieved by cutting away a portion of the Janus particle with a focused ion beam (FIB) to reveal the Janus particle cross-section (**Figure**

3.1D). The cut furnished an SEM micrograph from which the direct measure of gold thickness along the surface was possible. Although the techniques employed in our work (i.e. SEM, FIB) are not new, the application of these techniques, implementation, and analysis of this specific Janus particle system are new and important to the prediction and measurement of Janus particle dyanmics[38]. Our measurements show that caps are not of constant thickness, but rather varied in thickness along the contour of the gold cap. We also found that varying deposition rates between 0.5 Å/s and 2 Å/s did not significantly impact the variation in thickness across the cap.

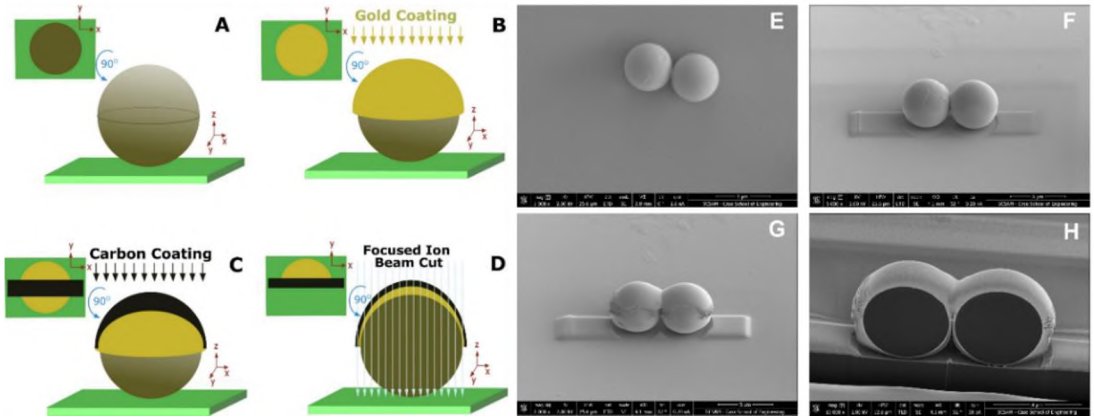

Figure 3.1. Preparation of a cross-section of a Janus sphere. The process consisted of (A) depositing a native particle, (B) gold deposition in the direction normal to the substrate, (C) local carbon coating in a strip along the particle and normal to the substrate, and (D) a focused ion beam (FIB) cut normal to the substrate to reveal the particle's cross-section. The process was imaged to show doublets (E) following gold deposition (top view), (F) following local carbon deposition (angled view), (G) following the first FIB cut (angled view), and (H) following the final FIB cut, revealing the cross section of the doublets (angled view).

Molecular Probes™ polystyrene sulfate latex beads 5 µm in diameter were obtained from Fisher Scientific (Lot #1964358). The polystyrene beads were drop cast onto 5 mm x 5 mm silicon wafers obtained from SPI supplies (Lot #1200724). Silicon chips with the deposited monolayer of polystyrene particles were transferred onto a precut microscope slide with high temperature adhesive tape. The samples were then transferred into the glovebox that was purged with N_2, pumped down to 4 x 10^{-6} Torr, and then purged again for three cycles. Once inside the glovebox, the microscope slides holding the samples were secured to a metallic plate using the provided screws and the plate was then rotated to orient samples facing downwards. Finally, gold was deposited by thermal evaporation in a physical vapor deposition system (Angstrom EvoVac) at the prescribed rate, thickness, and power (**Figure 3.1E**). The nominal thickness of the deposited material was tracked by a quartz crystal microbalance.

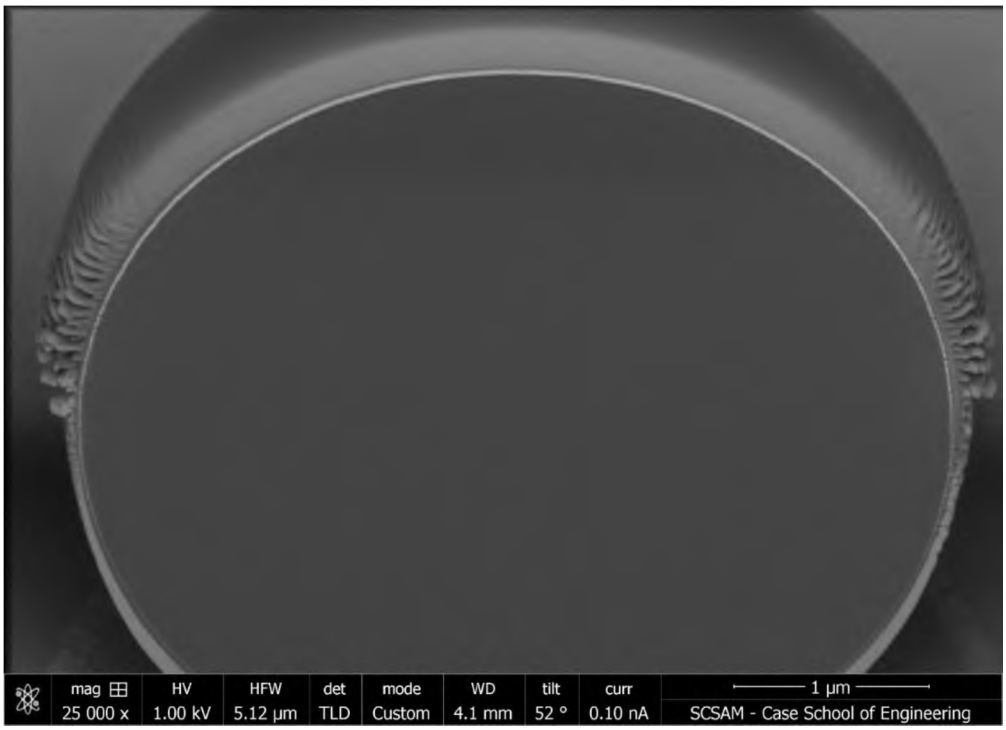

Figure 3.2. SEM micrograph of 5 mm polystyrene bead with 20 nm cap deposited at 1 Å/s.

Following addition of the gold layer, the samples were transferred to a FEI Helios 650 Field Emission Scanning Electron Microscope with Focused Ion Beam. Carbon was locally deposited with the electron beam using an *in-situ* gas injecting system (GIS) to protect the surface before ion beam cutting. Carbon was used rather than the default Pt to enhance the contrast of the gold in the image, as seen by the thin rectangular layer surrounding the particle (**Figure 3.1F**). The additional carbon layer also helped to protect the thin gold layer from delamination during the subsequent FIB cut. A 16 kV 0.43 *nA* ion-beam current was used with the FIB to mill away layers to reveal the cross-section of the particle (**Figures 3.1G & 3.1H**). Finally, the particle was imaged at an angle of $\theta = 52^{o}$ (angle in which the particles are normal to the ion beam) to visualize the gold layer thickness. The tilt angle of the sample impacted the interpretation of the imaged thickness. The extent of impact depended on the angular ϕ position of the measurement because only distances in the y-axis required correction (**Figures 3.2 & 3.3**). SEM images revealed the gold coating as a thin line of bright pixels on the top perimeter of the particle. Images were processed to determine the local thickness of the bright line. An in-house made code was developed to analyze of the images and calculate thickness of the coating (**APPENDIX 3.1**). In the image processing for the image, the mean intensity of 1842 pixels at three locations ($\phi = 135°, 90°, 35°$) around contour of gold was equal to $I_m = 162.29$ and standard deviation equal to $s = 12.09$. The threshold used to make the image binary was $I_m - s = 150$. The threshold was rounded to obtain an integer. In **Figure 3.**4, the thick white line is the gold cap, while the diffuse pixels above are stray pixels. As it can be seen in **Figure 3.4** image processing was conducted to exclude the stray pixels by both avoiding the area of the image in which they appear and also only counting a pixel when it has two bright neighbors. Later, each image was processed with 1000 intensity profiles between ($\phi = 180° - 0°$) (**Figure 3.5**).

The tilt angle of the sample impacted the interpretation of the imaged thickness. The extent of impact depended on the angular ϕ position of the measurement because only distances in the y-axis required correction. The real gold thickness was related to the measured value by the following expression:

$$L_{cs} = m \underbrace{\sqrt{\cos\phi^2 + \frac{\sin\phi^2}{\sin\theta^2}}}_{C} \tag{3.1}$$

The value of θ was fixed for all experiments θ = 52°, whereas f varied between ϕ = 0° and ϕ = 180°. The value of the correction factor C varied between C = 1 at ϕ = 0°/180° and C = 1.269 at ϕ = 90°.

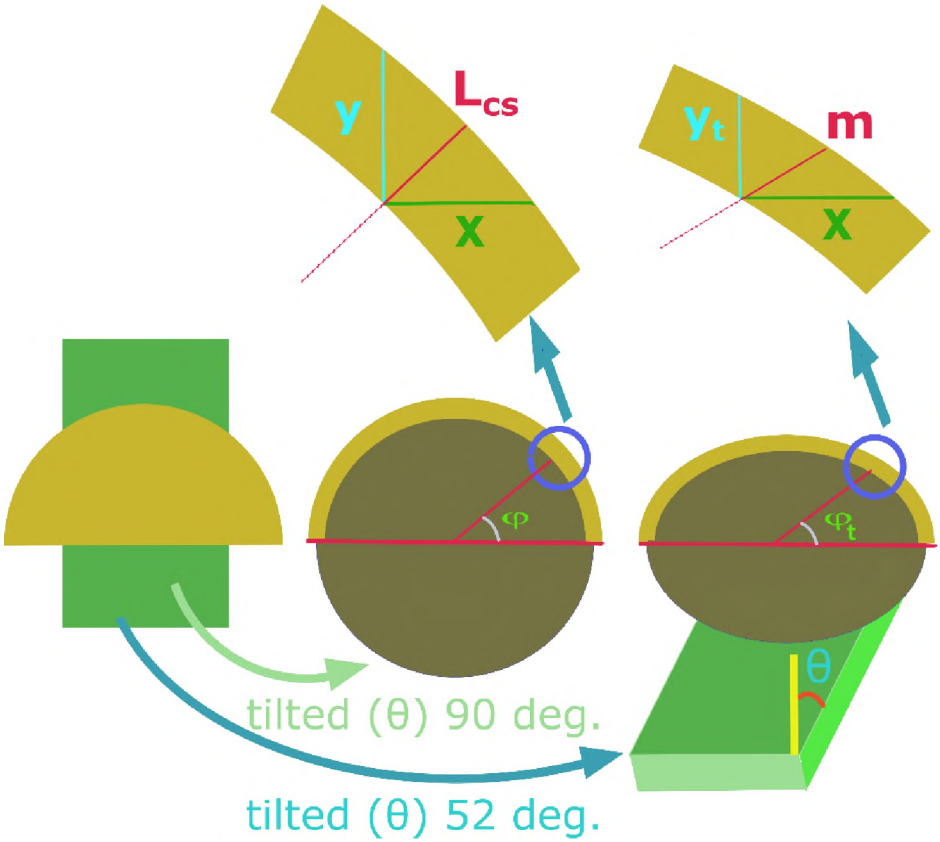

Figure 3.3. Illustration showing particle inclinations inside the FEI Helios 650 Field Emission Scanning Electron Microscope after carbon coating and cutting of the particle. The left side image shows the particle while the stage is at its initial condition and objective is perpendicular to the top of the particle (θ = **0°**). The middle image displays the particle at stage incline of θ = 90°, which is perpendicular to the cross sectional cut of the particle. The right image presents the working condition θ = 52°.

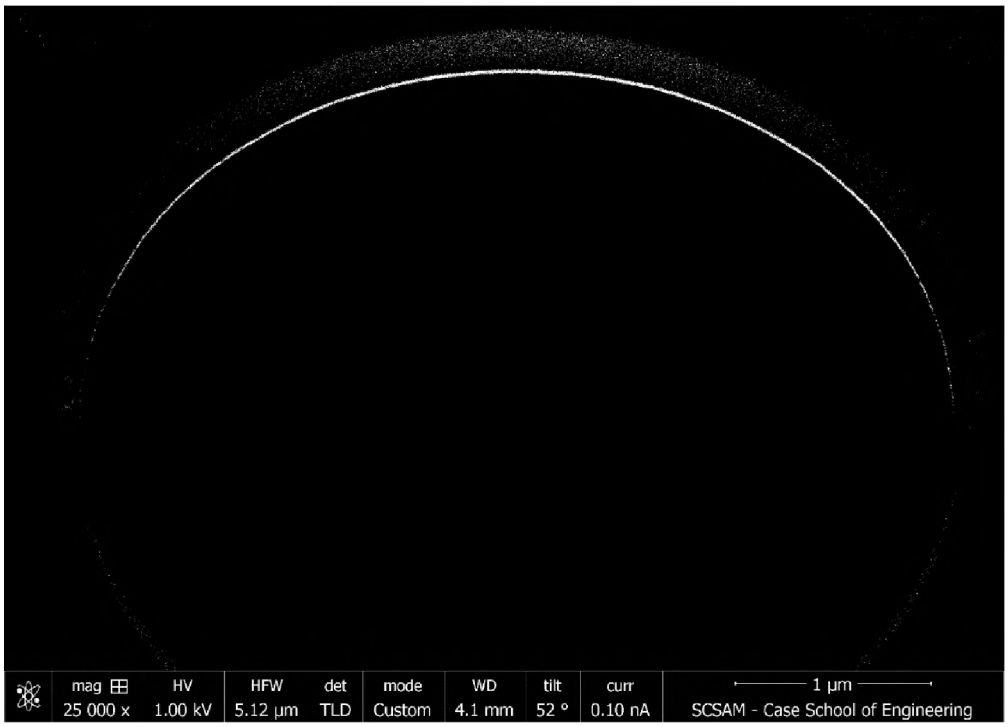

Figure 3.4. Binary SEM micrograph of 5 µm polystyrene bead with 20 nm cap deposited at 1 Å/s following threshold of 150. The thick white line is the gold cap.

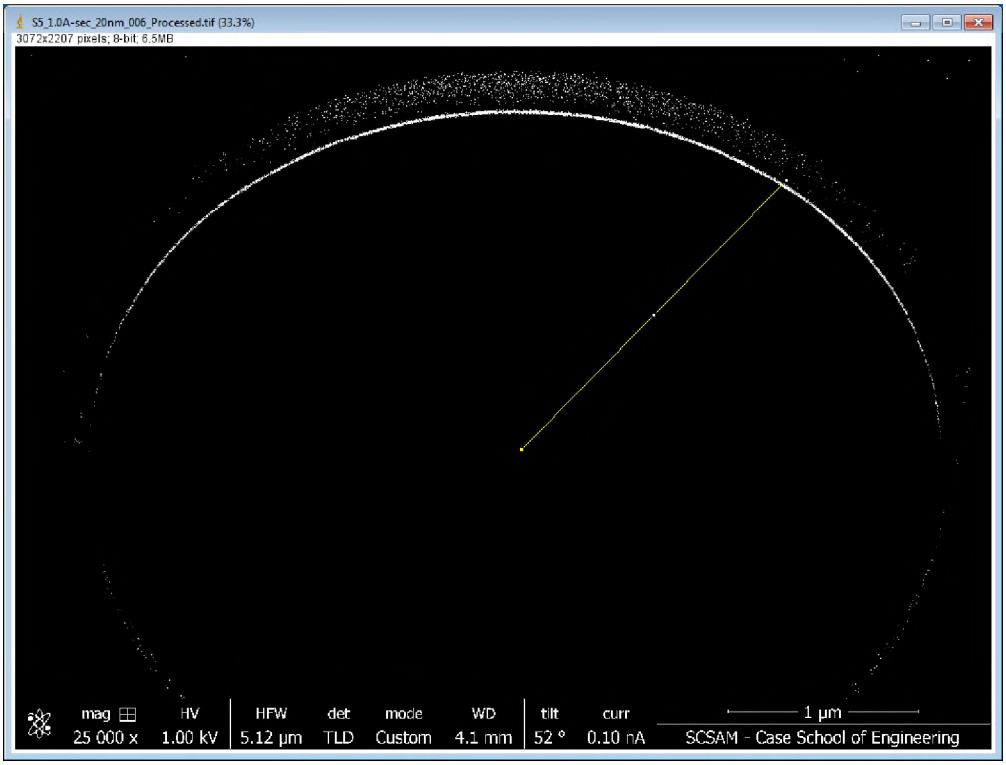

Figure 3.5. Example line along which intensity was measured.

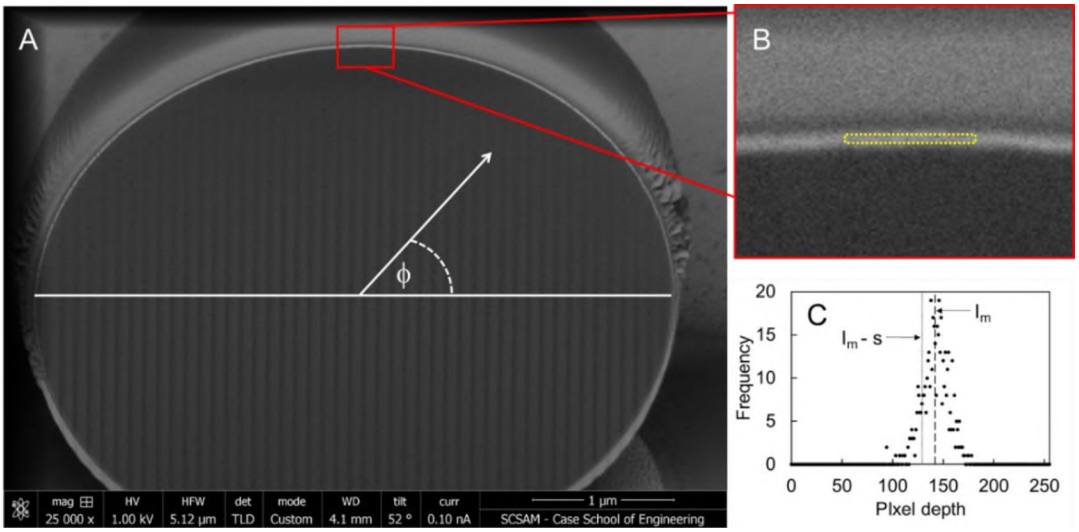

Figure 3.6. Determining threshold value for image processing. The threshold value was set equal to the difference between the mean and standard deviation of a selection of pixels along the gold contour of the particle. The pixels used to calculate these values were selected from contour positions $\phi = 135^{o}$, 90^{o}, and 45^{o}. (A) Original SEM micrograph, (B) zoomed in image and location of pixels used for calculation at $\theta = 90°$, (C) histogram of intensities from selection with pixel depth mean (I_m) and standard deviation (s) at $\theta = 90°$. The threshold used for image analysis was determined from the mean and standard deviations of data obtained at $\phi = 135^{0}$, 90^{0}, and 45^{0}. Images were threshold by making all pixels with > I_m-s equal to a pixel depth of 255.

3.3 Results

Initially, the mean and standard deviation of pixel depth along the gold cap was determined at three locations (ϕ = 135°, 90°, 45°) to obtain a threshold value I_t that would eliminate any non-gold pixels (**Figure 3.6**). The threshold value was set equal to the difference of the mean I_m and standard deviation s of the pixel depth found along the gold cap ($I_t = I_m - s$). Once the threshold value was determined, the 8-bit SEM image was made binary, leaving behind an image with a black background (pixel depth = 0), cap (pixel depth = 255), and stray pixels (pixel depth = 255). Stray pixels were a consequence of portions of the top of the particle having brightness greater than that of the gold perimeter (**Figure 3.4**). Once a binary image was obtained, the thickness of the

cap was measured with a custom macro written for Fiji (https://fiji.sc/). An ellipse was fit to the curve representing the cap because the spherical particle appeared as an ellipse as the sample was imaged at an angle (**Figure 3.3**). The pixel depth was then measured along a line from the center of the ellipse to a point closely (40 – 50 pixels from center of contour) outside that of the cap. Intensity profile curves were then analyzed to pinpoint the location of the boundary between the core polystyrene particle and the gold metal cap by identifying the portion of the curve that possess a pixel depth of zero for each particular angle ϕ and repeating the measurement along 1000 profiles from $\phi = 0°$ to $\phi = 180°$. Included in this measurement was a requirement that a pixel was counted as gold if and only if three pixels in a row had a depth greater than or equal to 2 x 255 = 510. Thus, single dark pixels with two bright neighbors count, while a dark pixel with one bright neighbor and one dark neighbor would not count as gold. This requirement included dropped pixels in the cap interior, but excluded stray pixels outside the cap. Finally, the actual length was determined by converting the pixel number counted as gold (integer number of pixels) to real thickness (nm), while accounting for the image tilt. The pixel resolution varied slightly depending on the imaging conditions, from 1.04 nm/pixel to 1.67 nm/pixel. The specific processing procedure used herein identified the cap to the level of a pixel, meaning the limiting resolution of our result is approximately ~ 1 nm. Note that increased resolution of this technique may be achievable by utilizing additional image processing steps that are often used in particle tracking to achieve sub-pixel accuracy[97].

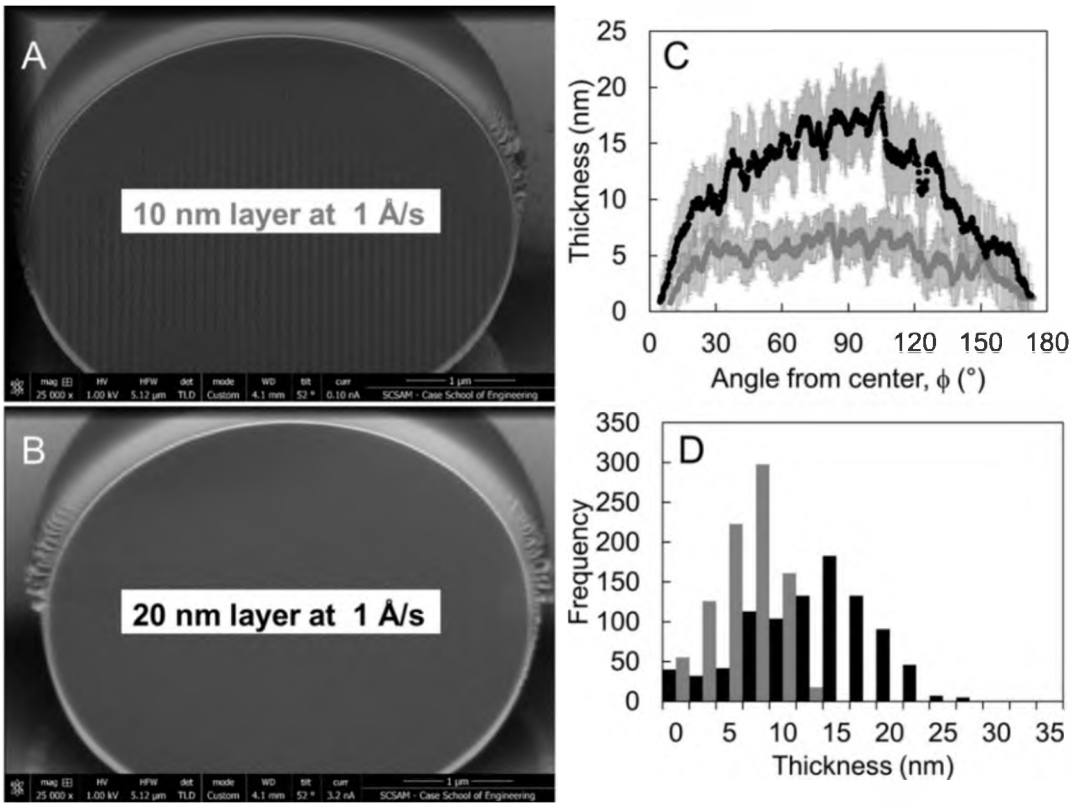

Figure 3.7. Thickness measurement for two thicknesses at fixed rate. 5 μm polystyrene spheres with a gold cap of nominal thickness (A) 10 nm and (B) 20 nm deposited at 1 Å/s. (C) & (D) The gold thickness varied continuously over the contour for both the 10 nm and 20 nm caps. Solid black and solid grey points and bars are for 20 nm and 10 nm layers, respectively.

The image processing and measurement were conducted for Janus particles prepared with nominal thicknesses of 10 nm or 20 nm at fixed deposition rates of 0.5 Å/s, 1 Å/s, and 2 Å/s. **Figure 3.7** shows the SEM micrographs, measured thicknesses along the contour, and histogram of thicknesses for 20 nm caps deposited at 1 Å/s. The measured thicknesses were reported as moving averages for every 20 measurements (**Figure 3.7C**), while the histogram was assembled for every thickness measurement (1000 total between $\phi = 0° - 180°$). The cap thickness varied continuously along the contour of the particle, between ~0 nm at the equator ($\phi = 0°$ and 180°), to a maximum near the pole ($\phi = 90°$). The maximum and mean thickness of all measurements, prior to taking moving average as shown in **Figure 3.3**, with standard deviation were 29.57 nm and 11.84 nm ± 5.77 nm for the 20 nm cap and 11.87 nm and 5.00 nm ± 2.68 nm

for the 10 nm cap. Surfaces normal to the deposition source had a thickness nearly matching the prescribed nominal thickness, while surfaces deviating from normal would had a thickness less than that of the nominal thickness, approaching ~0 nm when the surface was perpendicular. Cap thickness varying across the gold contour was an anticipated result, with this variation being previously suggested as an explanation for observed deviations in experimental systems from the predicted behavior for a perfect Janus cap[98].

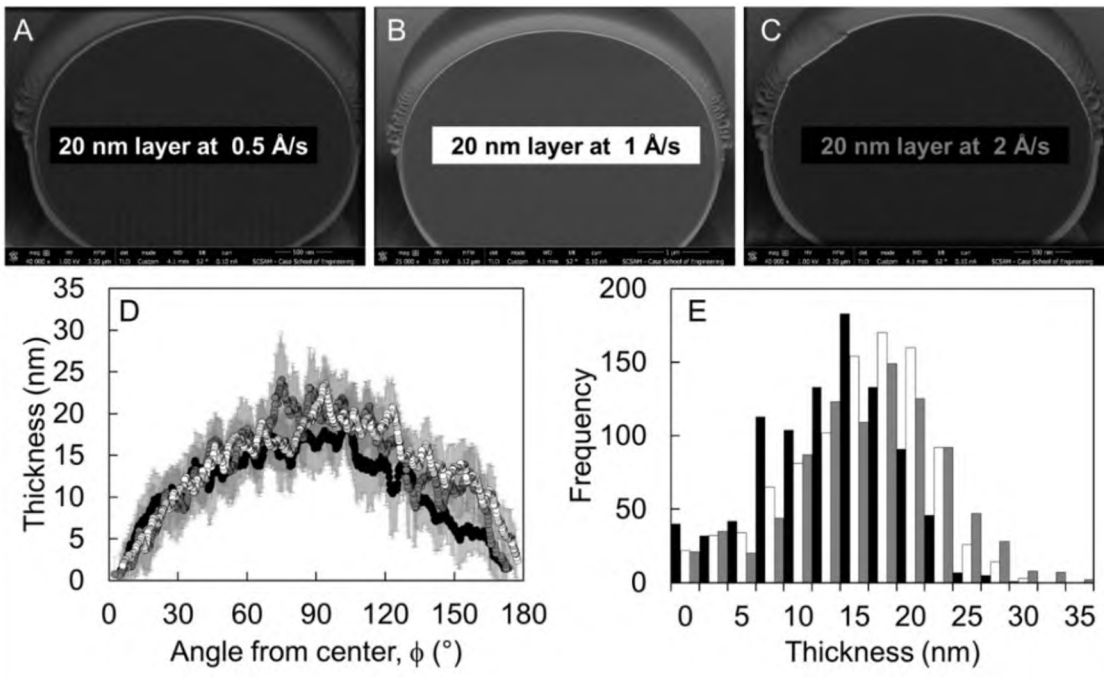

Figure 3.8. Thickness measurement for nominal 20 nm thickness at three different rates. 5 μm polystyrene spheres with a gold cap of thickness 20 nm deposited at (A) 0.5 Å/s, (B) 1.0 Å/s, and (C) 2.0 Å/s. The gold thickness varied continuously over the contour for each sample, but did not show any impact of deposition rate in this range. White points with black outline, solid black, and grey points with black outline are for 0.5 Å/s, 1.0 Å/s, and 2.0 Å/s, respectively.

A second set of experiments was conducted to test the impact of deposition rate on the variation in thickness across a Janus cap. Particles were prepared with nominally 20 nm thick caps at rates of 0.5 Å/s, 1 Å /s, and 2 Å /s. **Figure 3.8** shows SEM images of cross sections of these particles at these conditions, thickness profiles, and histograms of thickness measurements for the three conditions. Similar to data

summarized in **Figure 3.3**, **Figure 3.4** shows strong variation in cap thickness along the contour of the particle. However, there were no perceptible differences between caps deposited at the rates chosen, either in the coarse variation of cap thickness or in the local roughness. The histograms show very similar distributions, with mean thicknesses and standard deviations of 14.02 nm ± 6.01 nm, 11.84 nm ± 5.77 nm, 14.66 nm ± 6.66 nm for 0.5 Å/s, 1 Å /s, and 2 Å /s, respectively.

3.4 Conclusion

In summary, I presented an experimental and image processing procedure to measure the local cap thickness of Janus particles consisting of a 5 μm native polystyrene particle with a gold cap. Our data shows cap thickness strongly varies over the contour of the cap and that deposition speeds between 0.5 Å/s to 2 Å/s do not significantly alter this thickness variation or roughness of deposited material. These data can be used to accurately model the thickness of the cap for experiments or simulations that are concerned with the dynamics of a Janus particle at equilibrium or in response to external fields. Most work concerned with Janus particles has assumed a uniform coating thickness. However, non-uniform coverage (as detailed herein) will certainly impact the rotational and translational dynamics of a Janus particle in different environments. Note that this work was done only on one slice to demonstrate a proof of concept for imaging the Janus layer. It would be possible to image and assemble of a full 3D model of the cap by using the "slice and view" method [99–101]. Slice and view is an automated protocol for conducting serial sectioning of the sample, where each feature of interest is traced to create a 3D model of the cap.

CHAPTER IV

INFLUENCE OF CAP WEIGHT ON THE MOTION OF A JANUS PARTICLE VERY NEAR A WAL

4.1 Introduction

Colloidal particles dispersed in a liquid interact via surface forces that play a critical role in dictating the properties and performance of complex fluids. Over the past decade, the dynamics and interactions of anisotropic colloidal particles have gained attention[102] because of potential applications in various fields such as optical displays[103], magnetorheological system[104], controlling interfacial microstructure[3], self-assembly[4,105], microfluidic devices[6], tuning interparticle interactions[106,107], and biomaterials or drug delivery[108]. Supporting these efforts have been a variety of new techniques for the synthesis of anisotropic colloidal particles[4,54,114–116,57,58,108–113]. Newly developed fabrication techniques provided the ability to tune the shape and the surface properties of these materials. Janus particles are one class of anisotropic colloid, typically with some property difference between the two hemispheres. Each hemispherical domain of a Janus particle may have its own surface chemistry, shape, or other property[117].

Predicting the dynamics of anisotropic colloids is important for applications in real systems, for example during processing when complex fluids are often not at

equilibrium[118,119]. Various parameters influence the dynamics of anisotropic colloids[120–123]. Particle confinement will impact the hydrodynamic interactions between the colloid and boundary, thereby influencing particle mobility. Brownian motion and conservative (*i.e. path independent*) forces, such as electrostatic double layer repulsion and gravity, will also impact the dynamics of a confined spherical Janus particle. Although not dependent on orientation for an isotropic particle, each of these phenomena will likely depend on the orientation of an anisotropic particle. For example, a Janus particle with anisotropy in zeta potential will experience an electrostatic interaction that depends upon orientation with respect to the boundary[38]. Rotation of the Janus particle at a constant separation distance from a boundary induces an effective change in an interaction, which then alters the probability density at that particle's position.

Janus particles are fabricated by coating one hemisphere of a spherical colloidal particle with another material, usually a metal such as gold[96,124]. The cap typically has some nominal thickness from a few to tens of nanometers, but direct measurement of the coating thickness has shown the cap to be non-uniform across the contour of the particle[39]. Tracking translational and rotational displacement of Janus particles at various boundary, physiochemical, and rheological conditions will assist in understanding the dynamics of these particles[61,125–127]. Various studies have focused on the rotation of isotropic[11,12] and anisotropic colloids[128,129]. There has been some work on the translational and rotational dynamics of Janus particles near a boundary[98,130], on the effect of mass-anisotropic coating on the dynamics of active particles away from a boundary[131–133], and on the dynamics of Janus microswimmers which have bottom heaviness nearby surfaces[134]. Experimental techniques such as confocal microscopy[36,135], evanescent wave scattering[136], video-microscopy[137], and holographic

microscopy[62,138,139] were used to measure the rotational diffusion coefficient. Surface roughness[140], particle shape[141], external fields[142], and the presence of motility (*i.e. for active particles*)[74,143–148] were found to influence the rotation of Janus particles. Despite the significant recent work in this area, there has not yet been a detailed quantitative analysis of the dynamics of a Janus particle with a cap of non-matching density near a boundary.

Herein, we conducted Brownian dynamics simulations to predict the behavior of a Janus particle with a cap of density not matching that of the native particle. This technique has been previously used to study the dynamic behavior of other colloidal systems[64,149–151]. Our results show the importance of the particle's surface properties, in particular, the weight of the cap, on the dynamics of a particle close to a wall. We systematically altered coating thickness and particle size to test their impact on rotational and translational dynamics, probability distribution, and potential energy landscape. Our findings illustrate the importance of non-negligible gravitational torque on the rotational and translational trajectories of a Janus particle. Notably, the aforementioned torque influenced the behavior of Janus particles at conditions relevant to experimental studies.

4.2 Theory

4.2.1 Near-boundary forces and torques on a Janus particle

A colloidal particle dispersed in a fluid near a boundary experiences conservative, dissipative, and stochastic forces. Conservative forces experienced by a non-density matched particle in low concentration electrolyte with bound surface charges are primarily due to electrostatic double layer repulsion and gravity. Strong electrostatic forces help to keep the particle levitated close to the substrate. Van der Waals attraction

may also play a role at sufficiently small separation distances (h < 100 nm), but is neglected herein[44,152].

A charged spherical colloidal particle with radius a and separation distance h (see **Figure 4.1a**) will experience an electrostatic force that depends upon the size of the particle, the solution Debye length κ^{-1}, and Stern potential of the particle and the substrate. The conservative force F_c is calculated by:

$$F_c = -\frac{d\phi_c(h)}{dh} = \underbrace{\kappa B \exp(-\kappa h)}_{\text{Electrostatic}} - \underbrace{\frac{4}{3}\pi a^3(\rho_p - \rho_f)g}_{\text{Gravitational}} \tag{4.1}$$

$$B = 64\pi\varepsilon_0\varepsilon_f a\left(\frac{kT}{e}\right)^2 \tanh\left(\frac{e\zeta_s}{4kT}\right) \tanh\left(\frac{e\zeta_p}{4kT}\right) \tag{4.2}$$

$$\kappa = \sqrt{\frac{2e^2 C_\infty}{\varepsilon_0\varepsilon_f kT}} \tag{4.3}$$

where B is the electrostatic charge parameter, ρ_p and ρ_f are density of the particle and fluid respectively, g is gravitational acceleration, ε_0 is the electric permittivity of vacuum, ε_f is the relative permittivity of water, e is the charge of an electron, ζ_s and ζ_p are the zeta potentials of the surface (boundary) and particle respectively (equated with the Stern potential), k is the Boltzmann's constant, T is temperature, and C_∞ is electrolyte concentration in the bulk. This expression is applicable to an isotropic particle with uniform surface chemistry. A meshing method was previously developed to account for these forces on a chemically anisotropic particle with a non-uniform zeta potential[38].

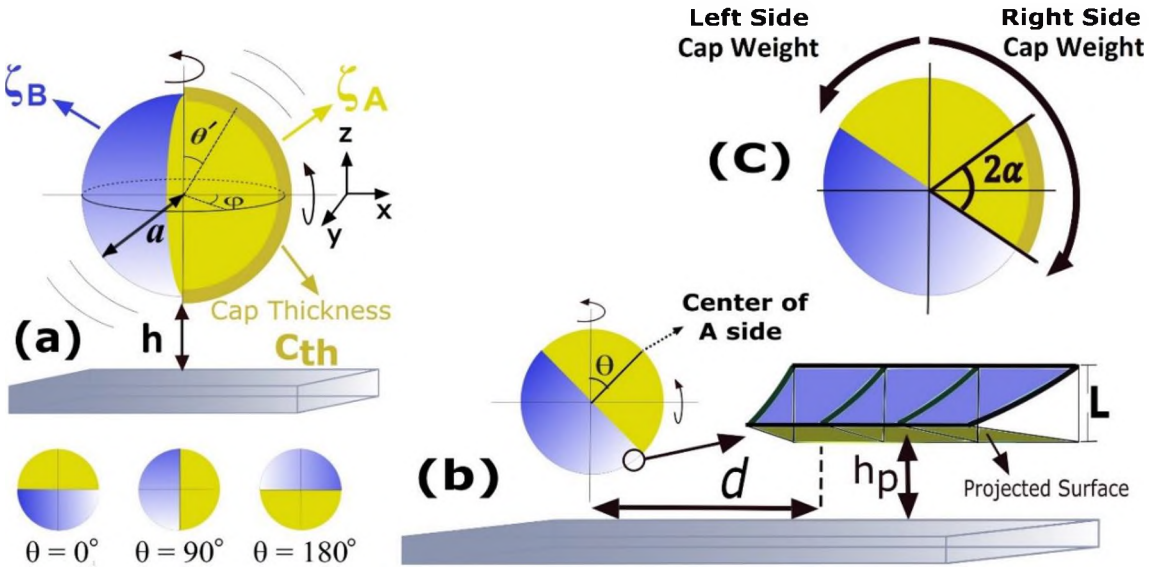

Figure 4.1. (a) Schematic of a Janus particle with one hemisphere coated by a metallic cap. (b) Schematic representation of θ orientation. (c) Alpha (α) definition for the center of mass calculation.

A Janus particle will experience stochastic torque, just as an isotropic particle, but will additionally experience deterministic torque due to the asymmetry in both the gravitational and electrostatic interaction. For instance, a mismatch in the electrostatic charge on the surface of a particle induces an electrostatic torque relevant only when the boundary between the hemispheres of the Janus particle is near perpendicular to the wall. Similar to accounting for variations in surface chemistry in calculating translational displacements as mentioned above, a meshing method was used to calculate the electrostatic torque on a Janus particle. For each mesh point, the torque ($T_{dL}(i)$) was equated to the product of the electrostatic force ($F_{dL}(i)$) and the distance of the projected mesh point from the center of the particle (d) (**Figure 4.1b**):

$$P_{dL}(i) = 64C_{\infty}kT\tanh\left(\frac{e\zeta_s}{4kT}\right)\ \tanh\left(\frac{e\zeta_{mp}(i)}{4kT}\right)\exp\left(-\kappa h_{dL}(i)\right) \quad (4.4)$$

$$T_{dL}(i) = P_{dL}(i)A(i) \times d \quad (4.5)$$

where P_{dL} is the electrostatic double layer repulsion pressure of the substrate and projection of curved mesh area ($A(i)$), ζ_{mp} is the zeta potential of the flat projected

surface of a mesh point, h_{dL} is equal to substrate distance from the mid-point of the curved meshed surface ($h_{dL} = h_p + L/2$). The total torque was calculated by summing contributions from each projected flat surface area. The sum of clockwise and counter-clockwise torques at each time step provided the electrostatic torque on the Janus particle:

$$T_{dL-total} = \sum T_{dL}(i) \tag{4.6}$$

where $T_{dL-total}$ is electrostatic torque between the Janus particle and the substrate.

The gravitational torque on a Janus particle originates from the density distribution mismatch between the cap and native particle. Although gravitational deterministic torque affects the rotation of the particle about an axis parallel to the substrate, there is no impact on the rotation of the particle about the z-axis (see **Figure 4.1**) because of the particle's axisymmetric geometry. Note that for the work summarized herein, we assumed the coating thickness distribution to be uniform over the contour of the particle. The weight of right and left hemispheres of the Janus particle was calculated at each time step with respect to a dynamic spherical coordinate system and a vertical plate that passes through the particle center. The gravitational torque was calculated:

$$T_{G-total} = (\text{weight\_Cap}_{right} - \text{weight\_Cap}_{left}) \times w_{CoM} \tag{4.7}$$

$$\text{weight\_Cap}_{right} = Total\ cap\ weight \times \frac{2\Theta+\pi}{2\pi} \tag{4.8}$$

$$\text{weight\_Cap}_{left} = Total\ cap\ weight - \text{weight\_Cap}_{right} \tag{4.9}$$

$$w_{CoM} = \frac{2a}{\pi \times \sin(\alpha)} \times \left(\frac{\alpha}{2} + \frac{\sin(2\alpha)}{4}\right) \tag{4.10}$$

where w_{CoM} is the center of mass (**Figure 4.1b**) and α is half of the angle swept out by the non-canceled portion of the cap (**Figures 4.1b, 4.1c, & 4.8**). Note from **Figure 4.1** and **equations 4.7) – 4.10** that particle symmetry was utilized to calculate torque. The

portion of the non-cancelled cap, swept out by the angle 2α, was the body contributing to gravitational torque, while the remaining cap and hemispheres of the native particle cancelled. To calculate center of mass of the cap we used a geometrical method. The geometry required for the center of mass in the torque calculation was that of a semi-hollow hemisphere (**Figure 4.2**). The axisymmetric nature of the relevant geometry allowed for the center of mass to be obtained at some position along the x-axis. A cut of the cap was required to account for the non-canceled torque of the Janus particle when rotated away from $\theta = 0°$ or $\theta = 180°$. Finally, the cap thickness was small enough as compared to the particle radius that it was neglected in center of mass calculations. The center of mass was calculated by:

$$w_{CoM} = \frac{\int x\, dm}{M} = \frac{\int x\, dA}{\int dA} \tag{4.11}$$

Where dm is a differential mass element, M is total mass, dA is a differential surface area element, and A is the total surface area. By replacing x and dA values with the expressions found in **Figure 4.2**, w_{CoM} was calculated:

$$\frac{\int_0^{\alpha}\int_0^{\pi} a\cos\psi \sin\varphi\; a\, d\psi\; a\cos\psi\, d\varphi}{\int_0^{\alpha}\int_0^{\pi} a\, d\psi\; a\cos\psi\, d\varphi} \tag{4.12}$$

The result following integration is the center of mass:

$$w_{CoM} = \frac{2a}{\pi \times \sin(\alpha)} \times \left(\frac{\alpha}{2} + \frac{\sin(2\alpha)}{4}\right) \tag{4.13}$$

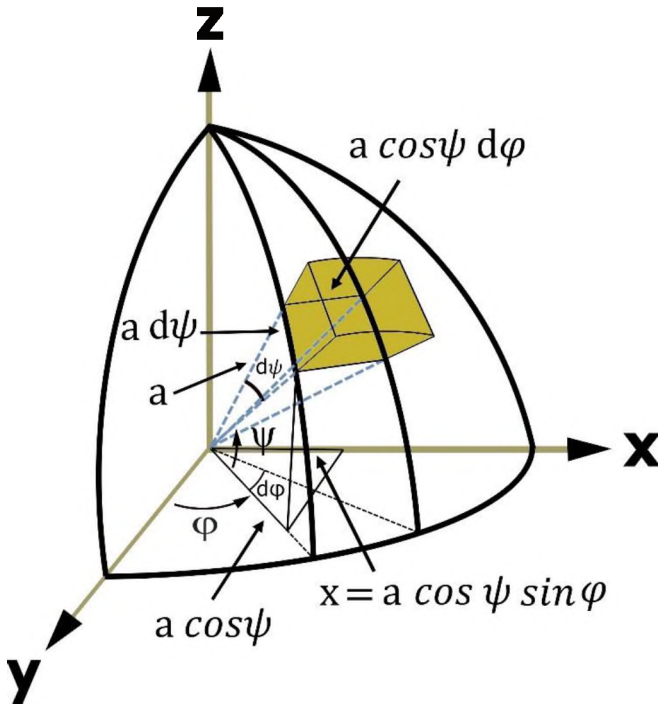

Figure 4.2. A schematic of a semi-hollow hemisphere.

4.2.2 Near-boundary diffusion coefficients

Although hydrodynamic hindrance from the nearby boundary will occur in all translational (x, y, z) and orientational (θ, ϕ) directions (see **Figure 4.1**), we are primarily concerned with hindrance in the polar rotational (θ) and translational direction normal to the substrate (z). A solution of the Stokes equation is necessary to account for the bounding effect of the wall on hydrodynamic interactions. Goldman et al.[153] provided an infinite-series solution for this equation. The normal translational diffusion coefficient of a spherical particle can be computed by an approximation of the Goldman infinite-series solution by a regression[15]:

$$D_z = \frac{kT}{f_\infty} q(h) = \frac{kT}{6\pi\eta a} q(h) \tag{4.14}$$

$$q(h) = \frac{6h^2+2ha}{6h^2+9ha+2a^2} \tag{4.15}$$

where T is temperature, k is Boltzmann constant, η is the fluid viscosity, f_∞ is the friction coefficient ($f_\infty = 6\pi\eta a$), and $q(h)$ is the wall correction factor.

Dean and O'Neill[68] considered the polar rotation of a bounded sphere about an axis parallel to the planar surface. Goldman[70,71,153] updated the Dean and O'Neill solution and numerically computed the solution in form of dimensionless force and torque on a rotating sphere. We previously fit several gap ranges to implement the corrected Dean and O'Neill expression based on the numerical fit from Goldman.[38] The comprehensive polar rotational diffusion coefficients are as follows:

$$D_{r,\theta} = \frac{kT}{f_{r,\infty}} / q^{\theta}(h) = \frac{kT}{8\pi\eta a^3} / q^{\theta}(h) \tag{4.16}$$

$$q^{\theta}(h) = 0.9641 \left(\frac{h}{a}\right)^{-0.1815} \qquad \frac{h}{a} \leq 0.6 \tag{4.17}$$

$$q^{\theta}(h) = 1.056 \left(\frac{h}{a}\right)^{-0.07286} \qquad 0.6 \leq \frac{h}{a} \leq 2 \tag{4.18}$$

$$q^{\theta}(h) = 1 \qquad \frac{h}{a} > 2 \tag{4.19}$$

4.2.3 Brownian dynamic simulation (BDS).

We carried out Brownian dynamics simulations to track rotational and z-axis translational motion of a Janus particle. The Langevin equation with a thermal fluctuating force, conservative forces, hydrodynamic forces, as well as torques, was used to formulate a stepping algorithm for the Janus particle. A well-known inertia-less numerical solution was obtained by Ermak and McCammon[72] to solve the Langevin equation at small Reynolds numbers. This numerical solution was used to predict the dynamic behavior of a single particle and consequently track the position of the particle at consecutive time steps. The z-axis translational and polar rotational trajectories of a single particle were predicted via Ermak and MaCammon stepping algorithm:

$$h(t + \Delta t) = h(t) + \frac{dD_z}{dh}\Delta t + \frac{D_z}{kT}F\Delta t + H(\Delta t) \tag{4.20}$$

$$\theta(t + \Delta t) = \theta(t) + \frac{D_{r,\theta}T_{det}\Delta t}{kT} + G(\Delta t) \tag{4.21}$$

These stepping algorithms are valid when the time step (Δt) is longer than the momentum relaxation time of the particle and is short enough such that the system properties are constant. The momentum relaxation times for the colloidal particles in the range of particles we use in our simulation are in the order of 10^{-6}s[154]. In the z-axis translational algorithm, F represents conservative forces on the particle and H, which has $\langle H^2 \rangle = 2D_z \Delta t$ variance, is the Gaussian random fluctuation due to Brownian motion. The total force F was the sum of the double layer repulsion and gravity. In the polar rotational algorithm, T_{det} is the deterministic torque, which may include contributions from a mismatch in electrostatic forces near the Janus boundary and gravitational force due to a mismatch in the density of the cap and particle. $G(\Delta t)$, which has $\langle G^2 \rangle = 2D_{r,\theta} \Delta t$ variance, is Gaussian random rotation due to the stochastic torque. Electrostatic torque results from the asymmetry in electrostatic force arising when the Janus boundary separating the two hemispheres of different properties rotates towards the wall ($\theta = 90°$). The gravitational torque depends on the polar orientation of the particle and the weight of the cap, which in turn depends on the thickness, total size, and cap material. Note that although the stepping algorithms are uncoupled, height (Eq. 4.20) and rotation (Eq. 4.21) may have synergistic effects. The height of the particle will impact rotation by effecting the rotational diffusion coefficient, electrostatic and rotational stochastic torques. Also, the orientational position of the particle will impact z-axis translational by affecting the electrostatic force between the particle and the substrate.

A MATLAB code was developed to implement the Brownian dynamics simulation for our system (**APPENDIX 4.1**). Zeta potential is a key factor in calculating electrostatic double layer repulsion force between colloidal particles and surrounding media. We addressed the challenge of accounting for variations in zeta potential with

an existing meshing method[38] in which the sphere was divided into small parts in both the azimuth (φ) and polar (θ') angles. Each small meshed region has its own value of zeta potential; the small curved area was projected parallel to the boundary. The electrostatic force was calculated between each small projected flat surface and the substrate. The sum of the electrostatic interactions between the small projected area and the substrate is the double layer electrostatic force between the particle and the substrate. At each time step, this force was calculated as one of the conservative forces (F) in Equation 4.20. Finally, the time step for each simulation was set as $\Delta t = 5$ ms. For all the system conditions studied here, the stepping algorithms were run 10 times each for 4.8×10^6 time steps. The number of observations at each separation height or orientation is the average of 10 sets of simulations. In all simulations the Janus particle cap includes a 2.5 nm titanium as a sublayer in addition to the reported gold layer thickness. Experiments regularly include a thin layer of titanium to increase adhesion of a gold coating on a polystyrene particle. A summary of simulation conditions and particle properties is provided in **Table 4.1**.

TABLE 4.1. Simulation conditions and particle properties used in the study.

Property Name	Value
Particle diameter	1 μm – 6 μm
Particle material	Polystyrene
Polystyrene Density	1.055 gr^1cm^{-3}
Gold coating thickness	2 nm – 20 nm
Gold density	19.32 gr^1cm^{-3}
Titanium Density	4.5 gr^1cm^{-3}
Temperature	298.15 K
Electrolyte concentration	1 mM
Debye length	9.6 nm
Time step	5 ms
Initial orientation position	π/2
Number of time steps	4.8×10^6
Surface zeta value	-50 mV
Particle coated side zeta value	-5 mV
Particle un-coated side zeta value	-50 mV
Number of iterations for each simulated condition	10

4.3 RESULTS & DISCUSSION

4.3.1 Influence of deterministic torque on particle rotation dynamics.

We defined a dimensionless rotation number (DRN - $\widehat{\boldsymbol{\theta}}$) that balances the deterministic and stochastic torques:

$$\widehat{\boldsymbol{\theta}} = \frac{\Delta\theta_{det}}{\Delta\theta_{sto}} \tag{4.22}$$

where $\Delta\theta_{det}$ and $\Delta\theta_{sto}$ are the rotational displacements of the Janus particle in the polar direction due to deterministic and stochastic torques, respectively. This dimensionless number furnished a direct quantitative measure of the relative influence of deterministic torque as compared to stochastic torque on the particle. Note also that the DRN is a dynamic quantity, in that it will depend upon the time step. Thus, the proceeding comparison is applicable to the time step conditions we tested herein.

Stochastic rotational fluctuations dominate at small values of DRN, while deterministic fluctuations become more relevant at large values of DRN. We calculated the DRN to compare fluctuations from gravitational and stochastic torque absent of

hydrodynamic hindrance as a function of particle size. The expression for calculating the deterministic rotational displacement is:

$$\Delta\theta_{det}(\Delta t) = \frac{D_{r,\theta\_Bulk} < T_{det} > \Delta t}{kT} \quad (4.23)$$

where $< T_{det} >$ is the average deterministic torque over 180 orientations and D_{r,θ_Bulk} is rotational diffusion coefficient in the bulk, ensuring that this DRN will be height independent. Torque, $< T_{det} >$ was obtained by uniform averaging over 180-degree in the (clockwise) orientation according to Equation 4.10. We used the standard deviation $\sqrt{\langle G^2 \rangle} = \sqrt{2\mathrm{D}_{\mathrm{r},\theta}\Delta\mathrm{t}}$ for calculating the random torque on the rotation of the Janus particle (Eq. 21) as the stochastic contribution. Further, DRN was developed to approximate the impact of gravitational force, thereby neglecting electrostatic torque. However, the later effect was included in all subsequent calculations found in this paper, although previous work has shown electrostatic torque to be small[38].

Figure 4.3a shows the impact of stochastic torque embodied in the rotational displacement experienced by a Janus particle as a function of diameter and with a gold cap thickness of 20 nm. Increasing the diameter of the particle induced a decrease in the fluctuations arising from stochastic torque because of the correlation between the diameter of the Janus particle and rotational diffusion coefficient (see $G(\Delta t)$ term of Eq. (4.21)). The characteristic fluctuations arising from deterministic torque were calculated for the same conditions. Deterministic torque had a qualitatively similar impact on rotation as stochastic torque (see **Figure 4.3b**); the magnitude of rotation decreased with increasing particle diameter at fixed cap thickness. However, deterministic torque decreased more slowly with increasing diameter as compared with stochastic torque. The origin of this trend for deterministic torque is in the competing effects of diameter on rotational displacements. The rotational diffusion coefficient (see Eq. 4.23) decreased with increasing diameter, but the magnitude of deterministic torque

increased with increasing diameter due to both the growth of cap weight and displacing this weight further from the center. **Figure 4.3c** shows the DRN, which is the quotient of values summarized in **Figures 4.3a & 4.3b**. The positive slope of DRN as a function of diameter indicates that deterministic torque had an increased influence as the diameter of the particle increased.

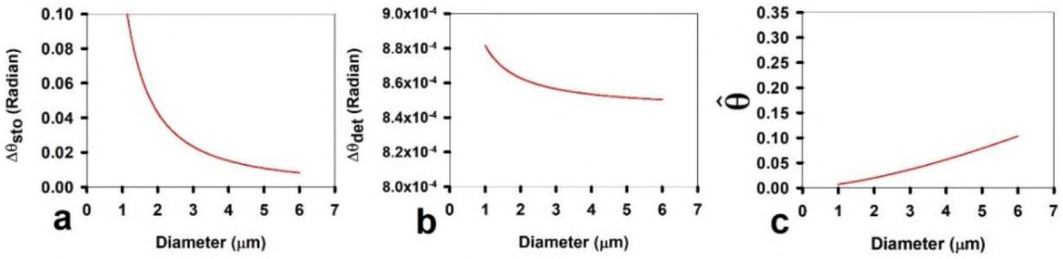

Figure 4.3. Calculations for the fluctuations arising form (a) stochastic torque, (b) deterministic torque, and (c) the balance of these two torques via the dimensionless rotation number (DRN) on a Janus particle with a cap of 2.5 nm titanium and 20 nm gold. The reader should note the difference in y-axis range of (a) and (b) figures. These data show that although both fluctuations arising from stochastic and deterministic torque decreased with increasing diameter, fluctuations from deterministic torque decreased more slowly as a function of diameter. Deterministic torque, which induces rotational quenching of the Janus particle, became more important as particle size increased.

We measured mean squared angular displacement (MSAD) from our Brownian dynamics simulations to track the influence of the cap on a quantity now regularly obtained from experiments. The MSAD can be calculated by $\langle \Delta\theta^2(t) \rangle = \langle [\theta(t + dt) - \theta(t)]^2 \rangle$ relation[140,155,156]. The MSAD results for Brownian Dynamic simulation data for particles with and without cap is shown in **Figure 4.4.** First, for both coated and non-coated particles, increases in the size of particles caused a shift in the magnitude of the MSAD to lower values. However, the shape of MSAD was significantly different for coated and non-coated particles. The MSAD is a straight line on the log-log plot shown in **Figure 4.3** for non-capped particles. However, the MSAD for capped particles has a shoulder indicative of quenched rotation. Also, the size of the

particle affects the start location of the shoulder. The start points shift to lower scaled lag time as the size of the particle increases.

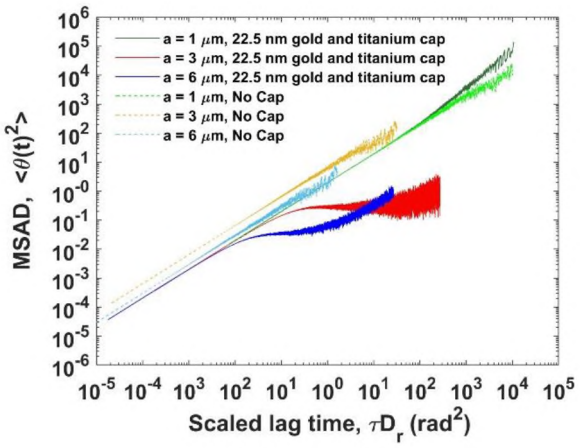

Figure. 4.4. Angular motion of the spherical particles with and without a cap. The MSAD analysis results for capped and no-capped particles can be differentiated by their color. The evaluated particles are 1 μm, 3 μm and 6 μm. The τ parameter refers to lag time.

4.3.2 Probability and potential energy landscapes for a Janus particle with cap of non-matching density.

Data summarized in the previous section suggest that deterministic torque is relevant to the dynamics of a Janus particle near a boundary. The outcome of such relevance is that the probability of finding a Janus particle at a given state will be altered by the deterministic torque. The probability density of translational and orientation states was obtained to assemble a histogram and subsequently calculate the effective interaction landscape experienced by the Janus particle under various conditions. **Figures 4.5a – 4.5c** summarize data showing the impact of various parameters on the polar orientation of a Janus particle. The number of observations reported in these figures is that of a cap-down orientation, which corresponds to the 'quenched' state. Stronger quenching is associated with a larger number of observations at $\theta = 180^{o}$. As shown in the previous section, the particle diameter at a fixed cap thickness had a strong

effect on rotational quenching (see **Figure 4.5a**). The number of observations at θ = 180° increased as the diameter was increased. Increasing the coating thickness increased the number of observations at θ = 180° (see **Figures 4.5b & 4.5c**). Both figures demonstrate the critical importance of changes in cap weight to rotational quenching of a Janus particle. Larger particle diameters and thicker caps enhance the influence of deterministic torque, thereby increasing the probability of a rotationally quenched Janus particle.

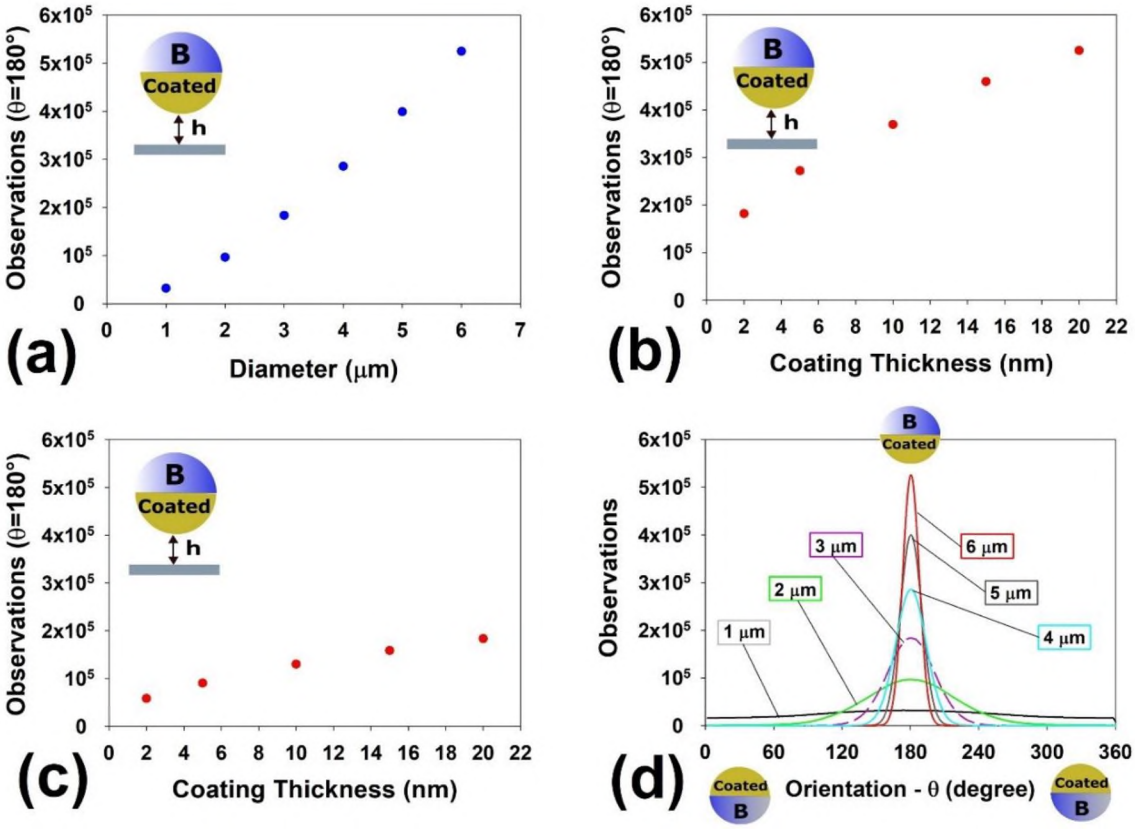

Figure 4.5. (a) Impact of particle size on the number of observations for a particle with cap oriented downward (BDS - C_{th} is 20 nm gold and 2.5 nm titanium). (b) Coating thickness impact on the number of observations for a particle with cap oriented downward (BDS - 6 μm). (c) Coating thickness impact on the number of observations for a particle with cap oriented downward (BDS - 3 μm). (d) Number of observations at different orientations for various particle sizes and same coating thickness (4.8 m iterations - BDS - C_{th} is 20 nm gold and 2.5 nm titanium). – **B** referred to the uncoated side. The angle bin-size is number of observation evaluation is 1-degree.

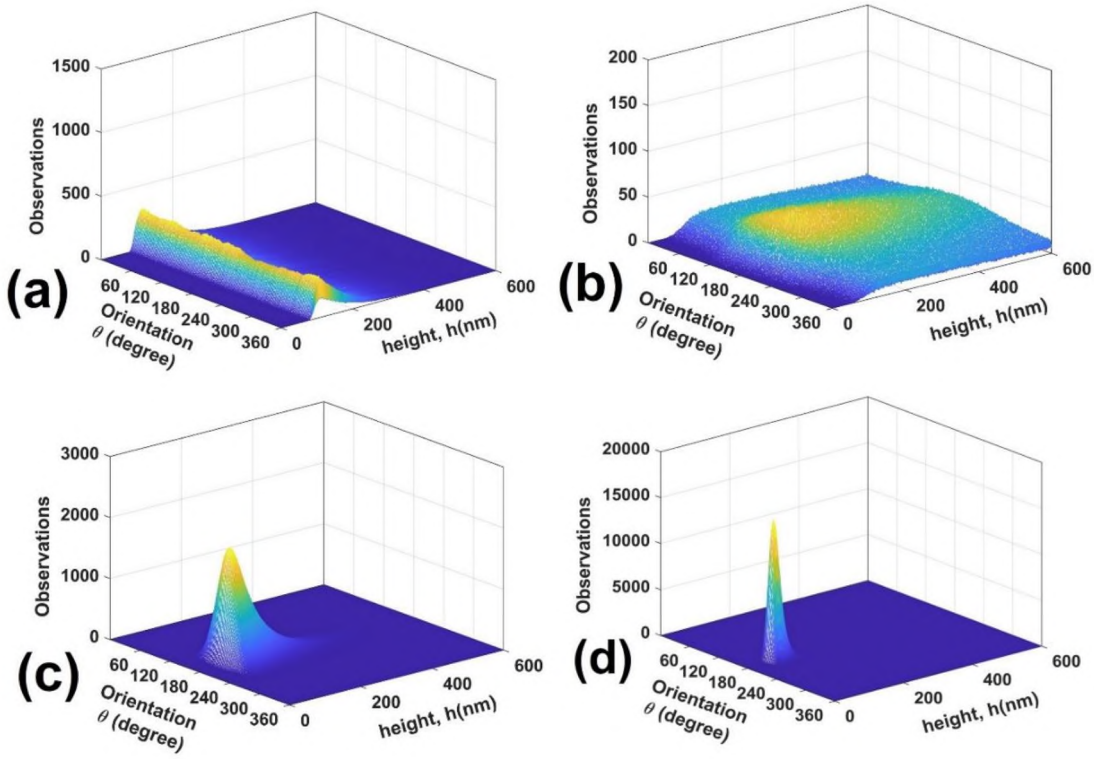

Figure 4.6. (a) Histogram landscape for non-Janus 6μm colloid particle, and histogram landscape for Janus particles with 2.5 nm titanium and 20 nm gold coatings at different diameters: (b) 1 μm. (c) 3 μm. (d) 6 μm. The height here refers to the separation distance between the particle and the substrate. The reader should note the difference in the y-axis scale.

Figure 4.6 shows a histogram landscape of observations in separation distance and orientation. Note the significant change in probability density for variation in particle size from 1 μm (**Figure 4.6a**) to 6 μm (**Figure 4.6c**) with the same coating thickness. The distribution of states spreads across all orientations for a Janus particle of 1 μm diameter and 20 nm cap thickness, meaning the Janus particle is only weakly quenched at these conditions. However, merely increasing the particle diameter to 3 μm and then 6 μm induces orientational states that are highly populated around $\theta = 180^0$. Deterministic torque became increasingly important at larger diameters due to the mismatch in the cap and particle core densities. This behavior is in contrast with the 1

μm diameter particle, which experienced random rotation such that orientational states are distributed across all available θ.

As was done previously for separation distance observations of isotropic spheres[64], observations of position and orientation were used to calculate the potential energy landscape for a Janus particle. Histogram landscapes shown in the previous section were interpreted to obtain the potential energy of interaction for a Janus particle with a cap of non-matching density. In the BDS, we used a non-coupled translational-rotational Langevin equation to solve BDS. The single spherical particle of our model system allows us to neglect translational and rotational coupling motion. As the translational and rotational are not coupled so the probability of finding a Janus particle at a particular separation distance and orientation can be independent.

We assumed the probability of finding a Janus particle at a particular separation distance and orientation was independent and equal to the product of those individual probabilities:

$$p(h,\theta) = \underbrace{A_h e^{-\phi_h/kT}}_{p_h}\underbrace{A_\theta e^{-\phi_\theta/kT}}_{p_\theta} = Ae^{-\phi_c/kT} \tag{4.24}$$

where ϕ_h is the potential energy associated with changes in separation distance, ϕ_θ is the potential energy associated with changes in orientation, ϕ_c is the total colloidal potential energy ($\phi_c = \phi_h + \phi_\theta$), and A is a normalization constant chosen such that the cumulative probability summed over all states equals 1. Equation 4.24 can be rearranged and the normalization constant eliminated by subtracting the potential energy of the most probable state $\phi_c(h_m, \theta_m)$, where h_m and θ_m are the most probable separation distance *and* orientation corresponding to a maximum in the probability density landscape. Thus, the potential energy landscape was calculated by:

$$\frac{\phi_c(h,\theta)-\phi_c(h_m,\theta_m)}{kT} = \ln\frac{n(h_m,\theta_m)}{n(h,\theta)} \tag{4.25}$$

where $n(h_m, \theta_m)$ is the maximum number of particle observations among all heights and orientations, $\phi_c(h_m, \theta_m)$ is the potential energy at 'most probable' position and orientation, $n(h, \theta)$ and $\phi_c(h, \theta)$ are the number of particle observation and potential energy respectively at some specific height and polar orientation.

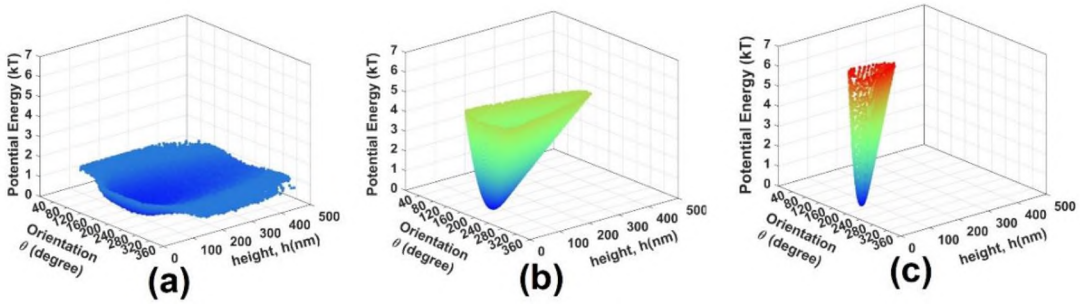

Figure 4.7. (a) Potential energy landscape of 1 μm particle with 2.5 nm titanium and 20 nm gold cap. (b) Potential energy landscape of 3 μm particle with 2.5 nm titanium and 20 nm gold cap. (c) Potential energy landscape of 6 μm particle with 2.5 nm titanium and 20 nm gold cap

Figure 4.7 shows the potential energy landscape for a Janus sphere of varying diameter and 20 nm gold cap. In **Figures 4.7b & 4.7c**, there is a minimum potential energy configuration belonging to the location of maximum observations among all orientations, corresponding to the coated side facing the wall. Comparing these three profiles, from a particle with diameter 1 μm to one with diameter 6 μm, illustrates the impact of a cap on conservative interactions. The potential energy landscape for a particle of 1 μm diameter nearly matches that of a Janus particle with density matching cap. Larger particle diameters with correspondingly larger gravitational torques have landscapes with a clear minimum. A colloidal particle will typically only sample states of a few kT. The projected two-dimensional view of the energy landscapes then shows how the presence of a cap will restrict the sampled states of a Janus particle. Increasing particle diameter at constant cap thickness severely limited the available orientations of the particle for a fixed energy state (see **Figure 4.8**). Although a 1 μm particle with 20 nm thick cap will sample most orientations, a 6 μm particle with the same cap thickness

will sample only a fraction of possible orientations. Variations of potential energy landscapes for Janus particles of different particle size will help to explain observations of stable and unstable positions for a coated particle.

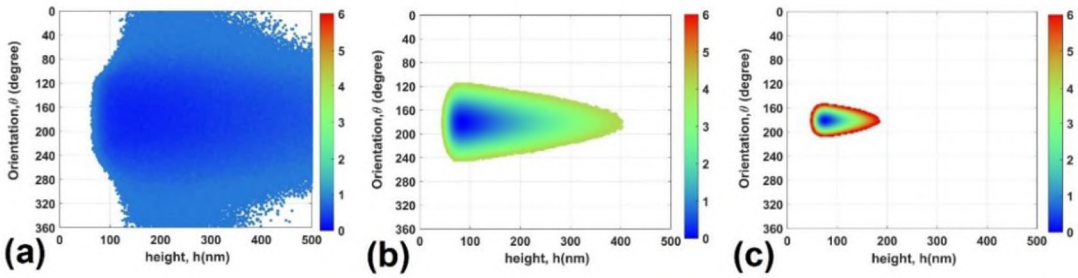

Figure 4.8. (a) 2D cut away panel of BDS Potential Energy landscape of 1 μm PS with 2.5 nm titanium and 20 nm gold cap. (b) 2D cut away panel of BDS Potential Energy landscape of 3 μm PS with 2.5 nm titanium and 20 nm gold cap. (c) 2D cut away panel of BDS Potential Energy landscape of 2.5 nm titanium and 6 μm PS with 20 nm gold cap.

4.4 Conclusion

Brownian dynamics simulations were used to predict the rotational and translational displacements of a Janus particle with cap of non-matching density. These simulated data provided evidence that gold caps of thickness 5 nm – 20 nm on particles of diameter 1 μm to 6 μm may strongly influence the rotational dynamics of the particle. Cap-down or 'quenched' orientations arise when the balance of deterministic and stochastic torque is dominated by the former. Deterministic torque arising from the weight of the cap depended on particle size and cap thickness. Our parametric variation found that at experimentally relevant particle sizes (> 1 μm) or cap thicknesses (> 5 nm), the particle was strongly quenched such that most observations of orientation were in the cap-down state. Further, histogram landscapes were inverted to calculate the potential energy landscape for Janus particles. The energy landscapes showed that Janus particles of typical size and coating thickness will sample only a limited number of orientation states. These simulations and associated analysis revealed the importance of considering the cap weight of a Janus particle, especially when designing new

materials and developing new applications that rely on particle dynamics or transport. Further, Janus particles have also been suggested as probes of local rheology and mechanics of material. The phenomena described herein should be taken into account when utilizing Janus particles in this manner.

CHAPTER V

INTERPERETING THE MORPHOLOGY OF EVANESCENT WAVE SCATTERING FROM AN ELLIPSOID

5.1 Introduction

Anisotropic colloid particles have garnered the attention of scientists and engineers in recent years[131,157–163]. Colloidal particles with non-uniform features, from surface chemistry to non-spherical shape, are considered anisotropic. The potential application of these particles in advanced materials has ignited interest among researches in academic institutions and industry[148,164–167]. Many research groups are now able to synthesize various types of anisotropic particles for different purposes. For example, in some studies, scientists can synthesize colloidal muscle-like fibers of Janus ellipsoids by self-assembly[17]. Janus particles with dissimilar hemispheres have been used to stabilize interfaces. In one study, mushroom-like Janus polymeric particles as a surfactant were used to stabilize 1-octanol-in-water emulsion droplets[18]. In another study, a silica-based Janus particle[21] with hydrophilic and hydrophobic domains was used to strongly stabilize a foam.

Colloidal interaction forces play an important role in determining the properties of a variety of macroscopic material properties such as performance, stability, storage life, and rheology of suspensions. Forces relevant to colloidal suspensions are either

conservative or non-conservative. Conservative forces are path independent, while non-conservative or dissipative forces are path-dependent. Typically encountered conservative colloidal interaction forces are electrostatic double-layer repulsion, van der Waals dispersion interactions, solvation or hydration force, hydrophobic force, depletion interaction, steric force, and gravity[48,168,169].

Techniques for measuring colloidal scale surface forces are necessary to engineer and develop new and better-performing materials. Multiple experimental techniques, including atomic force microscopy (AFM)[42], the surface force apparatus (SFA)[43], confocal microscopy[36], holographic microscopy[37], and Total Internal Reflection Microscopy (TIRM), have been developed over the past few decades to probe these interactions. AFM and SFA, modified with a colloidal probe, are robust techniques that have been widely adopted to measure surface forces between the probe and a substrate[31]. Similarly, TIRM has been developed to measure the surface force experienced by a single colloidal particle immersed in a liquid nearby, but not adhered to, a substrate[32]. TIRM tends to be more sensitive than AFM and SFA because TIRM uses a 'thermal' energy scale (i.e., ~ kT, k is Boltzmann's constant). In contrast, AFM and SFA operate on a mechanical energy level (i.e., ~ $k_S X^2/2$, k_S is the cantilever spring constant)[31]. Unfortunately, none of these techniques are easily adapted for measuring surface forces for anisotropic particles; AFM, confocal microscopy, and conventional TIRM are designed for measuring dynamics and forces for spherical isotropic particles.

Physical and chemical asymmetric properties of anisotropic particles induce forces associated with them (ex. electrostatics) to become orientation dependent. The central goal of my Ph.D. research was to develop an experimental methodology and design for conducting TIRM on anisotropic particles. For this purpose, I chose an ellipsoidal as a model particle to develop a TIRM system suitable for anisotropic

particles. In the first part of this chapter, I describe a conventional TIRM system and initial benchmarking experiments conducted in our lab. In the next section, I describe a working hypothesis that drove the development process for a new TIRM technique called "Scattering Morphology Resolved – TIRM" (SMR – TIRM) as well as a methodology to create this technique. Finally, I described the experimental efforts, results, and conclusions.

5.2 Conventional Total Internal Reflection Microscopy

Total Internal Reflection Microscopy (TIRM) is an optical technique that has been developed over the past few decades to directly and sensitively probe colloidal surface force interactions between a single mobile colloidal particle immersed in a liquid and a flat substrate. The surface forces could be as weak as a few ~kT. The essence of TIRM is in measuring fluctuations of a single colloidal particle under the influence of stochastic or Brownian motion normal to the nearby substrate[31,32,45].

Conventional TIRM is conducted on a chemically isotropic sphere to measure a variety of ~kT scale interactions. For instance, over the last few decades, scientists have successfully measured depletion interactions[49], electrostatic double-layer repulsion[46], van der Waals attraction,[170] steric interactions[48]. Recently, the application of TIRM has been expanded to measure colloidal interactions at liquid-liquid interfaces and biological systems. Helden et al.[52] applied TIRM to evaluate the dynamic behavior of solid colloid particles and oil droplets in the oil-water interface. Scientists have even used evanescent waves to observe the detachment and separation distance of bacterial cells from a substrate[171]. Swavola et al. mimicked bovine serum albumin and a mucus system in the format of a coated particle and a substrate and applied TIRM to measure

their interaction[172]. These studies illustrate the utility of TIRM as a tool for surface force measurement.

The basic feature of TIRM is that it tracks the motion of a particle normal to the substrate. As detailed in future paragraphs, analysis of these dynamics allows for the direct measurement of ~kT scale colloidal interactions. Accurate tracking of particle fluctuations normal to the boundary facilitates calculation of the potential energy curve sampled by the particle.

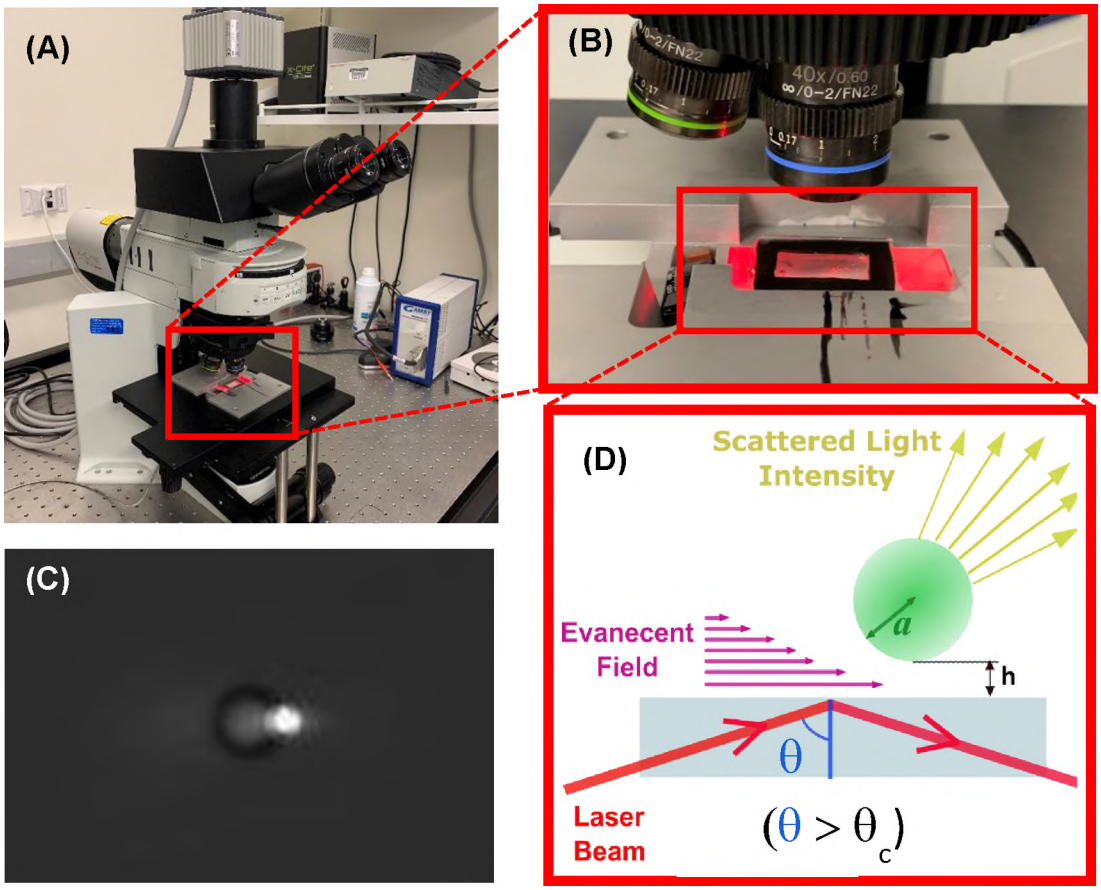

Figure 5.1 Total Internal Reflection Microscopy. (A-B) experimental apparatus for TIRM. (C) 6 μm polystyrene (PS) spherical particle illuminated by an evanescent wave. (D) Schematic figure of a TIRM system.

TIRM utilizes an evanescent wave, which arises as a consequence of optics described by Snell's law. In Snell's law, when electromagnetic waves traveling in the first medium approaches an interface, part of the incident wave is reflected in the first

medium, and a refracted wave arises in the second medium. When the incident angle is bigger than the critical angle (Fig. 5.1D), the refracted wave disappears, the incident totally reflected in the first medium, and an evanescent wave parallel to the interface is created in the second medium. The critical angle can be defined as:

$$\theta_C = \sin^{-1}\frac{n_2}{n_1} \tag{5.1}$$

Where θ_C is the critical angle, n_2 and n_1 are the refractive indices of the first and the second mediums, respectively. One significant difference between an evanescent wave and a propagating wave is that an evanescent wave decays exponentially, which limits its travel in different mediums. An evanescent wave has a broad range of applications. It is used in dynamic light scattering[173], infrared spectroscopy[174], fiber- optic biosensors[174], and many others. TIRM works by utilizing the evanescent wave or total internal reflection phenomena concept (see **Fig. 5.1**).

The intensity of light scattered by a particle very near that interface depends sensitively on the separation distance:

$$I = I_0 e^{-\beta h} \tag{5.2}$$

where I_0 is the intensity of light scattered from a particle at h = 0 (i.e., stuck to the surface) and β is the inverse decay length, which is a function of the incident angle of the laser beam and material of the substrate. The inverse decay length is defined as:

$$\beta = \frac{4\pi}{\lambda}\sqrt{(n_1 \sin\theta_1)^2 - n_2^2} \tag{5.3}$$

where λ is the incident laser wavelength. The decay length (β^{-1}) or penetration depth represents the depth that the evanescent wave can diffuse in the second medium. As the exponential equation is sensitive to the height, extremely minimal changes in height results in a measurable change in the intensity. Light scattered from the particle is

typically collected by either a photomultiplier tube (PMT) or a charge-coupled device (CCD) camera.

The potential energy of the particle at each height is calculated by assuming the particle samples a Boltzmann distribution of heights. Boltzmann's equation is given by:

$$p(h) = A \exp(-\frac{\emptyset(h)}{kT}) \quad (5.4)$$

where p(h) is the probability density function at heights in the range of h and h + dh, $\emptyset(h)$ is the potential energy profile at that range, and kT is the thermal energy. The shape of the histogram of the probability density function is similar to the shape of the histogram of intensity N(I). The probability of finding a particle at a specific height $(p(h)\,dh)$ is similar to (but not exactly the same as) the intensity probability $(p(I)\,dI)$ at the particular range of the intensity. According to the mentioned relationship between the probabilities, we can write:

$$\frac{p(h)}{p(h_2)} = \frac{P(I(h))}{P(I(h_2))}\frac{I(h)}{I(h_2)} \quad (5.5)$$

In this equation, the ratio of $\frac{P(I(h))}{P(I(h_2))}$ is equivalent to the ratio of the number of intensity observation at the specific range of the height ($\frac{N(I(h))}{N(I(h_2))}$). By using Boltzmann's equation (Eq. 5.3), equation 5.5 and replacing of the probability of the intensity ration with intensity ratio observation, the potential energy profile (Eq. 5.6) is deduced from a TIRM experiment by:

$$\frac{\emptyset(h) - \emptyset(h_m)}{kT} = \mathrm{Ln}\,\frac{N(I_m)I_m}{N(I)\,I} \quad (5.6)$$

where I_m is the intensity of the particle in a reference position, which corresponds to the minimum in the potential energy profile. I and N(I) are intensity and number of observations of the particle in the particular height, respectively[44]. **Figure 5.2** shows the sequence of collecting raw intensity data (Fig. 5.2A), converting the raw data to the number of observation histogram (Fig. 5.2B), and finally deduction of potential energy profile from the histogram (Fig. 5.2C).

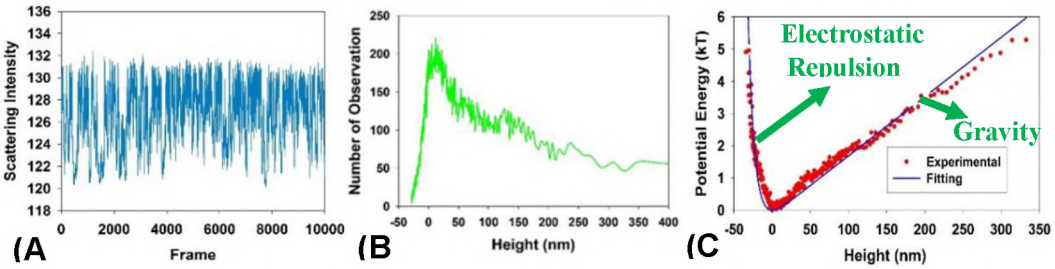

Figure 5.2. (A) Raw experimental scattering data for a 6μm (PS) sphere collected by CCD camera in 10000 frames. (B) The histogram of the number of observations. (C) The potential energy profile calculated from the data shown in (A). "0 nm" relative height equals the most probable height.

TIRM is one example of "near-field" or "ultra-microscopy." For a microscopic scale particle near a boundary in a liquid under the influence of surface forces, we expect the particle to move in the range of ~nanometers after each momentum relaxation time. One significant restriction currently imposed by TIRM is that the particle needs to be a sphere and chemically uniform. The research objective of this dissertation is to extend the capabilities of TIRM to measure the interaction energy between an anisotropic colloid and a flat plate.

5.3 Hypothesis and Methodology

Conventional TIRM is not suitable for measuring interactions of anisotropic particles because these interactions are functions of both separation distance and orientation. In conventional TIRM, the integrated intensity of scattered light is

collected. However, such an integrated signal is not suitable for an anisotropic system because orientation information is lost. For this purpose, according to the primary results, the working hypothesis to conduct TIRM on anisotropic colloids is that the morphology of scattered light from an anisotropic particle is a sensitive function of orientation and shape of the particle. This morphology represents the scattered light intensity value and its pattern. In **Figure 5.3**, the scattered light morphology and pattern differences between a stuck spherical particle and a stuck ellipsoidal particle is detectable.

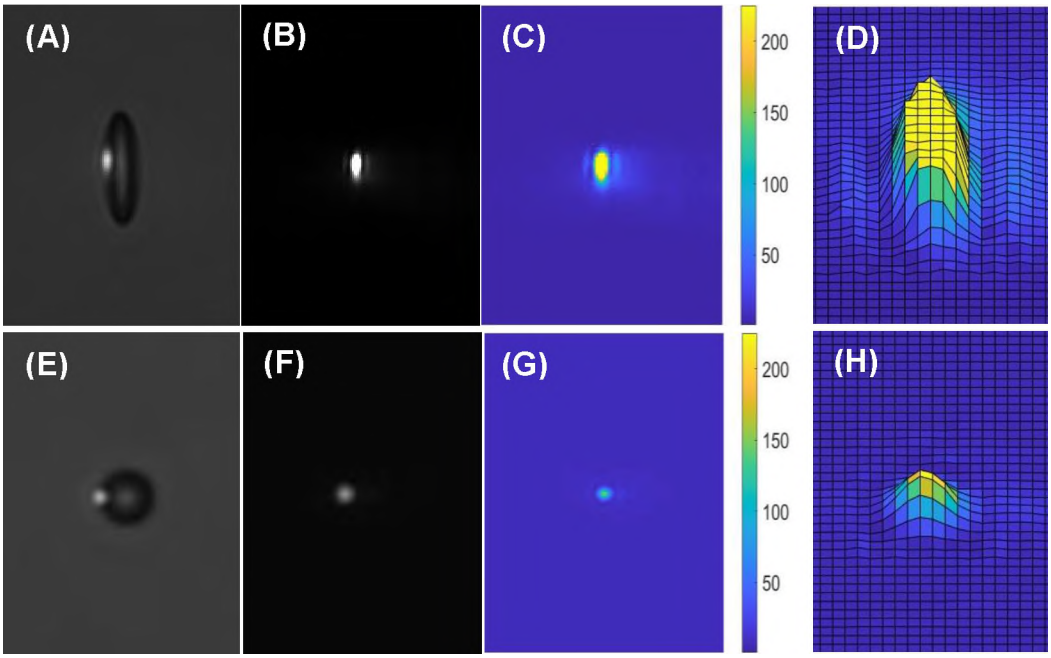

Figure 5.3. Scattering light from the ellipsoid particle at Evanescent field (A) with backlight (B) without backlight (C) without a backlight and intensity distribution pattern (D) Morphology of the image without backlight, Scattering light from the spherical particle at Evanescent field (E) with backlight (F) without backlight (G) without backlight and intensity distribution pattern (H) Morphology of the image without backlight.

To directly measure the ~kT scale interaction energy between a spheroidal particle and a flat surface by the novel TIRM experiment technique, we first aim to understand the scattering morphology of ellipsoidal particles deposited on a substrate. The hypothesis is that we can decode the particle orientation from the scattering

morphology. For this study, I chose the ellipsoid polystyrene particle as a model system. A two-step approach is used to analyze the scattering morphology information. The first one is the experimental mapping method and, the second, using light scattering simulations to complement the experimental results. As part of the first method, the scattering morphology of spheroid particles stuck to the substrate at different orientations was collected. It is then used as a standard reference for a "Scattering Morphology Resolved" - TIRM experiment (SMR – TIRM) to help create the map. The scattering morphology map will be used as a guide to validate the unknown aspect ratio and orientation of a particle at each frame in an SMR – TIRM experiment. In the second method, a computer simulation was used to understand the trend of scattered light morphology from particles. For this, we established a collaboration with Dr. Thomas Wriedt[160] at the University of Bremen. His research group has developed a light scattering model for total internal reflection microscopy using the T-Matrix method. Applying this code on an ellipsoid particle can help me to predict scattered light morphology from ellipsoidal particles. In section 5.4, I will explain the techniques to collect these data.

5.4 Experimental and collecting data techniques

In the experimental part of the project, I followed several approaches. In the first part, I conducted conventional TIRM on the different types of spherical isotropic particles to calibrate and optimize the TIRM system, including designing accurate tools. The second part of the experiment was collecting data for SMR-TIRM system mapping. In this section, after preparing the ellipsoid particles with different aspect ratios, the particles were stuck on the substrate inside the system, and scattered light images at different orientations were collected.

5.4.1 TIRM Setup

The TIRM hardware setup (Fig. 5.1) includes three main parts. The first part is the mount (Fig. 5.4), which is a combination of equipment to create an evanescent wave and places to put the dispersion on it. The second part is an optical microscope to collect scattered light. The last part of the system is a software to convert the collected scattered lights by an optical microscope to images and videos. The mount includes a laser beam, a single-mode fiber optic, a collimator, a polarizer, prism, and base to put together the different parts of the system. The polarizing filter is used to let only light of specific polarizing transmits through it, and block the other polarizing. The optical microscope includes a stage, an objective, and a charged-coupled device (CCD) camera. Also, we use Cellsens software to convert the data from the optical microscope to the images and videos. The detailed technical features of the mentioned parts are explained in **Table 5.1**.

Table 5.1. The TIRM hardware part specification details.

Name of the Part	Description	Manufacturer
Mount		
Laser	PLM-633.0-PMF model – 633 nm laser Power output > 40mW	NECSEL Co.
Fiber Optic	1m long fiber optic with FC/PC	NECSEL Co.
Collimator	CFC-8X-A - f = 7.5 mm, ARC: 350-700	THORLABS Co.
Polarizing filter	Rotating Linear Polarizer Module, 500 -	THORLABS Co.
Prism	25mm(W) × 50mm(L) Facilitated by 75° & 68 ° edges	
Base	Made of Aluminum	In-house made
Optical Microscope		
Optical Microscope	Olympus BX51WI microscope	Olympus Co.
Optical Objective	LUCPLFLN40X Objective, NA = 0.6	Olympus Co.
CCD Camera	Max 115.1 frames/Sec with binning	Hamamatsu Inc.
Software		
Cellsens Software		Olympus Co.

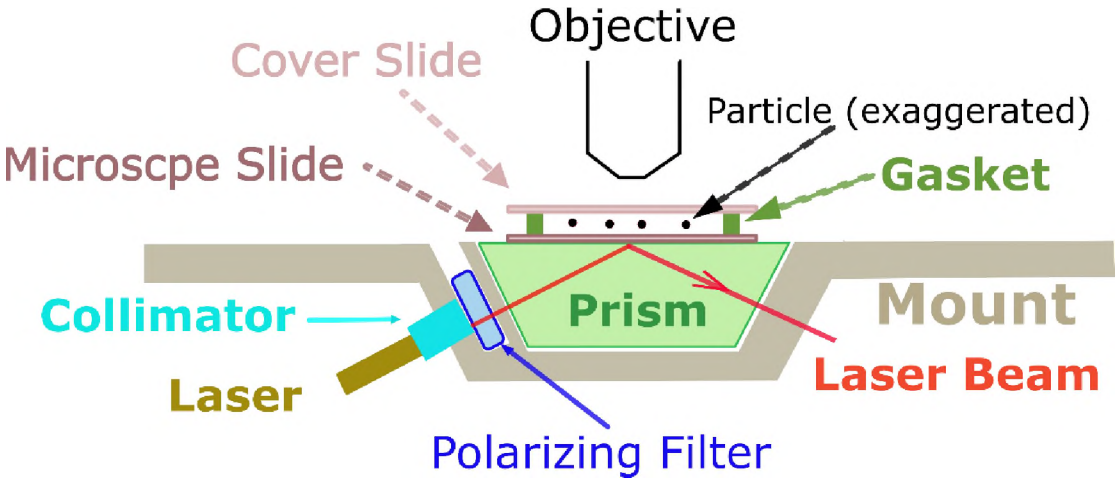

Figure 5.4. Schematic figure of the mount.

5.4.2 TIRM on Isotropic Spherical Particles

Total Internal Reflection microscopy was conducted with nominally 6 μm polystyrene (PS) and 3 μm silica (Si) spherical particles. Both the PS (Molecular Probes Inc.) and Si (Sigma-Aldrich Inc.) particles were negatively charged. Collecting data in TIRM takes place in several steps. The first step is preparing samples. The second step is cleaning the prism and slides. The third step is putting the prism on the mount and connect the laser. The final steps are focused on adjusting the microscope, laser software, Cellsens software, and capturing videos or images.

Different types of experiments with different dispersants can be conducted in the TIRM device. Two main parameters should be considered in the sample preparation step. These are electrolyte concentration and dispersion concentration. In the TIRM experiment, it is crucial to prevent scattered light interference among particles while applying a laser beam. For this purpose, I kept the particle concentration low. After preparing samples, it would be good to check particle concentration on top of a regular slide before using them in the TIRM system. The particles were diluted and dispersed in a 1 mM NaCl-water solution. The sample was shaken for about thirty seconds to disperse the particles. For cleaning the prism and slides, I used Kimwipe and acetone

(HPLC grade, AlfaAecer Co.) several times until any oil has been removed from the surface. I repeated the same process with ethanol (200 Proof anhydrous, Decon Laboratories Co.). Finally, I rinsed them with water and then dried the prism quickly with the aero duster (MS-222N, Miller Stephenson Co.) to remove fibers that may exist on the surface. The optical faces of the prism should look pristine. After cleaning, I put the prism into the chamber of the plasma cleaner and cleaned it for 2 minutes. After placing the prism in the mount, the dispersion was injected into the TIRM cell, which includes a microscope slide, surrounding gasket, and a microscope cover glass (Fisher Scientific - 24×50-2 mm) on top of the prism (Fig. 5.4). Microscope immersion oil (Thermo Scientific Resolved) was used to optically couple the prism and the microscope slide. Grease (Dow Corning vacuum grease) was used between the gasket and the microscope slide and the cover slide to prevent leakage. The particles were monitored using an Olympus BX51WI upright optical microscope and Olympus LUCPLFLN40X objective. A laser beam (λ= 638 nm) at 68° or 75° angle of incidence was used to create an evanescent wave. The critical angle for the glass prism and water is 57.4°. After putting the mount on the microscope stage and injecting the dispersion, at least thirty minutes is necessary for the particles to settle. Raman Box Control Panel software was used to adjust laser power as well as turn on the laser. The scattered light from the particles was captured at 24-frame per second rate for 25 minutes. This process generated 36000 frames, which were collected by a charged coupled device (CCD) camera (Hamamatsu Inc.). The images were transferred into CellSens software (Olympus Co.) and saved in a big tiff (btiff) format. The scattered light intensity value at each frame was measured by an in-house made MATLAB code (APPENDIX 5.1). In this code, after loading the video in btiff format, the pick point of the scattered light intensity value was found as a reference to track the particle. The next step in the code

is calculating the background of the frame. For this purpose, the average of the twenty pixels at four directions from the pick pints was calculated as the background of each individual frame. The intensity value at each frame was calculated by the integration of the pixel values at each frame minus background intensity of the same frame. The raw captured scattered light intensity from each experiment was initially converted to an observation histogram and then to a particle height distribution (Figs. 5.2A & B). Equation 5.6 was used to convert the number of observation histogram data to potential energy profile (Fig. 5.2C).

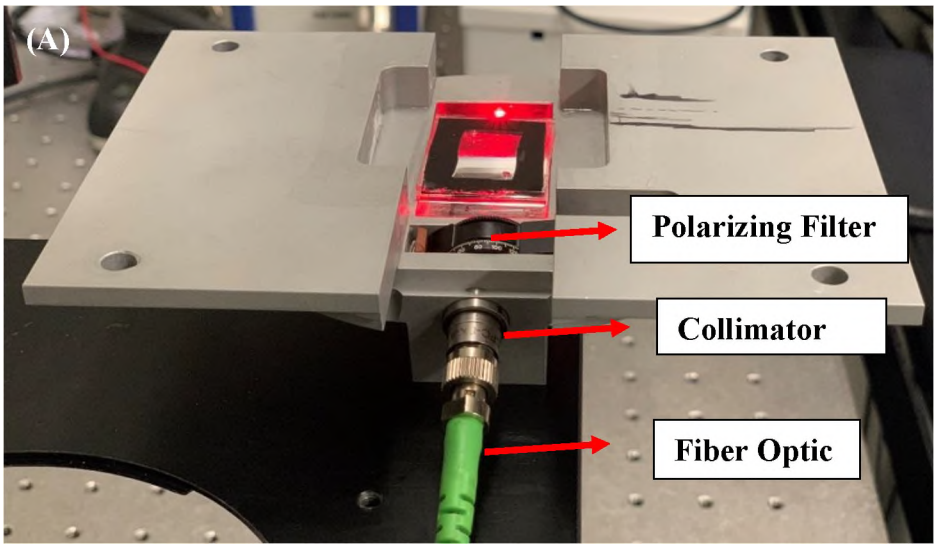

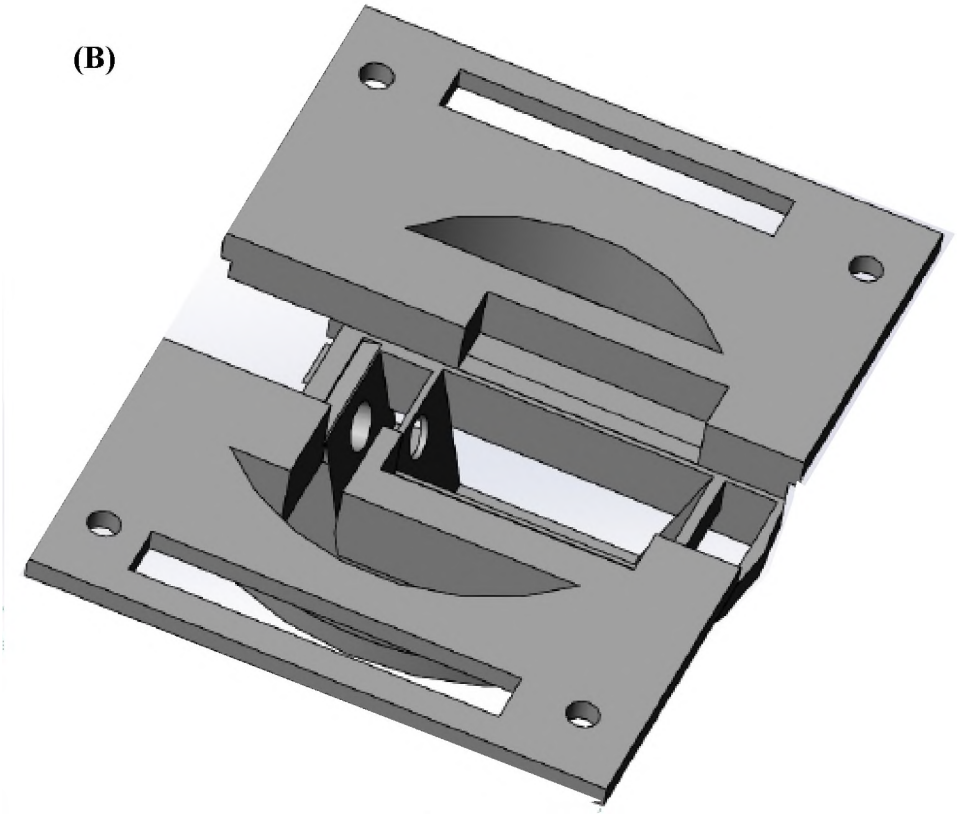

Figure 5.5. (A) In-house made mount with its attachments. (B) Schematic drawing of the mount.

5.4.3 Preparing of polystyrene ellipsoids

I chose ellipsoid polystyrene particles as a model system for this study. In the SMR – TIRM experiments, the various aspect ratio of ellipsoid particles was used. Ellipsoids were synthesized with the monoaxial stretching technique. In this technique, spherical polystyrene particles are dispersed in a low concentration polyvinyl alcohol (PVA) solution. I added 13.358 g PVA in 534.38 g of pure water and began mixing at 400 rpm on the magnetic stirrer. To prevent the PVA from clumping, I added it slowly. I left the solution to mix for 24 hours; 12 hours at room temperature and 12 hours at 50° C. After filtering the PVA/water solution, I added approximately 1 gram of 5 μm polystyrene suspension to the glass bottle and shook it gently to mix and avoid bubbles. The solution was casted to create a PVA/polystyrene film. Then I waited for the water to evaporate. It caused only PVA and the polystyrene embedded in the film to be left. After peeling the film from the surface, the dried film was cut into 7x7 cm squares of PVA films. Next, the small film pieces were tightly sandwiched between two metal holders in a mono-axial starching apparatus and heated to 145° C. During the stretching process, the film is stretched in a single direction to reach the desired aspect ratio. The stretched length depends on the thickness of the film, temperature, and heating time. Next, the stretched film was dissolved in IPA/water stirring solution. The ratio of IPA to water is 3 to 7, and the stirring speed is 400 rpm. I repeated the similar washing process with IPA/water three times and with pure water six more times. After the washing process, the ellipsoids were ready to be used.

Ellipsoids prepared in this way typically maintain a strong bound surface charge. For example, a sulfate *poly*styrene particle will still have sulfate groups exposed after stretching. This surface charge is vital because a strong repulsion force from the surface is necessary to maintain the particles being stable during the experiments. **Figure 5.6**

shows the stretching process, and **Figure 5.7** shows a sample of a prepared ellipsoid particle in our lab.

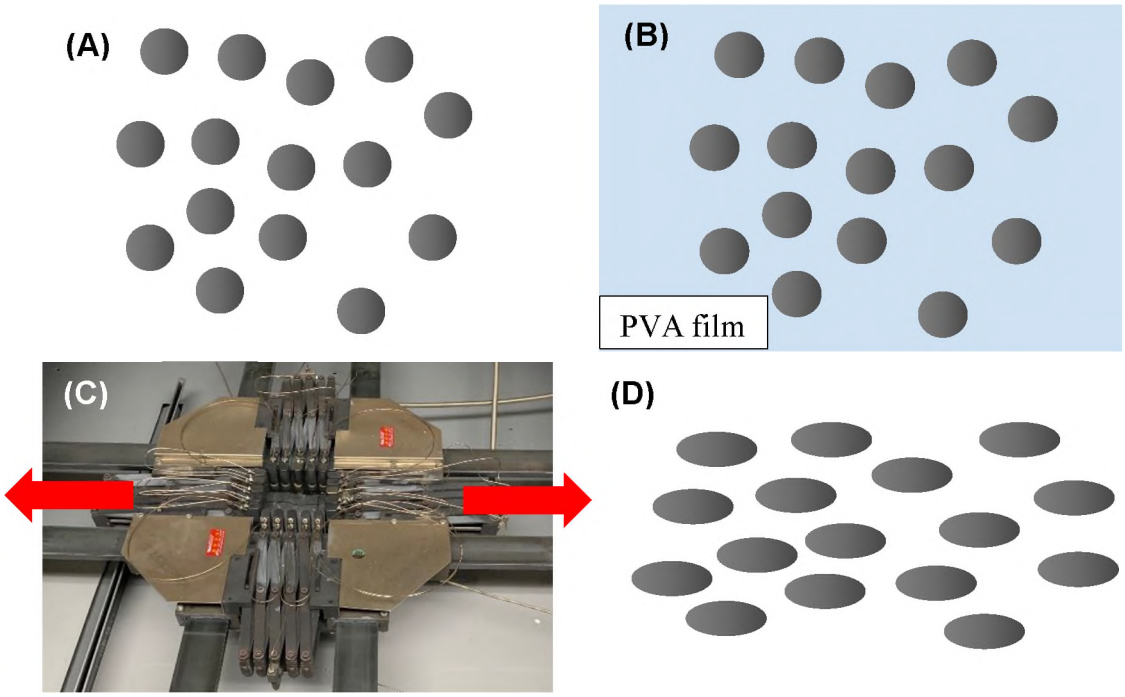

Figure 5.6. (A) Spherical Polystyrene, (B) Particles mixed in PVA/water solution, (C) Mono-axial stretching apparatus to stretch PVA films, (D) Films dissolved/washed in isopropyl alcohol/water solution.

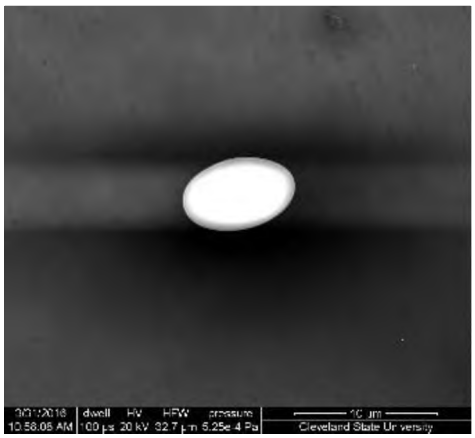

Figure 5.7. Scanning electronic micrographs (SEM) image of an ellipsoid particle fabricated in our lab.

5.4.4 Map the evanescent wave scattering from spheroids at known height and orientation.

I performed SMR – TIRM measurements on a group of horizontally stuck (h = 0nm) ellipsoid particles at different ϕ orientations to prepare pixel value maps of those particles (Fig. 5.8). A comprehensive map of scattering morphology from particles of known aspect ratio and orientation of particles will be measured. The scattering morphology map will be used as a guide to validate the position and orientation of a particle at each time-step in an SMR – TIRM experiment. **Figure 5.8** shows the profound difference in scattered light morphology between a sphere and ellipsoidal particle. Before starting the mapping experiment, I have to make sure that the ellipsoid dispersion concentration is adequate to prevent interference of the scattered light from the neighboring particles. Nominally 5 μm sulfate latex polystyrene beads were used. These particles were negatively charged, thereby being repelled at most conditions from the negatively charged substrate. Deposition was encouraged by increasing the electrolyte concentration to screen the electric double-layer repulsion force. During sample preparation, after washing the stretched ellipsoid particles, I dispersed them in a 10 mM NaCl solution. I sonicated the dispersion for thirty minutes. It helps to separate potential agglomerated samples before injecting the sample in the cleaned TIRM cell. Following injection, particles require approximately 30 minutes to settle to the bottom boundary.

CellSens software was used to collect images and metadata, including the type of the image, acquisition time, etc. The acquisition time for images was 10 ms. Before taking images, care was taken to minimize and eliminate interference from scattered light arising from neighboring particles. Images were collected with backlight, to characterize the known particle specification, such as aspect ratio, major length, and

particle orientation. Other images were collected without backlight at no-binning and 4-binning conditions. The data reported in this research for mapping were collected at 20 mW.

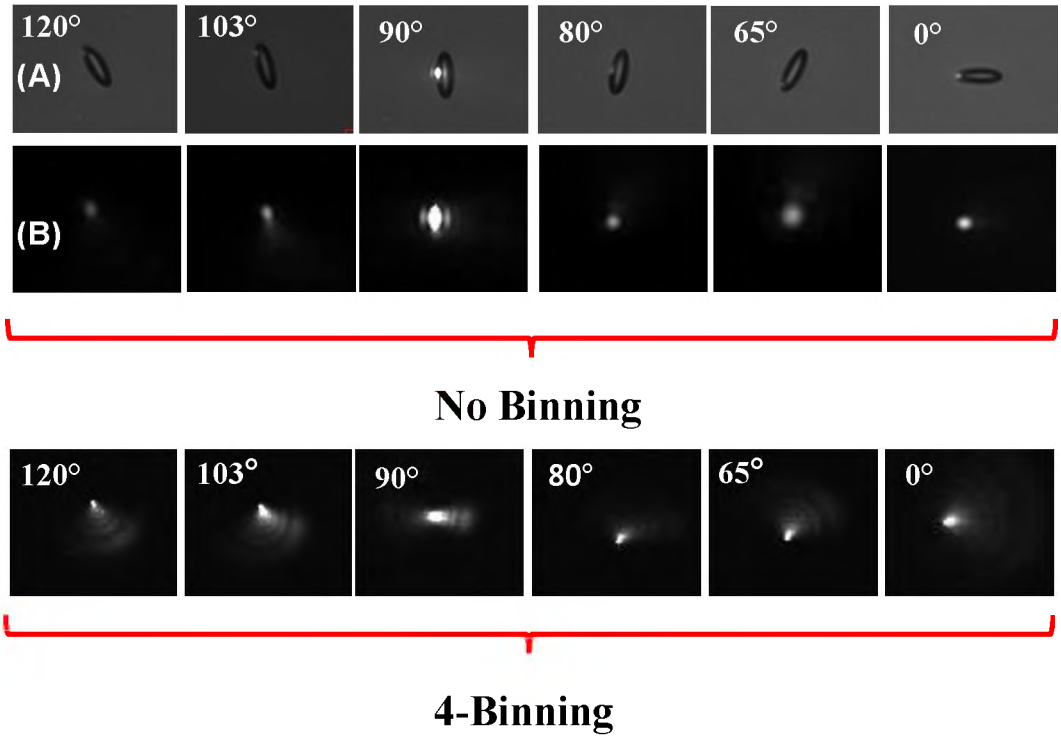

Figure 5.8. Scattered light from ellipsoidal particle stuck to the substrate at different orientations collected by CCD camera. The laser power is 20 mW. (A) Images with backlight. (B) Images without backlight at the no-binning condition. (C) Images without backlight at the 4-binning situation.

5.5 Results

5.5.1 Conventional TIRM on Spherical Isotropic Particle

To evaluate applying TIRM on a spherical isotropic system, two types of particles were used. Namely, a 6 μm PS spherical particle and a 3 μm silica spherical particle. I converted the scattered light intensity data collected by CCD camera to the number of observation histogram (Figs. 5.9A & C). The histogram data was converted to a potential energy profile (Figs. 5.9B & D) by Eq. 5.6. The particle is under the influence of gravitational force (Right side of the minimum point) and double-layer repulsion

force (left side of the minimum position), as shown in the potential energy profile. **Figure 5.10** show the potential energy profile for each of the two particles. Electrostatic double layer repulsion is the primary contributor to the left side of the curve. Given that each particle was suspended in 1 mM NaCl, these curves are similar for each measurement. However, the slope of the right side of the curve is primiarly dictated by the weight of each particle. Given that a 3 μm of silica particle is heavier than a 6 μm polystyrene particle, the slope of the PE profile on that portion of the surve is larger than the slope for the PE profile of the polystyrene particle.

One outcome of a TIRM experiment is the determination of particle and solution properties from the potential energy profile. I fit the potential energy profile with a nonlinear least square method to determine particle and solution properties. The calculated particle size and electrolyte solution based on the potential energy profile of the TIRM experiment (Figs. 5.9.B D) are summarized in **Table 1**. These results are in strong agreement with the expected values.

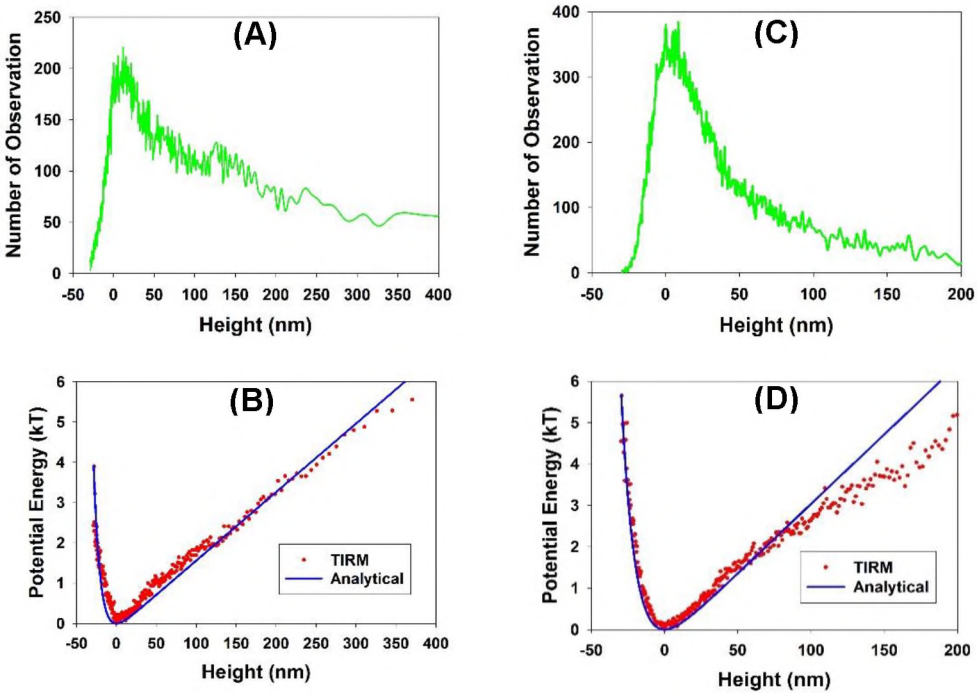

Figure 5.9. Experimental TIRM data for 6 μm PS particle in 1 mM sodium chloride electrolyte. (A) The number of observation histogram, (B) The potential energy profile calculated by TIRM (red circles) and potential energy profile calculated analytically (blue line). Experimental TIRM data for 3 μm Si particle in 1 mM sodium chloride electrolyte. (C) The number of observation histogram, (D) The potential energy profile calculated by TIRM (red circles) and potential energy profile calculated analytically (blue line). The height is the difference between the real height of the particle and the height of the particle in the most probable height (h-h(m)).

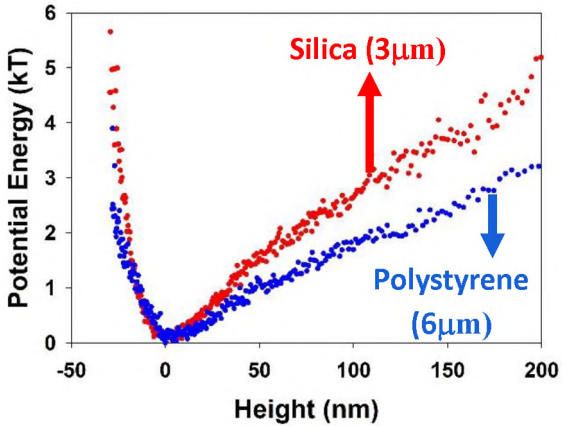

Figure 5.10. Combined potential energy profile for 6 μm PS, and 3 μm Si particles.

Table 5.2. TIRM experiment results to calculate particle and solution properties.

Particle	Actual Size (Company data)	Calculated Size (TIRM)	Electrolyte Conc. (Real)	Electrolyte Conc. (TIRM)
Polystyrene	5.8 μm	6.32	1 mM	1.38
Silica (3 μm)	3 μm	3.02	1 mM	1.35

5.5.2 Mapping Ellipsoid Particles in SMR-TIRM system

Our strategy to create a morphology map for the ellipsoid particle is based on the hypothesis that the morphology of scattered light from an anisotropic particle is a sensitive function of orientation, aspect ratio, and volume of the particle. Two approaches that I used in this process are the experimental mapping method and the simulation method. In the experimental technique, a comprehensive experimental map of scattered light from stuck ellipsoidal particles at different aspect ratios and orientations were collected. In addition, simulated scattering data from stuck ellipsoidal particles at various orientations, volumes, and aspect ratios were used to interpret and validate the experimental morphology of the ellipsoidal system. The method of collecting data is explained in the experimental and collecting data techniques section. I used two techniques to analyze data. The first method (ellipticity-direction method) applies to full-resolution images, while the second method (quadrant method) applies to binned images. The only simulation images that I used in this research to validate the experimental data were created at no-binning condition, so I applied only ellipticity-direction on the simulation data. However, based on the type of images, both methods were used to analyzing experimental data.

In the ellipticity-direction method (**Figure 5.11**), I analyzed the ellipticity and direction of the scattered light under TIRM. While a variety of analysis and fitting techniques were tested, I found the most reliable and robust results were obtained by

applying a 2D Gaussian function fit to the spatial distribution of the scattered light. In this technique, I used an open-source code developed by Gero Nootz[175] that was modified for our system by Dr. Sergio Dominguez Medina. Also, I added a function to the code to calculate the Gaussian parameters by using MATLAB tools, as well as calculating fitting error. The original code can be found in the Mathworks file exchange, and the modified version is available in APPENDIX 5.2. The code can find the position, orientation, and width of the two-dimensional Gaussian. After getting scattered light intensity data in the btif or Jpeg format, the code uses a non-linear least-squares optimization tool for finding the best-fitting curve on Gaussian function in X and Y axes separately (first part of the code). Also, the modified code is able to find a Gaussian fitting coefficient by a non-linear least-square tool of MATLAB and Levenberg-Marquardt algorithm (modified part o the code). In the first part of the code, I need to apply initial values for orientation and Gaussian width, and in the modified part, I need to use initial values for the Gaussian fitting coefficients. These values should be close to the final fitting results in order to fit to converge. Later, these fittings were used to calculate direction and aspect ratio of the scattered light (**Figure 5.12**). In the first part of the fitting process, the fitting RMSE parameter was calculated to evaluate the error. For the modified part, standard error of the coefficients, RMSE, R-square, and SSE of the Gaussian fitting function was calculated for each image.

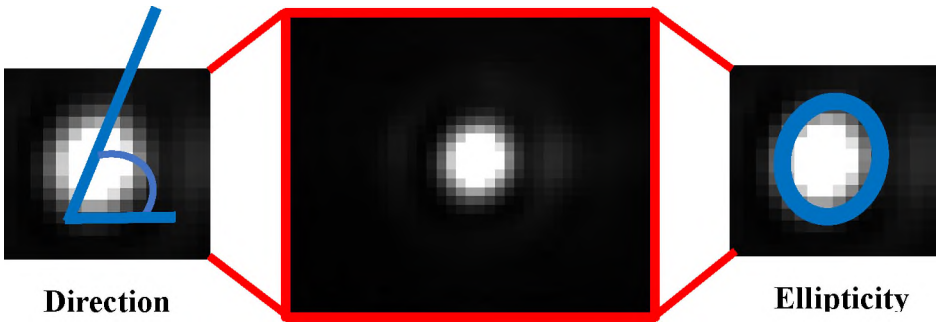

Figure 5.11. Schematic figure of Ellipticity-Direction method concept.

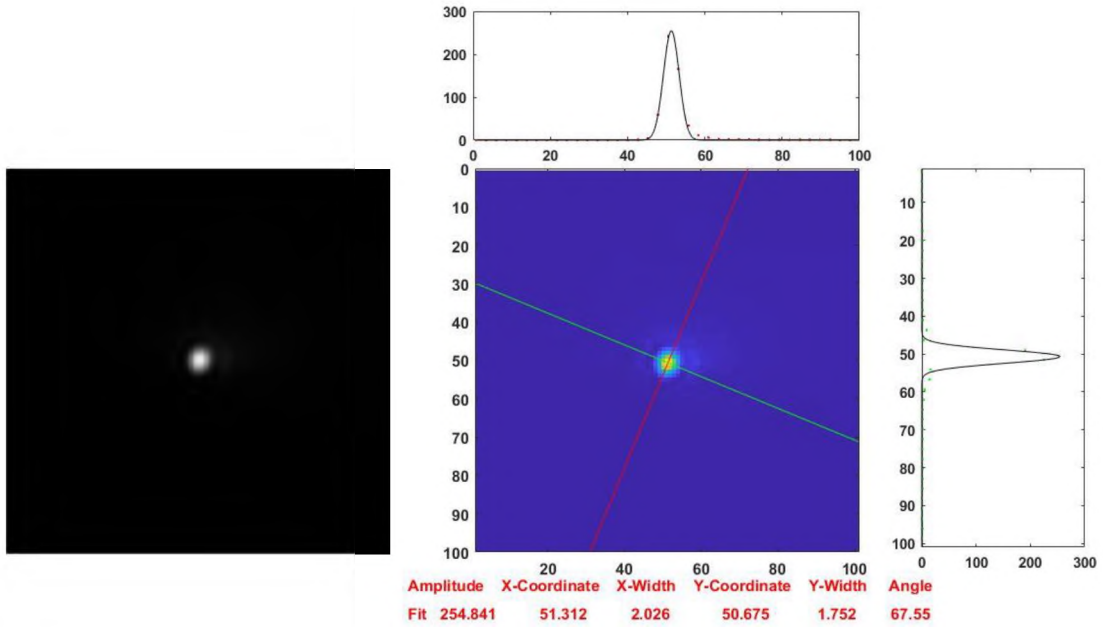

Figure 5.12. The Gaussian fitting technique to deduce the direction and ellipticity of the scattered light. The aspect ratio is calculated by dividing X-Width by Y-Width. This method is applicable to no-binning images.

The quadrant method (**Figure 5.13**) is suitable for 4-binning images. In this method, the center of the scattered light image, which is the center of the maximum intensity value scattered from the particle, is set as the center of a quadrant system. Integrated intensity is obtained by first determining the background intensity and then summing the value of all pixels within twenty pixels far from the center. In the code, there is a definition for pixel limit value based on the calculated background. It is used to distinguish the region of interest or pixels occupying the intensity values belonging to the particle. This pixel limit is 1.2 times of the background. Based on the pixel limit value, the code screens the pixels to find the right pixels occupied by scattered light at each quadrant. Later, the integration of the intensity at every four quadrants minus background is calculated. The distribution of the intensity at each quadrant can be used to interpret the orientation of the particle.

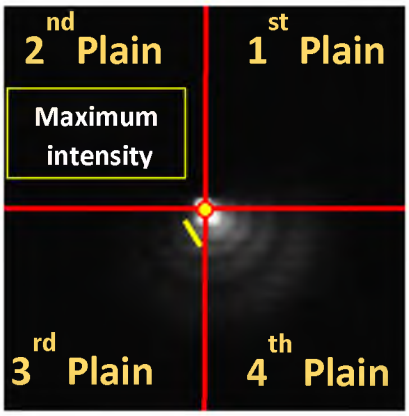

Figure 5.13. The quadrant method description. The scattered light intensity at each quadrant plain was calculated.

In all of the results in this part, I defined the rotation of the particle while it is stuck to the substrate (in X-Y quadrant system – azimuthal angle) as φ. The detail of the φ angle definition in the result section is schematically shown in **figure 5.14**. The aspect ratio is calculated by $\frac{a}{b}$ ratio.

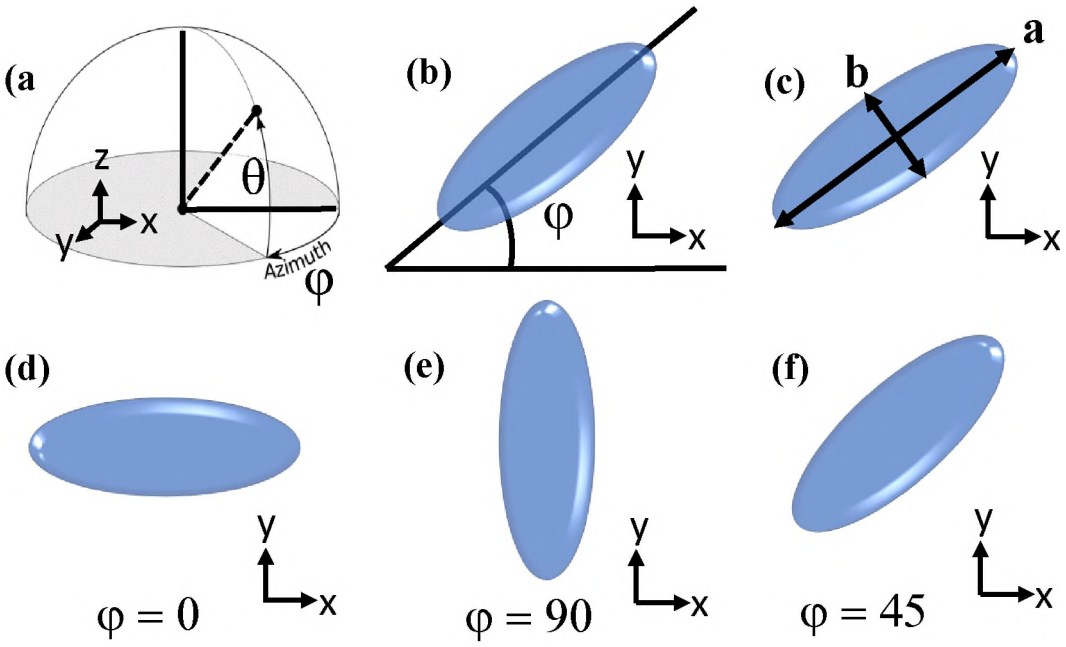

Figure 5.14. Schematic detail of φ angle definition.

The stretching process used to fabricate ellipsoidal particles was earlier described. I used 5 μm spherical sulfate latex polystyrene particles (Invitrogen Inc., 4% w/v). The

product's certification specification shows the mean as equal to 4.9 μm, its standard deviation 0.29 μm, and the polydispersity of the product in the range of 5.0 ± 0.5 μm. I used the stretched particles in two aspect ratio (AR) groups. Low aspect ratio particles (LAR), which their AR was in the range of 1.35-1.85 μm, their average was 1.6 μm, and their standard deviation was 0.1008 μm. High aspect ratio particles (HAR), which their AR was in the range of 2.6-3.2 μm, their average was 2.8 μm, and their standard deviation was 0.1424 μm. In the simulation, the AR that I chose was similar to the average size of AR of LAR and HAR.

In applying the ellipticity-direction method on the experimental data, the specification of the scattered light (scattered light direction or AR) vs. different particle features (particle orientation and AR) was plotted. **Figure 5.15** shows the effect of the ellipsoid particle orientation on scattered light direction. The results predict that increasing azimuthal angle of the particle (clockwise – check **figure 5.14** for particle orientation definition) leads to increasing scattered light direction approximately linear. The simulation results for the particles at the same AR range almost validate the experimental results for both LAR and HAR. Dr. Sergio Dominguez Medina prepared these simulated images with the T-matrix method in collaboration by Dr. Wriedt. The changing directionality of the scattered light by changing the orientation of the particle clearly depicts how the shape of the particle can impact the scatted light. As the shape and curvature of the particle are not uniform as a sphere, any changes at the incident angle of the evanescent can create different internal reflection pattern inside the particle. As a consequence of this phenomenon, we can see the directionality change in this system. It can be seen in the graphs that at each particle orientation, the directionality of the scattered light is not exactly unique, and they are not precisely matched with the simulated results. Many potential parameters may affect this deviation in the

experimental results. One interesting finding that can be seen in **figure 5.15B** is that the experimental results in HAR don't cover all of the particle orientations; i.e. there is a blind region outside the 60°-120° range. When evanescent wave, which is not an oscillating wave and has limited travel diffusion, hits a particle, the input energy can be divided into several parts. One part of the energy absorbs to the particle, the other part is internally reflected inside the particle, and the remaining energy is scattered from the particle. It seems that a lower curvature (HAR particles) at a low or high azimuthal angle can cause an increasing number of internal reflection. The rising number of internal reflection causes energy loss and consequently decreases the scattered light intensity power. The reduction of scattered intensity makes tracking of the scattered light hard or impossible.

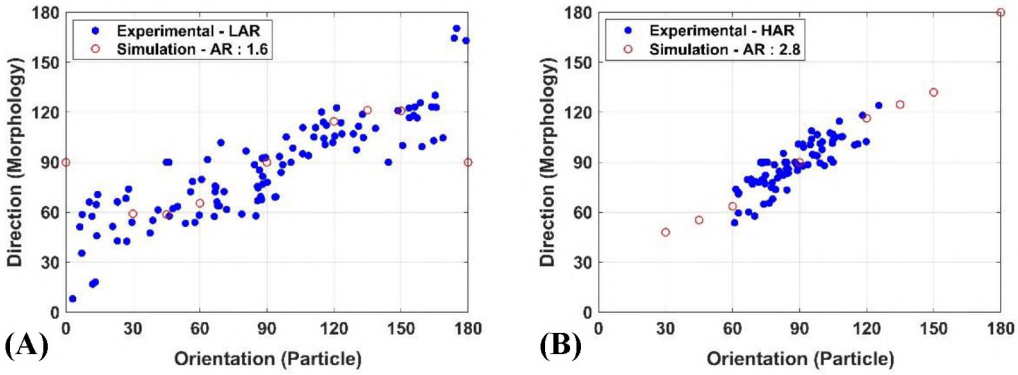

Figure 5.15. Effect of the ellipsoidal particle orientations on the scattered light intensity direction. The open circles on each graph represent simulation results calculated by Dr. Sergio Dominguez Medina with the T-matrix method. The solid circles are experimental results. (A) LAR. (B) HAR.

Also, the simulation results (**figure 5.16**) show that the aspect ratio of the particle doesn't impact the directionality of the scattered light. The simulation results at three different aspect ratios (1.6, 2, and 2.8) have similarly scattered light directionality. Also,

the experimental results follow are almost match to the simulated data and follow the same trend.

In **figure 5.17**, the effect of the ellipsoid particle orientation on the scattered light AR is shown. These results demonstrate the impact of the shape of the particle on the morphology of the scattered light. It can be seen that rotation of the ellipsoid particle can change the scattered light shape (ellipticity) or morphology, which is recognizable. The features such as particle curvature and the internal reflection of the evanescent wave affect the shape of the output wave. The simulation results in **figure 5.17B** show that despite the scattered light direction, the scattered light AR is under the influence of the particle AR. Increasing particle AR can exaggerate the impact of particle orientation on the scattered light AR. But, there is weak compatibility between the simulation and the experimental results.

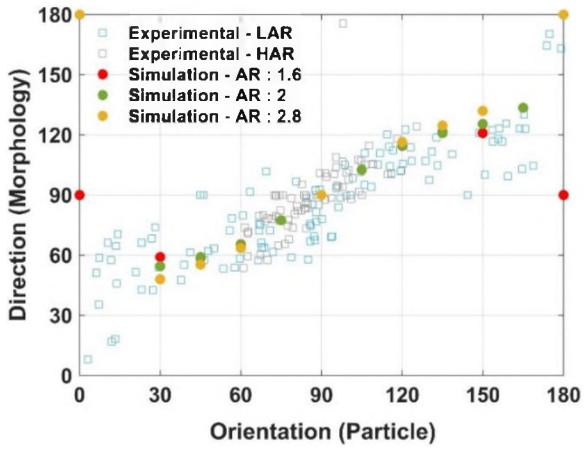

Figure 5.16. Effect of the orientation of the ellipsoidal particles on the scattered light intensity direction. The solid circles are simulation data at different ARs. The squares are the experimental results for both HAR & LAR.

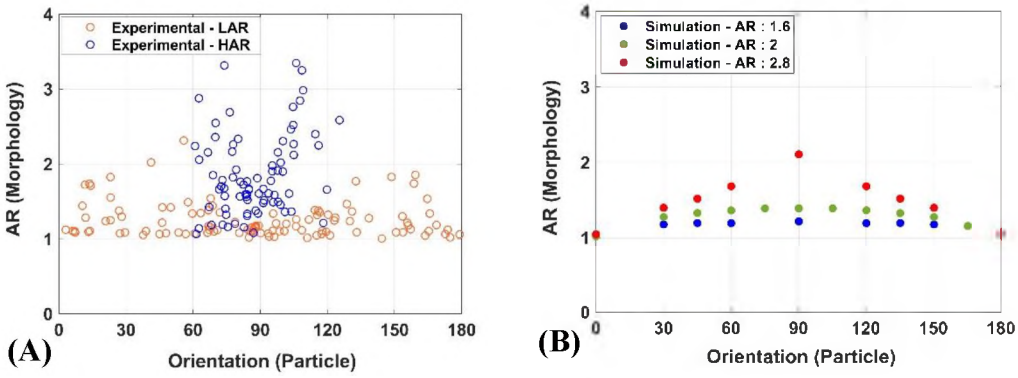

Figure 5.17. Effect of the ellipsoidal particle orientations on the scattered light AR. (A) Experimental results based on two individual groups (LAR & HAR). (B) Simulation results for three different AR.

Although the experimental results discussed herein have many similar features to simulated data, there are still important quantitative differences. The origin of these differences has recently been identified, including (1) inexact characterization of ellipsoidal particles (i.e. polydispersity of the stretched spherical particles or polydispersity in the stretch), (2) error associated with the Gaussian fitting method, (3) deviation of stuck particles from the long-axis parallel condition with respect to the substrate (theta problem - sticking problem), and (4) the error in calculating particle features in bright field.

At non-parallel condition, it is important to understand better the correlation of the ellipsoid major length polydispersity to potential sticking problem. For this reason, I compared the particle size polydispersity of the spherical particles to the major length polydispersity of the ellipsoidal particles. In a precise particle stretching process, we should expect similar major length polydispersity in ellipsoidal particles and size polydispersity in spherical particles. However, **figure 5.18** shows that the polydispersity of the ellipsoidal particle major length is bigger than the polydispersity of the spherical particle size at both LAR and HAR. Two reasons may cause this phenomenon. One reason may come from an inappropriate stretching process that

deviates the particle from ellipse shape. The latter problem can cause an error in calculating particle AR as well as error in the scattered light morphology. Another reason for the unmatched polydispersity is the deviation of the ellipsoid particle from the parallel sticking to the substrate or theta deviation.

To evaluate the effect of theta deviation, I used the simulated images created by Dr. Sergio Dominguez Medina. **Figure 5.20** shows the impact of the theta deviation on the correlation between particle features and the scattered light properties. At 10-degree polar angle deviates, the scattered light directionality of simulated images can have up to 2% deviation in the range of the scattered light directionality distribution. Also, in the same situation, the scattered light AR can have up to 20% deviation in the range of scattered light AR distribution. Thus, the polar angle deviation or any error from appropriate sticking of the particle to the substrate had a significant effect on the morphology aspect ratio results (and a relatively small impact on the directionality results). According to the last analysis, the theta deviation may have a significant contribution to the deviation of the experimental results from simulation results in **figure 5.20A**.

Another potential error is Gaussian fitting. In the Gaussian fitting, we expect to calculate AR of the scattered light. But in some of the images, the scattered light deviates from ellipses shape, and a tail appears. This tail may impact the accuracy of ellipticity calculations. In the simulation data, there isn't such a tail. It seems this type of tail in some of the experimental data is the consequence of the collecting light by the microscope system. To understand whether this tail impacts the results, we conducted a Gaussian fitting error calculation. In this analysis, several error factors were calculated in the modified 2D-Gaussian code. We figured out that after fitting, the data

that have R-square bigger than 0.99 can provide us data that are more compatible with experimental data (**Figure 5.19**).

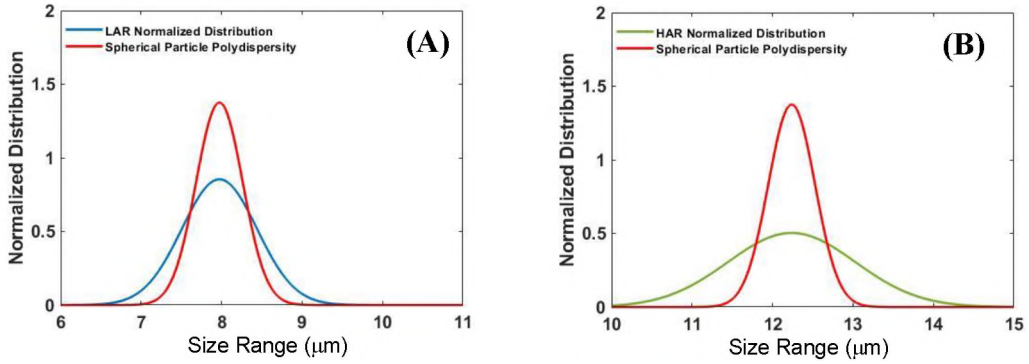

Figure 5.18. Particle major length polydispersity normalized distribution. The blue and green lines are a normal distribution for the ellipsoid particle major length distribution, and the red line is a normal distribution for the size of spherical particles I used to create ellipsoid particles. (A) LAR ellipsoid particle polydispersity diagram. (B) HAR ellipsoid particle polydispersity diagram.

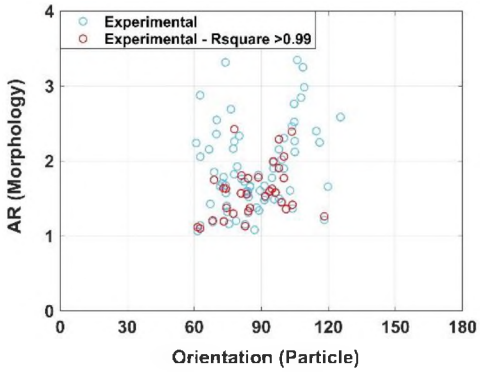

Figure 5.19. Error analysis of the experimental data. The red circles represent fitting data that their Gaussian fitting has an R-square parameter bigger than 0.99.

In applying the quadrant method on the experimental data in the 4-binning condition, I plotted the specification of the scattered light direction versus particle orientation. **Figure 5.21A** shows the integration of the intensity at the 1st quadrant versus the particle orientation. The fitting chart shows a sin shape correlation between the integration of the scattered light in the 1st quadrant. **Figure 5.21.B** shows the scattered light intensity integration in the 4th quadrant. In this graph, there is a reverse

sin correlation between intensity integration and particle orientation. These graphs tell us that the morphology of the underestimated images can provide us a new set of information. This information can help us to predict the orientational position of the ellipsoidal particles. In this case, there is inaccuracy in the results. The source of errors and inaccuracy may be similar to the parameters which I explained in the ellipticity-direction method part. In APPENDIX 5.3, the in-house made MATLAB code to apply the quadrant method on 4-binning images is available.

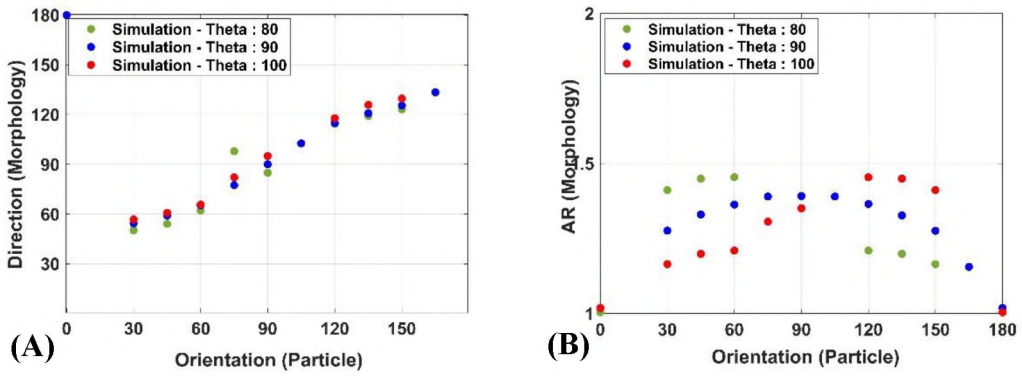

Figure 5.20. Simulation results for the effect of the polar orientation on the scattered light morphology. Dr. Sergio Dominguez Medina generates raw simulation data. The results are for sticking particles parallel to the substrate (polar angle equal to 90-degree) as well as ±10-degree polar angle deviation (80-degree & 100-degree).

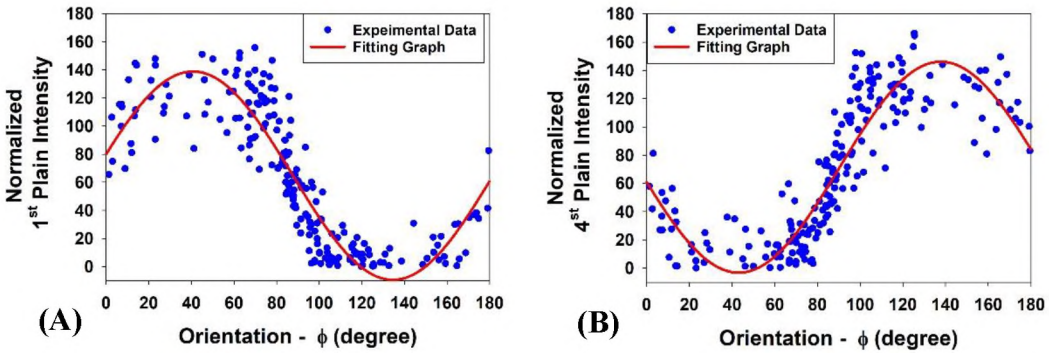

Figure 5.21. Distribution of the scattered light intensity at different ellipsoid particle orientations. The images are captured in a 4-binning condition. The solid red line is a fitting graph. (A) The scattered light intensity integration in the 1st quadrant. (B) The scattered light intensity integration in the 4th quadrant.

Each of the analyzing techniques has its own advantageous and disadvantageous. In the ellipticity-direction method, which uses Gaussian fitting to evaluate the data, both the direction and shape of the scattered light were assessed. This condition can give us more morphology information as compared to the quadrant method, which only evaluates the directionality of the scattered light. On the other hand, if the particle fluctuates in a weak evanescent field for any reason, tracking the scattered light in the no-binning condition is difficult or impossible. However, at the same evanescent field, it is possible to track the same particle in a 4-binning condition. It means that in such situations applying an ellipticity-direction method, which is applicable to images at no-binning condition, is not possible, but we can conduct a quadrant method.

5.6 Conclusion

In this chapter, I applied the SMR-TIRM device to ellipsoidal particles. The hypothesis for this work was that both the integrated intensity and morphology of evanescent light scattered depends on shape and orientation. The hypothesis was tested by mapping scattered light morphology for ellipsoids of different shape and orientation. Experimental mapping data was compared with simulated data. I designed and manufactured a TIRM system to help us conduct these experiments. After collecting data, two methods called ellipticity-direction and quadrant methods were used to analyze the morphology of the scattered light data from ellipsoid particles. The results show that particle orientation and aspect ratio correlate the scattered light AR and scattered light directionality. This information can help us to use these correlations as a map to unveil the scattered light morphology meaning at the different conditions to understand the features and positions of the particle an SMR-TIRM system.

CHAPTER VI
CONCLUSIONS AND RECOMMENDATIONS

6.1 CONCLUSIONS

In this thesis, the dynamics of anisotropic particles near a wall, and the possibility of applying TIRM to anisotropic particles were investigated. I used Brownian dynamics simulations to predict the dynamic behavior of a Janus particle with a matched density and mismatched density cap near a wall. I helped to develop a fabrication and characterization technique for metal-coated Janus particles. I developed a hypothesis regarding the response of an ellipsoid particle to an evanescent wave and a methodology to interpret the scattered light morphology. This hypothesis was used to conduct evanescent wave mapping on ellipsoid particles. Comprehensive knowledge of interpreting scattered light morphology is essential to use it in TIRM process and tracking particle position as well as calculating potential energy profile.

To determine the impact of the matching density cap in the dynamics of a Janus particle, I applied Brownian dynamics simulation on a Janus particle in the range of 1 μm to 6 μm. The particle had hemispheres with a difference in zeta potential. Particle rotation was influenced by electrostatic double-layer repulsion force between the particle and the substrate. Tracking the fluctuation of the particle showed that the hemisphere with larger zeta potential can get closer to the substrate. I calculated the 3D

potential energy landscape of the particle following simulation of the position and rotation of the particle for the first time. This part of the thesis provided evidence that Brownian dynamics simulation can be used as a tool to probe TIRM for anisotropic particles.

To identify the effect of the cap weight on the dynamics of the Janus particles near a wall, I expanded the Brownian dynamics simulation to particles with caps of density not matching that of the native particle. The output of the simulation showed that the degree of gravitational torque effect on the rotation of the Janus particle depended on the size of the particle and coating thickness. At small coating thicknesses (> 5 nm) and small particle diameters (> 1 μm), the gravitational torque was negligible. Increasing particle size and coating thickness caused quenching of the rotation of the particle. The potential energy landscape, which was calculated according to the particle observation histogram, showed that Janus particles of typical size and coating thickness would sample only a limited number of orientation states.

I used physical vapor deposition to synthesize Janus particle with a cap of platinum and gold. The technique I used to fabricate was glancing angle deposition. I presented an experimental and image processing procedure to measure the local cap thickness of Janus particles in the micrometer scale. The results showed that cap thickness strongly varies over the cap, which is information necessary for understanding the dynamics of these types of Janus particles.

Finally, I used the an ellipsoid as a model particle for benchmarking SMR-TIRM. In summary, the integrated scattered light intensity of an ellipsoidal particle depended on the height, azimuthal angle, and polar angle, yet the morphology depended on the azimuthal and polar angles. A potential energy landscape of an ellipsoidal

particle will depend on the height and polar orientation. Thus, the azimuthal angle doesn't impact the potential energy landscape and would not need to be explicitly considered in a landscape calculation. The landscape will be generated by combining each individual potential energy profiles at each polar angle for an ellipsoid particle (**Figure 6.1**).

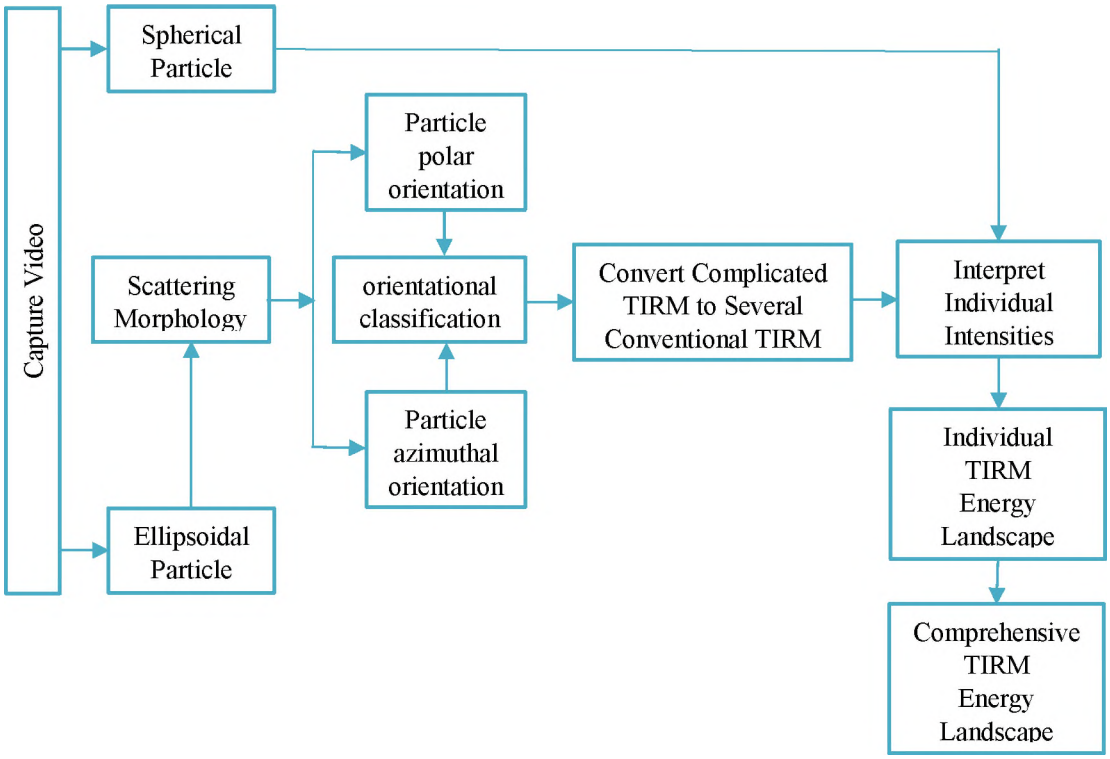

Figure 6.1. In this figure, you can see the proposed algorithm to calculate potential energy landscape for an ellipsoid particle.

6.2 RECOMMENDATIONS

In the mapping process of higher aspect ratio ellipsoidal particles, there is a blind region. For the mapping process and the SMR-TIRM methodology, scanning the images and the videos at 360° could increase the accuracy of the measurement. For this purpose, designing a new instrument to increase the scanning capacity in the azimuthal angle could be useful.

It is necessary to add data at polar angles beyond 90° to create a comprehensive morphology map. To accomplish this, designing new sets of experiments is essential. Applying an external AC electric field can cause standing the ellipsoid particle. Later, using an external DC electric field can cause sticking the particle to the substrate. In this condition, the ellipsoid particle stick to the substrate at a polar angle different than 90°. This polar angle is possible to be measured by the projection of the ellipsoid particle parallel to the substrate. Applying geometrical methods helps to calculate the polar angle of particle.

Adding coating on the particle can quench the rotation of the particle. On the other hand, it is possible to convert the system to an active system by applying an appropriate cap such as platinum as a catalyst inside a proper solution. It would be an exciting project to evaluate the effect of the different parameters such as coating thickness and particle size on the fluctuation and propulsion of this active particle near a wall.

REFERENCES

(1) Prieve, D. C. *Physical Chemistry of Colloids & Surfaces*; Carnegie Mellon University, 2014.

(2) Graham, T. X. Liquid Diffusion Applied to Analysis. *Philos. Trans. R. Soc. London* **1861**, *151*, 183–224.

(3) Lenis, J.; Razavi, S.; Cao, K. D.; Lin, B.; Lee, K. Y. C.; Tu, R. S.; Kretzschmar, I. Mechanical Stability of Polystyrene and Janus Particle Monolayers at the Air/Water Interface. *J. Am. Chem. Soc.* **2015**, *137* (49), 15370–15373.

(4) Wang, Y.; Wang, Y.; Zheng, X.; Yi, G.; Sacanna, S.; Pine, D. J.; Weck, M. Three-Dimensional Lock and Key Colloids. *J. Am. Chem. Soc.* **2014**, *136* (19), 6866–6869.

(5) Gangwal, S.; Cayre, O. J.; Bazant, M. Z.; Velev, O. D. Induced-Charge Electrophoresis of Metallodielectric Particles. *Phys. Rev. Lett.* **2008**, *100* (5), 1–4.

(6) Tasci, T. O.; Herson, P. S.; Neeves, K. B.; Marr, D. W. M. Surface-Enabled Propulsion and Control of Colloidal Microwheels. *Nat. Commun.* **2016**, *7*, 1–6.

(7) Leon Morales, C. F.; Strathmann, M.; Flemming, H. C. Influence of Biofilms on the Movement of Colloids in Porous Media. Implications for Colloid Facilitated Transport in Subsurface Environments. *Water Res.* **2007**, *41* (10), 2059–2068.

(8) Prieve, D. C.; Sides, P. J.; Wirth, C. L. 2-D Assembly of Colloidal Particles on a Planar Electrode. *Curr. Opin. Colloid Interface Sci.* **2010**, *15* (3), 160–174.

(9) Wirth, C. L.; Rock, R. M.; Sides, P. J.; Prieve, D. C. Single and Pairwise Motion of Particles near an Ideally Polarizable Electrode. *Langmuir* **2011**, *27* (16), 9781–9791.

(10) Giersig, M.; Mulvaney, P. Preparation of Ordered Colloid Monolayers by Electrophoretic Deposition. *Langmuir* **1993**, *9* (12), 3408–3413.

(11) Rogers, S. A.; Lisicki, M.; Cichocki, B.; Dhont, J. K. G.; Lang, P. R. Rotational Diffusion of Spherical Colloids Close to a Wall. *Phys. Rev. Lett.* **2012**, *109* (9), 1–5.

(12) Liu, Q.; Prosperetti, A. Wall Effects on a Rotating Sphere. *J. Fluid Mech.* **2010**, *657* (21), 1–21.

(13) Bevan, M. A.; Prieve, D. C. Forces and Hydrodynamic Interactions between Polystyrene Surfaces with Adsorbed PEO-PPO-PEO. *Langmuir* **2000**, *16* (24), 9274–9261.

(14) Magazzù, A.; Callegari, A.; Staforelli, J. P.; Gambassi, A.; Dietrich, S.; Volpe, G. Controlling the Dynamics of Colloidal Particles by Critical Casimir Forces. **2018**, 1–11.

(15) Bevan, M. A.; Prieve, D. C. Hindered Diffusion of Colloidal Particles Very

near to a Wall: Revisited. *J. Chem. Phys.* **2000**, *113* (3), 1228–1236.

(16) Stocco, A.; Chollet, B.; Wang, X.; Blanc, C.; Nobili, M. Rotational Diffusion of Partially Wetted Colloids at Fluid Interfaces. *J. Colloid Interface Sci.* **2019**, *542*, 363–369.

(17) Shah, A. A.; Schultz, B.; Zhang, W.; Glotzer, S. C.; Solomon, M. J. Actuation of Shape-Memory Colloidal Fibres of Janus Ellipsoids. *Nat Mater* **2015**, *14* (1), 117–124.

(18) Tanaka, T.; Okayama, M.; Minami, H.; Okubo, M. Dual Stimuli-Responsive "Mushroom-like" Janus Polymer Particles as Particulate Surfactants †. *Langmuir* **2010**, *26* (14), 11732–11736.

(19) Wang, S.; Ma, F.; Zhao, H.; Wu, N. The Bulk Synthesis of Metal-Organic Hybrid Dimers and Their Propulsion under Electric Fields The Bulk Synthesis of Metal-Organic Hybrid Dimers and Their Propulsion under Electric Fields. **2014**.

(20) Walther, A.; Muller, A. H. E. Janus Particles. *Soft Matter* **2008**, *4* (4), 663–668.

(21) Yang, L.; Wang, T.; Yang, X.; Jiang, G.; Luckham, P. F.; Xu, J.; Li, X.; Ni, X. Highly Stabilized Foam by Adding Amphiphilic Janus Particles for Drilling a Higherature and High-Calcium Geothermal Well. *Ind. Eng. Chem. Res.* **2019**, *58* (23), 9795–9805.

(22) Uemura, T.; Kaseda, T.; Kitagawa, S. Controlled Synthesis of Anisotropic Polymer Particles Templated by Porous Coordination Polymers. *Chem. Mater.* **2013**, *25* (18), 3772–3776.

(23) Basavaraj Madivala, Steven Vandebril, J. F. and J. V. Exploiting Particle Shape in Solid Stabilized Emulsions. *Soft Matter* **2009**, *5* (8), 1717–1727.

(24) Jaemyung KimLaura J. CoteFranklin KimWa YuanKenneth R. ShullJiaxing Huang. Graphene Oxide Sheets at Interfaces. *J. Am. Chem. Soc.* **2010**, *132* (23), 8180–8186.

(25) Basavaraj, S. V. D. G. Emulsions Stabilized by Silica Rods via Arrested Demixing. *Langmuir* **2015**, *31* (24), 6649–6654.

(26) Irina Kalashnikova, Herve Bizot, Patricia Bertoncini, B. C. and I. C. Cellulosic Nanorods of Various Aspect Ratios for Oil in Water Pickering Emulsions. *Soft Matter* **2012**, *9* (3), 952–959.

(27) Pappaert, K.; Van Hummelen, P.; Vanderhoeven, J.; Baron, G. V.; Desmet, G. Diffusion-Reaction Modelling of DNA Hybridization Kinetics on Biochips. *Chem. Eng. Sci.* **2003**, *58* (21), 4921–4930.

(28) Yang, F.; Qian, S.; Zhao, Y.; Qiao, R. Self-Diffusiophoresis of Janus Catalytic Micromotors in Confined Geometries. *Langmuir* **2016**, *32* (22), 5580–5592.

(29) Lin, T.; Shen, B.; Chen, W.; Zhang, X. B. Interaction Mechanisms Associated with Organic Colloid Fouling of Ultrafiltration Membrane in a Drinking Water Treatment System. *Desalination* **2014**, *332* (1), 100–108.

(30) Linkhorst, J.; Beckmann, T.; Go, D.; Kuehne, A. J. C.; Wessling, M.

Microfluidic Colloid Filtration. *Sci. Rep.* **2016**, *6* (March), 1–8.

(31) Prieve, D. C. Measurement of Colloidal Forces with TIRM. *Adv. Colloid Interface Sci.* **1999**, *82* (1), 93–125.

(32) Prieve, D. C.; Frej, N. A. Total Internal Reflection Microscopy: A Quantitative Tool for the Measurement of Colloidal Forces. **1990**, No. 6, 396–403.

(33) Royall, C. P.; Louis, A. A.; Tanaka, H. Measuring Colloidal Interactions with Confocal Microscopy. *J. Chem. Phys.* **2007**, *127* (4), 4–6.

(34) Prasad, V.; Semwogerere, D.; Weeks, E. R. Confocal Microscopy of Colloids. *J. Phys. Condens. Matter* **2007**, *19* (11), 113102.

(35) Mukhija, D.; Solomon, M. J. Translational and Rotational Dynamics of Colloidal Rods by Direct Visualization with Confocal Microscopy. *J. Colloid Interface Sci.* **2007**, *314* (1), 98–106.

(36) Kim, J. Y.; Weon, B. M. Confocal Microscopy of Colloidal Suspensions. *Appl. Microsc.* **2014**, *44* (1), 30–33.

(37) Fung, J.; Martin, K. E.; Perry, R. W.; Kaz, D. M.; McGorty, R.; Manoharan, V. N. Measuring Translational, Rotational, and Vibrational Dynamics in Colloids with Digital Holographic Microscopy. *Opt. Express* **2011**, *19* (9), 8051.

(38) Rashidi, A.; Wirth, C. L. Motion of a Janus Particle Very near a Wall. *J. Chem. Phys.* **2017**, *147* (22), 224906.

(39) Rashidi, A.; Issa, M. W.; Martin, I. T.; Avishai, A.; Razavi, S.; Wirth, C. L. Local Measurement of Janus Particle Cap Thickness. *ACS Appl. Mater. Interfaces* **2018**, *10*, 30935–30929.

(40) Rashidi, A.; Razavi, S.; Wirth, C. L. Influence of Cap Weight on the Motion of a Janus Particle Very near a Wall. **2020**.

(41) Berg, J. *An Introduction to Interfaces and Colloids*, 1st ed.; World Scientific, 2010.

(42) Butt, H.-J.; Cappella, B.; Kappl, M. Force Measurements with the Atomic Force Microscope: Technique, Interpretation and Applications. *Surf. Sci. Rep.* **2005**, *59* (1–6), 1–152.

(43) Israelachvili, J.; Min, Y.; Akbulut, M.; Alig, A.; Carver, G.; Greene, W.; Kristiansen, K.; Meyer, E.; Pesika, N.; Rosenberg, K.; et al. Recent Advances in the Surface Forces Apparatus (SFA) Technique. *Reports Prog. Phys.* **2010**, *73* (3), 036601.

(44) Prieve, D. C. Measurement of Colloidal Forces with TIRM. *Adv. Colloid Interface Sci.* **1999**, *82* (1–3), 93–125.

(45) Bevan, M. A.; Eichmann, S. L. Optical Microscopy Measurements of KT-Scale Colloidal Interactions. *Curr. Opin. Colloid Interface Sci.* **2011**, *16* (2), 149–157.

(46) Flicker, S. G.; Bike, S. G. Measuring Double Layer Repulsion Using Total Internal Reflection Microscopy. *Langmuir* **1993**, *9* (10), 257–262.

(47) Bevan, M. A.; Prieve, D. C. Direct Measurement of Retarded van Der Waals Attraction. *Langmuir* **1999**, *15* (23), 7925–7936.

(48) Bevan, M. A.; Scales, P. J. Solvent Quality Dependent Interactions and Phase Behavior of Polystyrene Particles with Physisorbed PEO-PPO-PEO. *Langmuir* **2002**, *18* (5), 1474–1484.

(49) Edwards, T. D.; Bevan, M. A. Depletion-Mediated Potentials and Phase Behavior for Micelles, Macromolecules, Nanoparticles, and Hydrogel Particles. *Langmuir* **2012**, *28* (39), 13816–13823.

(50) Wirth, C. L.; Sides, P. J.; Prieve, D. C. The Imaging Ammeter. *J. Colloid Interface Sci.* **2011**, *357* (1), 1–12.

(51) Hertlein, C.; Helden, L.; Gambassi, A.; Dietrich, S.; Bechinger, C. Direct Measurement of Critical Casimir Forces. *Nature* **2008**, *451* (7175), 172–175.

(52) Helden, L.; Dietrich, K.; Bechinger, C. Interactions of Colloidal Particles and Droplets with Water-Oil Interfaces Measured by Total Internal Reflection Microscopy. *Langmuir* **2016**, *32* (51), 13752–13758.

(53) Eichmann, S. L.; Smith, B.; Meric, G.; Fairbrother, D. H.; Bevan, M. a. Imaging Carbon Nanotube Interactions , Di Ff Usion , and Stability in Nanopores. **2011**, No. 7, 5909–5919.

(54) Glotzer, S. C.; Solomon, M. J. Anisotropy of Building Blocks and Their Assembly into Complex Structures. *Nat. Mater.* **2007**, *6* (7), 557–562.

(55) He, Z.; Kretzschmar, I. Template-Assisted GLAD: Approach to Single and Multipatch Patchy Particles with Controlled Patch Shape. *Langmuir* **2013**, *29* (51), 15755–15761.

(56) Hong, L.; Jiang, S.; Granick, S. Simple Method to Produce Janus Colloidal Particles in Large Quantity. *Langmuir* **2006**, *22* (23), 9495–9499.

(57) Shah, A. A.; Schultz, B.; Kohlstedt, K. L.; Glotzer, S. C.; Solomon, M. J. Synthesis, Assembly, and Image Analysis of Spheroidal Patchy Particles. *Langmuir* **2013**, *29* (15), 4688–4696.

(58) Liu, Y.; Li, W.; Perez, T.; Gunton, J. D.; Brett, G. Self Assembly of Janus Ellipsoids. *Langmuir* **2012**, *28* (1), 3–9.

(59) Miller, W. L.; Cacciuto, A. Hierarchical Self-Assembly of Asymmetric Amphiphatic Spherical Colloidal Particles. *Phys. Rev. E - Stat. Nonlinear, Soft Matter Phys.* **2009**, *80* (2), 1–6.

(60) Chen, Q.; Whitmer, J. K.; Jiang, S.; Bae, S. C.; Luijten, E.; Granick, S. Supracolloidal Reaction Kinetics of Janus Spheres. *Science* **2011**, *331* (6014), 199–202.

(61) Hunter, G. L.; Edmond, K. V.; Elsesser, M. T.; Weeks, E. R. Tracking Rotational Diffusion of Colloidal Clusters. *Opt. Commun.* **2011**, *19* (18), 17189–17202.

(62) Cheong, F. C.; Grier, D. G. Rotational and Translational Diffusion of Copper Oxide Nanorods Measured with Holographic Video Microscopy. *Opt. Express*

2010, *18* (7), 6555–6562.

(63) Torres-Díaz, I.; Bevan, M. A. General Potential for Anisotropic Colloid–Surface Interactions. *Langmuir* **2017**, *33* (17), 4356–4365.

(64) Sholl, D. S.; Fenwick, M. K.; Atman, E.; Prieve, D. C. Brownian Dynamics Simulation of the Motion of a Rigid Sphere in a Viscous Fluid Very near a Wall. *J. Chem. Phys.* **2000**, *113* (20), 9268–9278.

(65) Holmqvist, P.; Dhont, J. K. G.; Lang, P. R. Colloidal Dynamics near a Wall Studied by Evanescent Wave Light Scattering: Experimental and Theoretical Improvements and Methodological Limitations. *J. Chem. Phys.* **2007**, *126* (4), 044707.

(66) Carbajal-Tinoco, M. D.; Lopez-Fernandez, R.; Arauz-Lara, J. L. Asymmetry in Colloidal Diffusion near a Rigid Wall. *Phys. Rev. Lett.* **2007**, *99* (13), 1–4.

(67) Bevan, M. A.; Prieve, D. C.; Bevan, M. A.; Prieve, D. C. Hindered Diffusion of Colloidal Particles Very near to a Wall : Revisited Hindered Diffusion of Colloidal Particles Very near to a Wall : Revisited. **2000**, *1228* (2000).

(68) Dean, W. R.; O'Neill, M. E. A Slow Motion of Viscous Liquid Caused by the Rotation of a Solid Sphere. *Mathematika* **1963**, *10* (01), 13.

(69) Maude, a D. The Movement of a Sphere in Front of a Plane at Low Reynolds Number. *Br. J. Appl. Phys.* **2002**, *14* (12), 894–898.

(70) Goldman, A. J.; Cox, R. G.; Brenner, H. Slow Viscous Motion of a Sphere Parallel to a Plane Wall-II Couette Flow. *Chem. Eng. Sci.* **1967**, *22* (4), 653–660.

(71) Goldman, A. J. Investigations in Low Reynolds Number Fluid-Particle Dynamics, New York University, 1966.

(72) Ermak, D. L.; McCammon, J. A. Brownian Dynamics with Hydrodynamic Interactions. *J. Chem. Phys.* **1978**, *69* (4), 1352–1360.

(73) Hütter, M.; Christian Öttinger, H. Fluctuation-Dissipation Theorem, Kinetic Stochastic Integral and Efficient Simulations. *J. Chem. Soc. Faraday Trans.* **1998**, *94* (10), 1403–1405.

(74) ten Hagen, B.; van Teeffelen, S.; Löwen, H. Non-Gaussian Behaviour of a Self-Propelled Particle on a Substrate. *Condens. Matter Phys.* **2009**, *12* (4), 725–738.

(75) Dickinson, B. Y. E.; Allison, S. A.; Andrew, J. Brownian Dynamics with Rotation-Translation Coupling. **1985**, 591–601.

(76) Hotta, Y.; Alberius, P. C. A.; Bergström, L. Coated Polystyrene Particles as Templates for Ordered Macroporous Silica Structures with Controlled Wall Thickness. *J. Mater. Chem.* **2003**, *13* (3), 496–501.

(77) Buttinoni, I.; Bialk??, J.; K??mmel, F.; L??wen, H.; Bechinger, C.; Speck, T. Dynamical Clustering and Phase Separation in Suspensions of Self-Propelled Colloidal Particles. *Phys. Rev. Lett.* **2013**, *110* (23), 1–5.

(78) Zhang, J.; Luijten, E.; Granick, S. Toward Design Rules of Directional Janus

Colloidal Assembly. *Annu. Rev. Phys. Chem.* **2015**, *66* (1), 581–600.

(79) Ding, H.; Ma, Y. Interactions between Janus Particles and Membranes. *Nanoscale* **2012**, *4* (4), 1116–1122.

(80) Crossley, S.; Faria, J.; Shen, M.; Resasco, D. E. Solid Nanoparticles That Catalyze Biofuel Upgrade Reactions at the Water/Oil Interface. *Science (80-.).* **2010**, *327* (5961), 68–72.

(81) Tu, F.; Lee, D. Shape-Changing and Amphiphilicity-Reversing Janus Particles with PH-Responsive Surfactant Properties. *J. Am. Chem. Soc.* **2014**, *136* (28), 9999–10006.

(82) Bahrami, R.; Löbling, T. I.; Gröschel, A. H.; Schmalz, H.; Müller, A. H. E.; Altstädt, V. The Impact of Janus Nanoparticles on the Compatibilization of Immiscible Polymer Blends under Technologically Relevant Conditions. *ACS Nano* **2014**, *8* (10), 10048–10056.

(83) Tu, F.; Lee, D. One-Step Encapsulation and Triggered Release Based on Janus Particle-Stabilized Multiple Emulsions. *Chem. Commun.* **2014**, *50* (98), 15549–15552.

(84) Walther, A.; Müller, A. H. E. Janus Particles: Synthesis, Self-Assembly, Physical Properties, and Applications. *Chem. Rev.* **2013**, *113* (7), 5194–5261.

(85) Zarzar, L. D.; Sresht, V.; Sletten, E. M.; Kalow, J. A.; Blankschtein, D.; Swager, T. M. Dynamically Reconfigurable Complex Emulsions via Tunable Interfacial Tensions. *Nature* **2015**, *518* (7540), 520–524.

(86) Zhang, J.; Grzybowski, B. A.; Granick, S. Janus Particle Synthesis, Assembly, and Application. *Langmuir* **2017**, *33* (28), 6964–6977.

(87) Chaudhary, K.; Chen, Q.; Juárez, J. J.; Granick, S.; Lewis, J. A. Janus Colloidal Matchsticks. *J. Am. Chem. Soc.* **2012**, *134* (31), 12901–12903.

(88) De Leon, A. C.; Rodier, B. J.; Luo, Q.; Hemmingsen, C. M.; Wei, P.; Abbasi, K.; Advincula, R.; Pentzer, E. B. Distinct Chemical and Physical Properties of Janus Nanosheets. *ACS Nano* **2017**, *11* (7), 7485–7493.

(89) Binks, B. P.; Lumsdon, S. O. Influence of Particle Wettability on the Type and Stability of Surfactant-Free Emulsions †. *Langmuir* **2000**, *16* (23), 8622–8631.

(90) Du, Z.; Bilbao-Montoya, M. P.; Binks, B. P.; Dickinson, E.; Ettelaie, R.; Murray, B. S. Outstanding Stability of Particle-Stabilized Bubbles. *Langmuir* **2003**, *19* (8), 3106–3108.

(91) Binks, B. P.; Lumsdon, S. O. Pickering Emulsions Stabilized by Monodisperse Latex Particles: Effects of Particle Size. *Langmuir* **2001**, *17* (15), 4540–4547.

(92) Ergun, R.; Hartel, R. W.; Spicer, P. T. Kinetic Effects on Interfacial Partitioning of Fat Crystals. *Food Struct.* **2015**, *5*, 1–9.

(93) Takei, H.; Shimizu, N. Gradient Sensitive Microscopic Probes Prepared by Gold Evaporation and Chemisorption on Latex Spheres. *Langmuir* **1997**, *13* (7), 1865–1868.

(94) Pawar, A. B.; Kretzschmar, I. Multifunctional Patchy Particles by Glancing

Angle Deposition. *Langmuir* **2009**, *25* (16), 9057–9063.

(95) Pawar, A. B.; Kretzschmar, I. Patchy Particles by Glancing Angle Deposition. *Langmuir* **2008**, *24* (2), 355–358.

(96) Pawar, A. B.; Kretzschmar, I. Fabrication, Assembly, and Application of Patchy Particles. *Macromol. Rapid Commun.* **2010**, *31* (2), 150–168.

(97) Crocker, J.; Grier, D. Methods of Digital Video Microscopy for Colloidal Studies. *J. Colloid Interface Sci.* **1996**, *179* (1), 298–310.

(98) Wang, X.; In, M.; Blanc, C.; Würger, A.; Nobili, M.; Stocco, A. Janus Colloids Actively Rotating on the Surface of Water. *Langmuir* **2017**, *33* (48), 13766–13773.

(99) Avishai, A.; Yin, X.; Trapp, B.; Kidd, G. Focused Ion Beam-Based Three Dimensional Analysis of Optic Nerve Axons. *Microsc. Microanal.* **2009**, *15* (S2), 346–347.

(100) Mustafi, D.; Avishai, A.; Avishai, N.; Engel, A.; Heuer, A.; Palczewski, K. Serial Sectioning for Examination of Photoreceptor Cell Architecture by Focused Ion Beam Technology. *J. Neurosci. Methods* **2011**, *198* (1), 70–76.

(101) Kidd, G.; Avishai, A.; Yin, X.; Trapp, B. Three-Dimensional Analysis of Optic Nerve Axons Using a Focused Ion Beam-Based Appraoch. *Microscopy Today*. 2010, pp 18–22.

(102) Royer, J. R.; Burton, G. L.; Blair, D. L.; Hudson, S. D. Rheology and Dynamics of Colloidal Superballs. *Soft Matter* **2015**, *11* (28), 5656–5665.

(103) Nisisako, T.; Torii, T.; Takahashi, T.; Takizawa, Y. Synthesis of Monodisperse Bicolored Janus Particles with Electrical Anisotropy Using a Microfluidic Co-Flow System. *Adv. Mater.* **2006**, *18* (9), 1152–1156.

(104) Lee, S. H.; Liddell, C. M. Anisotropic Magnetic Colloids: A Strategy to Form Complex Structures Using Nonspherical Building Blocks. *Small* **2009**, *5* (17), 1957–1962.

(105) Kim, Y.; Shah, A. a; Solomon, M. J. Spatially and Temporally Reconfigurable Assembly of Colloidal Crystals. *Nat. Commun.* **2014**, *5*, 3676.

(106) Tu, F.; Park, B. J.; Lee, D. Thermodynamically Stable Emulsions Using Janus Dumbbells as Colloid Surfactants. *Langmuir* **2013**, *29* (41), 12679–12687.

(107) Shemi, O.; Solomon, M. J. Effect of Surface Chemistry and Metallic Layer Thickness on the Clustering of Metallodielectric Janus Spheres. *Langmuir* **2014**, *30* (51), 15408–15415.

(108) Kagan, D.; Laocharoensuk, R.; Zimmerman, M.; Clawson, C.; Balasubramanian, S.; Kang, D.; Bishop, D.; Sattayasamitsathit, S.; Zhang, L.; Wang, J. Rapid Delivery of Drug Carriers Propelled and Navigated by Catalytic Nanoshuttles. *Small* **2010**, *6* (23), 2741–2747.

(109) Kim, H.; Cho, J.; Cho, J.; Park, B. J.; Kim, J. W. Magnetic-Patchy Janus Colloid Surfactants for Reversible Recovery of Pickering Emulsions. *ACS Appl. Mater. Interfaces* **2018**, *10* (1), 1408–1414.

(110) Bradley, L. C.; Stebe, K. J.; Lee, D. Clickable Janus Particles. *J. Am. Chem. Soc.* **2016**, *138* (36), 11437–11440.

(111) Salgado-Blanco, D.; Mendoza, C. I. Self-Assembly of Anisotropic Soft Particles in Two Dimensions. *Eur. Phys. J. E* **2013**, *36* (4).

(112) Chen, W. H.; Tu, F.; Bradley, L. C.; Lee, D. Shape-Tunable Synthesis of Sub-Micrometer Lens-Shaped Particles via Seeded Emulsion Polymerization. *Chem. Mater.* **2017**, *29* (7), 2685–2688.

(113) Murphy, R. P.; Hong, K.; Wagner, N. J. Synthetic Control of the Size, Shape, and Polydispersity of Anisotropic Silica Colloids. *J. Colloid Interface Sci.* **2017**, *501*, 45–53.

(114) Shemi, O.; Solomon, M. J. Self-Propulsion and Active Motion of Janus Ellipsoids. *J. Phys. Chem. B* **2018**, *122* (44), 10247–10255.

(115) Fallahi-Sambaran, M.; Salami-Kalajahi, M.; Dehghani, E.; Abbasi, F. Investigation of Different Core-Shell toward Janus Morphologies by Variation of Surfactant and Feeding Composition: A Study on the Kinetics of DOX Release. *Colloids Surfaces B Biointerfaces* **2018**, *170* (May), 578–587.

(116) Kierulf, A.; Azizi, M.; Eskandarloo, H.; Whaley, J.; Liu, W.; Perez-herrera, M.; You, Z.; Abbaspourrad, A. Food Hydrocolloids Starch-Based Janus Particles : Proof-of-Concept Heterogeneous Design via a Spin-Coating Spray Approach. *Food Hydrocoll.* **2019**, *91* (January), 301–310.

(117) Du, J.; O'Reilly, R. K. Anisotropic Particles with Patchy, Multicompartment and Janus Architectures: Preparation and Application. *Chem. Soc. Rev.* **2011**, *40* (5), 2402.

(118) Mohajerani, F.; Zhao, X.; Somasundar, A.; Velegol, D.; Sen, A. A Theory of Enzyme Chemotaxis: From Experiments to Modeling. *Biochemistry* **2018**, *57*, 6256–6263.

(119) Nili, H.; Naji, A. Re-Entrant Bimodality in Spheroidal Chiral Swimmers in Shear Flow. *Sci. Rep.* **2018**, *8* (1), 1–9.

(120) Mitchell, W. H.; Spagnolie, S. E. Sedimentation of Spheroidal Bodies near Walls in Viscous Fluids: Glancing, Reversing, Tumbling and Sliding. *J. Fluid Mech.* **2015**, *772*, 600–629.

(121) Padding, J. T.; Briels, W. J. Translational and Rotational Friction on a Colloidal Rod near a Wall. *J. Chem. Phys.* **2010**, *132* (5).

(122) Das, S.; Garg, A.; Campbell, A. I.; Howse, J.; Sen, A.; Velegol, D.; Golestanian, R.; Ebbens, S. J. Boundaries Can Steer Active Janus Spheres. *Nat. Commun.* **2015**, *6*, 1–10.

(123) Wirth, C. L.; Nuthalapati, S. H. Response of a Doublet to a Nearby Dc Electrode of Uniform Potential. *Phys. Rev. E* **2016**, *94* (4), 1–9.

(124) Gangwal, S.; Cayre, O. J.; Velev, O. D. Dielectrophoretic Assembly of Metallodielectric Janus Particles in AC Electric Fields. *Langmuir* **2008**, *24* (23), 13312–13320.

(125) Delong, S.; Balboa Usabiaga, F.; Donev, A. Brownian Dynamics of Confined Rigid Bodies. *J. Chem. Phys.* **2015**, *143* (14), 1–54.

(126) Ota, S.; Li, T.; Li, Y.; Ye, Z.; Labno, A.; Yin, X.; Alam, M. R.; Zhang, X. Brownian Motion of Tethered Nanowires. *Phys. Rev. E - Stat. Nonlinear, Soft Matter Phys.* **2014**, *89* (5), 1–10.

(127) Wittmeier, A.; Leeth Holterhoff, A.; Johnson, J.; Gibbs, J. G. Rotational Analysis of Spherical, Optically Anisotropic Janus Particles by Dynamic Microscopy. *Langmuir* **2015**, *31* (38), 10402–10410.

(128) Cui, J.; Long, D.; Shapturenka, P.; Kretzschmar, I.; Chen, X.; Wang, T. Janus Particle-Based Microprobes: Determination of Object Orientation. *Colloids Surfaces A Physicochem. Eng. Asp.* **2017**, *513*, 452–462.

(129) Zheng, Z.; Han, Y. Self-Diffusion in Two-Dimensional Hard Ellipsoid Suspensions. *J. Chem. Phys.* **2010**, *133* (12), 1–11.

(130) Mangal, R.; Nayani, K.; Kim, Y. K.; Bukusoglu, E.; Córdova-Figueroa, U. M.; Abbott, N. L. Active Janus Particles at Interfaces of Liquid Crystals. *Langmuir* **2017**, *33* (41), 10917–10926.

(131) Campbell, A. I.; Wittkowski, R.; Ten Hagen, B.; Löwen, H.; Ebbens, S. J. Helical Paths, Gravitaxis, and Separation Phenomena for Mass-Anisotropic Self-Propelling Colloids: Experiment versus Theory. *J. Chem. Phys.* **2017**, *147* (8).

(132) Campbell, A. I.; Ebbens, S. J.; Illien, P.; Golestanian, R. Experimental Observation of Flow Fields Around Active Janus Spheres. **2018**, 1–10.

(133) Campbell, A. I.; Ebbens, S. J. Gravitaxis in Spherical Janus Swimming Devices. *Langmuir* **2013**, *29* (46), 14066–14073.

(134) Simmchen, J.; Katuri, J.; Uspal, W. E.; Popescu, M. N.; Tasinkevych, M.; Sánchez, S. Topographical Pathways Guide Chemical Microswimmers. *Nat. Commun.* **2016**, *7* (May 2015), 1–9.

(135) Liu, B.; Böker, A. Measuring Rotational Diffusion of Colloidal Spheres with Confocal Microscopy. *Soft Matter* **2016**, *12* (28), 6033–6037.

(136) Lisicki, M.; Cichocki, B.; Rogers, S. A.; Dhont, J. K. G.; Lang, P. R. Translational and Rotational Near-Wall Diffusion of Spherical Colloids Studied by Evanescent Wave Scattering. *Soft Matter* **2014**, *10* (24), 4312.

(137) Colin, R.; Yan, M.; Chevry, L.; Berret, J.-F.; Abou, B. 3D Rotational Diffusion of Micrometric Wires Using 2D Video Microscopy. *EPL (Europhysics Lett.* **2012**, *97* (3), 30008.

(138) Yu, X.; Hong, J.; Liu, C.; Kim, M. K. Review of Digital Holographic Microscopy for Three-Dimensional Profiling and Tracking. *Opt. Eng.* **2014**, *53* (11), 112306.

(139) Wang, A.; Dimiduk, T. G.; Fung, J.; Razavi, S.; Kretzschmar, I.; Chaudhary, K.; Manoharan, V. N. Using the Discrete Dipole Approximation and Holographic Microscopy to Measure Rotational Dynamics of Non-Spherical Colloidal Particles. *J. Quant. Spectrosc. Radiat. Transf.* **2014**, *146*, 499–509.

(140) Hsiao, L. C.; Saha-Dalal, I.; Larson, R. G.; Solomon, M. J. Translational and Rotational Dynamics in Dense Suspensions of Smooth and Rough Colloids. *Soft Matter* **2017**, *13*, 9229–9236.

(141) Han, Y.; Alsayed, A.; Nobili, M.; Yodh, A. G. Quasi-Two-Dimensional Diffusion of Single Ellipsoids: Aspect Ratio and Confinement Effects. *Phys. Rev. E - Stat. Nonlinear, Soft Matter Phys.* **2009**, *80* (1), 1–6.

(142) Shields, C. W.; Han, K.; Ma, F.; Miloh, T.; Yossifon, G.; Velev, O. D. Supercolloidal Spinners: Complex Active Particles for Electrically Powered and Switchable Rotation. *Adv. Funct. Mater.* **2018**, *28* (35), 1–7.

(143) Sharifi-Mood, N.; Mozaffari, A.; Córdova-Figueroa, U. M. Pair Interaction of Catalytically Active Colloids: From Assembly to Escape. *J. Fluid Mech.* **2016**, *798*, 910–954.

(144) Zaeifi Yamchi, M.; Naji, A. Effective Interactions between Inclusions in an Active Bath. *J. Chem. Phys.* **2017**, *147* (19).

(145) Bechinger, C.; Di Leonardo, R.; Löwen, H.; Reichhardt, C.; Volpe, G.; Volpe, G. Active Particles in Complex and Crowded Environments. *Rev. Mod. Phys.* **2016**, *88* (4).

(146) Bayati, P.; Najafi, A. Dynamics of Two Interacting Active Janus Particles. *J. Chem. Phys.* **2016**, *144* (13), 134901.

(147) Jalilvand, Z.; Pawar, A.; Kretzschmar, I. Experimental Study of the Motion of Patchy Particle Swimmers near a Wall. *Langmuir* **2018**, acs.langmuir.8b03220.

(148) Das, S.; Jalilvand, Z.; Popescu, M. N.; Uspal, W. E.; Dietrich, S.; Kretzschmar, I. Floor- or Ceiling-Sliding for Chemically Active, Gyrotactic, Sedimenting Janus Particles. *Langmuir* **2020**, acs.langmuir.9b03696.

(149) Mozaffari, A.; Sharifi-Mood, N.; Koplik, J.; Maldarelli, C. Self-Propelled Colloidal Particle Near a Planar Wall: A Brownian Dynamics Study. *Phys. Rev. FLUIDS* **2018**, *014104*.

(150) Sánchez, J. H.; Rinaldi, C. Rotational Brownian Dynamics Simulations of Non-Interacting Magnetized Ellipsoidal Particles in d.c. and a.c. Magnetic Fields. *J. Magn. Magn. Mater.* **2009**, *321* (19), 2985–2991.

(151) De Corato, M.; Greco, F.; D'Avino, G.; Maffettone, P. L. Hydrodynamics and Brownian Motions of a Spheroid near a Rigid Wall. *J. Chem. Phys.* **2015**, *142* (19), 194901.

(152) Nayeri, M.; Abbas, Z.; Bergenholtz, J. Measurements of Screening Length in Salt Solutions by Total Internal Reflection Microscopy: Influence of van Der Waals Forces and Instrumental Noise. *Colloids Surfaces A Physicochem. Eng. Asp.* **2013**, *429*, 74–81.

(153) Goldman, A. J.; Cox, R. G.; Brenner, H. Slow Viscous Motion of a Pshere Parallel to a Plane Wall - I Motion through a Quiescent Fluid. *Chem. Eng. Sci.* **1967**, *22*, 637–651.

(154) Tsuda, A.; Henry, F. S.; Butler, J. P. Particle Transport and Deposition: Basic Physics of Particle Kinetics. In *Comprehensive Physiology*; John Wiley &

Sons, Inc.: Hoboken, NJ, USA, 2013; pp 1437–1471.

(155) Edmond, K. V.; Elsesser, M. T.; Hunter, G. L.; Pine, D. J.; Weeks, E. R. Decoupling of Rotational and Translational Diffusion in Supercooled Colloidal Fluids. *Proc. Natl. Acad. Sci.* **2012**, *109* (44), 17891–17896.

(156) Anthony, S. M.; Kim, M.; Granick, S. Single-Particle Tracking of Janus Colloids in Close Proximity. *Langmuir* **2008**, *24* (13), 6557–6561.

(157) Strubbe, F.; Robben, B.; Puthenparampil George, J.; Amer Cid, Í.; Beunis, F.; Neyts, K. Axial Electrokinetic Trapping of Anisotropic Particles. *Sci. Rep.* **2019**, *9* (1), 1–11.

(158) Cheng, Y.; Zhu, C.; Xie, Z.; Gu, H.; Tian, T.; Zhao, Y.; Gu, Z. Anisotropic Colloidal Crystal Particles from Microfluidics. *J. Colloid Interface Sci.* **2014**, *421*, 64–70.

(159) Sacanna, S.; Pine, D. J. Shape-Anisotropic Colloids: Building Blocks for Complex Assemblies. *Curr. Opin. Colloid Interface Sci.* **2011**, *16* (2), 96–105.

(160) Doicu, A.; Vasilyeva, A. A.; Efremenko, D. S.; Wirth, C. L.; Wriedt, T. A Light Scattering Model for Total Internal Reflection Microscopy of Geometrically Anisotropic Particles. *J. Mod. Opt.* **2019**, *Just accep*, 1–22.

(161) Li, Z. W.; Zhu, Y. L.; Lu, Z. Y.; Sun, Z. Y. General Patchy Ellipsoidal Particle Model for the Aggregation Behaviors of Shape- and/or Surface-Anisotropic Building Blocks. *Soft Matter* **2018**, *14* (37), 7625–7633.

(162) Torres-Díaz, I.; Bevan, M. A. General Potential for Anisotropic Colloid-Surface Interactions. *Langmuir* **2017**, *33* (17), 4356–4365.

(163) Solomon, M. J.; Zeitoun, R.; Ortiz, D.; Sung, K. E.; Deng, D.; Shah, A.; Burns, M. A.; Glotzer, S. C.; Millunchick, J. M. Toward Assembly of Non-Close-Packed Colloidal Structures from Anisotropic Pentamer Particles. *Macromol. Rapid Commun.* **2010**, *31* (2), 196–201.

(164) Jalilvand, Z.; Haider, H.; Cui, J.; Kretzschmar, I. Pt-SiO2 Janus Particles and the Water/Oil Interface – A Competition Between Motility and Thermodynamics. *Langmuir* **2020**, acs.langmuir.9b03454.

(165) Najafi, H.; Jerri, H. A.; Valmacco, V.; Petroff, M.; Hansen, C.; Benczédi, D.; Bevan, M. A. Synergistic Polymer-Surfactant Complex Mediated Colloidal Interactions & Deposition Synergistic Polymer-Surfactant Complex Mediated Colloidal Interactions & Deposition. **2020**.

(166) Nano, A. C. S. Confined 1D Propulsion of Metallodielectric Janus Micromotors on Microelectrodes Under AC Electric Fields. **2019**.

(167) Sato, M. Self-Assembly Formed by Spherical Patchy Particles with Long-Range Attraction. **2019**.

(168) Flicker, S. G.; Tipa, J. L.; Bike, S. G. Quantifying Double-Layer Repulsion between a Colloidal Sphere and a Glass Plate Using Total Internal Reflection Microscopy. *Journal of Colloid and Interface Science*. 1993, pp 317–325.

(169) Wirth, C. L.; Sides, P. J.; Prieve, D. C. Electrolyte Dependence of Particle

Motion near an Electrode during Ac Polarization. *Phys. Rev. E - Stat. Nonlinear, Soft Matter Phys.* **2013**, *87* (3), 1–11.

(170) Bevan, M. A.; Prieve, D. C. Direct Measurement of Retarded van Der Waals Attraction.Pdf. **1999**, *1* (4), 7925–7936.

(171) Xia, A.; Yang, S.; Zhang, R.; Ni, L.; Xing, X.; Jin, F. Imaging the Separation Distance between the Attached Bacterial Cells and the Surface with a Total Internal Reflection Dark-Field Microscope. *Langmuir* **2019**, *35* (26), 8860–8866.

(172) Swavola, J. C.; Edwards, T. D.; Bevan, M. A. Direct Measurement of Macromolecule-Coated Colloid-Mucus Interactions. *Langmuir* **2015**, *31* (33), 9076–9085.

(173) Liu, Y.; Bławzdziewicz, J.; Cichocki, B.; Dhont, J. K. G.; Lisicki, M.; Wajnryb, E.; Young, Y. N.; Lang, P. R. Near-Wall Dynamics of Concentrated Hard-Sphere Suspensions: Comparison of Evanescent Wave DLS Experiments, Virial Approximation and Simulations. *Soft Matter* **2015**, *11* (37), 7316–7327.

(174) McKelvy, M. L.; Britt, T. R.; Davis, B. L.; Gillie, J. K.; Lentz, L. A.; Leugers, A.; Nyquist, R. A.; Putzig, C. L. Infrared Spectroscopy. *Anal. Chem.* **1996**, *68* (12), 93–160.

(175) Nootz, G. Fit 2D Gaussian Function to Data (Https://Www.Mathworks.Com/Matlabcentral/Fileexchange/37087-Fit-2d-Gaussian-Function-to-Data). MATLAB Central File Exchange 2020.

APPENDIX 2.1

MATLAB code to track motion of a chemically Janus particle near a boundary

```
% Last edit 01/10/2018
% Developed by Aidin Rashidi
% MATLAB code to track motion of a chemically Janus particle near a
boundary
rng('shuffle')
%%%   File Name Detection
%%%   Particle Size/Material/zpA/zpB/zs/Electrolit C/ N of
Iteration/Mesh/Date
%%%   6PS-50 10 50-1-240-101-110316

%%%% Middle height %%%%%%%%%%%%%%%%%%%%%%%%%%%%%%%%%%%%%%%%%%%%%%%%%%
disp('Have you changed the file name')
string=input('If yes please enter "y" else enter "N" ');

if string ~= 'y'
    return
end

tic
clc;
clear all;

Meshf=101;         % Number of Meshes (Meshf * Meshf)

nTheta=90;

a=0.5E-6;            % Particle Radius [m]

N=4800000;             % Number of Iterations

NN=5*N/100;

dt=5E-3;           % delta t or time sequence [second]
zpA=-5E-3;        % Stern potential of particle A which we replace
with zeta potential [V]
zpB=-50E-3;        % Stern potential of particle B which we replace
with zeta potential [V]
zs= -50E-3  ;      % Stern potential of substrate which we replace
with zeta potential [V]
C=1E-3;            % Electrolyte concentration [Molar]
%%
zp= -100E-3;         % Stern potential of particle which we replace
with zeta potential [V]
```

```
h0=150E-9;          % initial height [m]

K=1.38065*10.^-23;% 1.3806488E-23; % Boltzmann constant [J/K]
T= 298;             % Temperature [Kelvin]
Mu= 0.000887;       % Dynamic viscosity of water - μ - [N s/m^2]
Bins_N=500;

Rohp=1055;          % Particle Density(kg/m^3)
Rohf=1000;          % Fluid Density(kg/m^3)
g=9.81;             % Specific gravity
NA=6.022E23;        % Avogadro's No.[1/mol]
e=1.602E-19;        % [colone]

z=1;
e0=8.854E-12;       % [colon^2/N/m^2] /// e=e0*er  e:dielectric
permittivity
er=78.304;          % Dielectric constant

D=zeros(N,1);          % Diffusion Coeifficient
DrTeta=zeros(N,1);     % Teta Diffusion Coeifficient
DrPHI=zeros(N,1);      % PHI Diffusion Coeifficient
dDdh=zeros(N,1);       % Derivative of the diffusion coeifficent
respect to height
h=zeros(N,1);          % height of the particle on the substrate [m]
Teta=zeros(N,1);       % Rotational Degree Function Teta
PHI=zeros(N,1);        % Rotational Degree Function PHI
hh=zeros(N,1);         % height of the particle on the substrate [nm]
F=zeros(N,1);          % Force on Particle ( Double Layer and
Gravitational Force )
H=zeros(N,1);          % Height Random Displacement
GT=zeros(N,1);         % Teta Rotationl Random Displacement
GP=zeros(N,1);         % PHI Rotationl Random Displacement
RNDH=zeros(N,1);
phi= zeros(N,1);       % potential energy
phi2= zeros(N,1);
Intensity= zeros(N,1);
DrTeta_NN=zeros(NN,1);
DrPHI_NN=zeros(NN,1) ;
MSD_Teta=zeros(NN,1) ;
MSD_PHI=zeros(NN,1);
Lagtime=zeros(NN,1);
MSD_h=zeros(N,1);

qq1_sum=zeros(nTheta,1);
hh_Theta_ave = zeros(nTheta,1);  % Average Height in each orientation
hh_Theta_prob_loc = zeros(nTheta,1);
hh_Theta_probable2 = zeros(nTheta,1);
hh_Theta_probable= zeros(nTheta,1);
hh_ave_sum= zeros(nTheta,1); % Summation of the heights in each
individual orientation

Teta_A=zeros(Meshf,Meshf);     % Teta Location of A part of Janus
Particle
PHI_A=zeros(Meshf,Meshf);      % Phi Location of A part of Janus
Particle
Sphere_Area=zeros(100,100,3); % 3rd layer Area of particle in
99(teta)*199(phi) mesh scale - 1st layer A_Teta (ZA) - 2nd layer
A_Phi (ZB)
Sphere_meshA=zeros(Meshf,Meshf,3);
```

```
erf_m=zeros(Meshf,Meshf);      % electrostatic repulsion force in each
mesh

k=((2*1000*NA*e^2*C*z^2)/(e0*er*K*T))^0.5;  % Debye parameter [1/m]
ggg=1/k;

I0=1;
Intensity(1)=I0;

Beta=1/83;            % Inverse decay length [1/nm] - incident angle
= 75 degree

B =
64*pi*er*e0*a*((K*T./e).^2)*tanh(e*zp./(4*K*T))*tanh(e*zs./(4*K*T));
% It is not valid for Janus Particle
% zp = atanh( B /tanh(e*zs./(4*K*T))/ 64/pi/er/e0/a/((K*T./e).^2))
*(4*K*T)/e
Gg=((4/3)*pi*a^3*(Rohp-Rohf)*9.81);       % Net Weight of Particle
Hm=(1/k)*log(k*B/Gg);                     % Calculating hm for Direct
Potential Calculation
phim= (B*exp(-k*(Hm))+ (Gg)*Hm) /(K*T);  % Calculating Potential for
Direct Potential Calculation
i=1;
h(1)=h0;

Teta_A0 =linspace(0,pi,Meshf);           % dividing zpA
PHI_A0 =linspace(pi/2,3*pi/2,Meshf);     % dividing zpA

Teta(1)=Teta_A0((Meshf-1)/2+1);          % Initial middle Position of
the Particle Respect to Substrate (zpA)
PHI(1)=PHI_A0((Meshf-1)/2+1);            % Initial middle Position of
the Particle Respect to Substrate (zpA)

%%% Teta_Area=linspace(pi/2,pi,51); % teta Area meshing {the lower
halfsphere is mentioned} (teta degree)
%%% Phi_Area=linspace(0,2*pi,101);  % Area meshing (phi degree)

 for i=1:Meshf
     Teta_A(i,:)=Teta_A0(i); %%%%(Teta_A0(i+1)+Teta_A0(i))/2;
 end

for i=1:Meshf
     PHI_A(:,i)=PHI_A0(i); %%%% ((PHI_A0(i+1)+PHI_A0(i))/2)';
 end

    ii=0;
    jj=0;

Sphere_meshA(:,:,1)= Teta_A;  % Theta degree
Sphere_meshA(:,:,2)= PHI_A';  % Phi degree

 %%%% A22=@(teta_cal) A11(teta_cal)/2*a*pi/100*(
(sin(teta_cal+pi/200))    + (sin(teta_cal-pi/200))  );  % straight
calculation of surface
 %%%% A22=@(teta_cal) a^2*(pi/50)*(cos(teta_cal+pi/100)-cos(teta_cal-
pi/100));  % Finding real sphere surface area
```

```
A22=@ (teta_cal) pi*a^2/(2*(Meshf-1))*abs(((sin(teta_cal))^2-
(sin(teta_cal-pi/(Meshf-1)))^2));  %%% Derjagun projected surface
area
%%%%%%%%%%%%%%%%%%%%
F_Derjaguin= k*B*exp(-k*h0);
erp_A = @(h)
64*1000*NA*C*(K*T)*tanh(e*zpA./(4*K*T))*tanh(e*zs./(4*K*T))*exp(-
k*h); % Electrostatic Repultion Pressure
erp_B = @(h)
64*1000*NA*C*(K*T)*tanh(e*zpB./(4*K*T))*tanh(e*zs./(4*K*T))*exp(-
k*h); % Electrostatic Repultion Pressure

%%
for i=1:N-1

    i

D(i)=K*T*((6*h(i)^2+2*a*h(i))/(6*h(i)^2+9*a*h(i)+2*a^2))/(6*pi*Mu*a);
%%%% [m^2/s]

  %%% DrTeta(i)= K*T/(8*pi*Mu*a^3)/(1+ (5/16)*(a/(a+h(i)))^3);  %%%%
[m/s] Ref[20]
    h_over_a=h(i)/a;
  if h_over_a <= 0.6
    DrTeta(i)= K*T/(8*pi*Mu*a^3)/(0.9641*(h(i)/a)^-0.1815);   %%%%
fitting and numerical method from Goldman (h/a) <= 0.6
  else
      if h_over_a > 0.6 && h_over_a  <=2
          DrTeta(i)= K*T/(8*pi*Mu*a^3)/(1.056*(h(i)/a)^-0.07286);
%%%% fitting and numerical method from Goldman 0.6 <(h/a) <= 2
      else
           DrTeta(i)= K*T/(8*pi*Mu*a^3)/(1);
      end
  end

  DrPHI(i)= K*T/(8*pi*Mu*a^3)*(1-1/8*(a/(a+h(i)))^3-
3/256*(a/(a+h(i)))^8); %%%%  Ref[20]

  dDdh(i)=K*T/(6*pi*Mu*a)*((((2*a + 12*h(i))*(2*a^2 + 9*a*h(i) +
6*h(i)^2)) - ((6*h(i)^2 + 2*a*h(i))*(9*a + 12*h(i))))/(2*a^2 +
9*a*h(i) + 6*h(i)^2)^2);

  variance_H=2*D(i)*dt;
  H(i)=sqrt(abs(variance_H))*randn(1,1);  % Random displacement
calculations

  [Sphere_meshA(:,:,1)]=TetaConv_mesh( Sphere_meshA(:,:,1) , Meshf );
% Converting the Theta values to values inside of [0 2*pi]

    for p=2:Meshf
        for j=2:Meshf
           if (  (   (pi/2<=Sphere_meshA(p,j,1)) &&
(Sphere_meshA(p,j,1)<3*pi/2)  ) || (   (-3*pi/2<Sphere_meshA(p,j,1))
&& (Sphere_meshA(p,j,1)<-pi/2 )  )       )
               %%%
erf_m(p,j)=erp_A(a*(1+cos(Sphere_meshA(p,j,1)))+h(i))*abs(-
cos(Sphere_meshA(p,j,1))*Sphere_meshA(p,j,3));%% abs(-
sin(Sphere_meshA(p,j,1)-
pi/2)*a^2*(pi/100)^2*(sin(Sphere_meshA(p,j,1)))); %%%abs(-
```

```
sin(Sphere_meshA(p,j,1)-
pi/2)*a^2*(pi/100)*(cos(Sphere_meshA(p,j,1)+pi/200)-
cos(Sphere_meshA(p,j,1)-pi/200)));
                    if  abs(cos(Sphere_meshA(p,j,1)))>
abs(cos(Sphere_meshA(p,j,1)-pi/(Meshf-1)))
                          erf_m(p,j)=erp_A(   a*(   1-abs(  cos(
Sphere_meshA(p,j,1)- pi/(2*(Meshf-1))  )  )  +h(i)
)*abs(A22(Sphere_meshA(p,j,1)));
                         % BB(p,j)=
64*pi*er*e0*a*((K*T./e).^2)*tanh(e*zpA./(4*K*T))*tanh(e*zs./(4*K*T));
                         % erp(p,j)= erp_B(  a*  (  1-abs(  cos(
Sphere_meshA(p,j,1) - pi/(2*(Meshf-1))   )  )  +h(i)  );
                    else
                          erf_m(p,j)=erp_A(  a*(  1-abs(  cos(
Sphere_meshA(p,j,1)-  pi/(Meshf-1)  + pi/(2*(Meshf-1))  )  )   )
+h(i)  )*abs(A22(Sphere_meshA(p,j,1)));
                        %  BB(p,j)=
64*pi*er*e0*a*((K*T./e).^2)*tanh(e*zpA./(4*K*T))*tanh(e*zs./(4*K*T));
                         % erp(p,j)= erp_B(  a*  (  1-abs(  cos(
Sphere_meshA(p,j,1) - pi/(2*(Meshf-1))   )  )  +h(i)  );
                    end

            else
              %%%%  erf_m(p,j)=erp_B(a*(1-
cos(Sphere_meshA(p,j,1)))+h(i))*abs(-
cos(Sphere_meshA(p,j,1))*Sphere_meshA(p,j,3));%%%%%%%abs(-
cos(Sphere_meshA(p,j,1))*a^2*(pi/100)^2*(sin(Sphere_meshA(p,j,1))));
%%%abs(-
cos(Sphere_meshA(p,j,1))*a^2*(pi/100)*(cos(Sphere_meshA(p,j,1)+pi/200
)-cos(Sphere_meshA(p,j,1)-pi/200)));

                   if  abs(cos(Sphere_meshA(p,j,1)))>
abs(cos(Sphere_meshA(p,j,1)-pi/(Meshf-1)))
                        erf_m(p,j)=erp_B(  a*  (  1-abs(  cos(
Sphere_meshA(p,j,1) - pi/(2*(Meshf-1))   )  )  +h(i)
)*abs(A22(Sphere_meshA(p,j,1)));
                         % BB(p,j)=
64*pi*er*e0*a*((K*T./e).^2)*tanh(e*zpB./(4*K*T))*tanh(e*zs./(4*K*T));
                        % erp(p,j)= erp_B(  a*  (  1-abs(  cos(
Sphere_meshA(p,j,1) - pi/(2*(Meshf-1))   )  )  +h(i)  );
                       else
                        erf_m(p,j)=erp_B(  a*(  1-abs(  cos(
Sphere_meshA(p,j,1) - pi/(2*(Meshf-1)) + pi/(2*(Meshf-1))  )  )  )
+h(i)  )*abs(A22(Sphere_meshA(p,j,1)));
                        % BB(p,j)=
64*pi*er*e0*a*((K*T./e).^2)*tanh(e*zpB./(4*K*T))*tanh(e*zs./(4*K*T));
                        % erp(p,j)= erp_B(  a*  (  1-abs(  cos(
Sphere_meshA(p,j,1) - pi/(2*(Meshf-1))   )  )  +h(i)  );
                   end

            end
        end
    end

    dlr(i)=sum(sum(erf_m));
    F(i)=sum(sum(erf_m))- Gg;

    h(i+1)=h(i)+dDdh(i)*dt+D(i)/(K*T)*F(i)*dt+H(i);
        %%%%% Teta Rotational Calculation %%%%%------------------
         variance_RT=2*DrTeta(i)*dt;
```

```
        RND_RT=sqrt(abs(variance_RT))*randn(1,1);
        GT(i)= RND_RT;
        Teta(i+1)=Teta(i)+GT(i);

    %%%%% Phi Rotational Calculation %%%%%-------------------
        variance_RP=2*DrPHI(i)*dt;
        RND_RP=sqrt(abs(variance_RP))*randn(1,1);
        GP(i)= RND_RP;
        PHI(i+1)=PHI(i)+GP(i);

    %%%%% ..................... %%%%%-------------------

    Sphere_meshA(:,:,1)=Sphere_meshA(:,:,1)+GT(i);
    Sphere_meshA(:,:,2)=Sphere_meshA(:,:,2)+GP(i);

 phi(i+1)= ((B*exp(-k*(h(i+1)))+ (Gg)*h(i+1)))/(K*T)- (phim);
 phi2(i+1)= ((exp(-k*(h(i+1)-Hm))-1))/(K*T*k)*Gg + Gg/(K*T)*((h(i+1)-
Hm));

hh(i+1)=1E9*h(i+1);
Intensity(i+1)=I0*exp(-Beta*hh(i+1));

end
 Intensity(1)=I0*exp(-Beta*h(1)*1E9);

%% Calculating Number of Observation according to the position of A
and B respect to the Surface

TetaC=TetaConversion( Teta , N );
qq1=histcounts2(TetaC,hh,[nTheta round(max(hh))]);
nTheta_half=nTheta/2;
Nof_B_down=sum(sum(qq1(1:nTheta_half,:)));
nTheta_half2=nTheta_half+1;
Nof_A_down=sum(sum(qq1(nTheta_half2:nTheta,:)));
```

APPENDIX 3.1

Image analysis code.

```
xC=getNumber("Enter x coordinate at center of ellipse [pixel]",1595);
yC=getNumber("Enter y coordinate at center of ellipse [pixel]",1264);
B=getNumber("Enter height of ellipse [pixel]",2073);
A=getNumber("Enter width of ellipse [pixel]",2670);
L=getNumber("Enter profile length [pixel]",85);
b=B/2;
a=A/2;
P=getNumber("Enter points along perimeter",1000);
xPIB=newArray(P);
yPIB=newArray(P);
xPOB=newArray(P);
yPOB=newArray(P);
xPIT=newArray(P);
yPIT=newArray(P);
xPOT=newArray(P);
yPOT=newArray(P);
fyT=newArray(1800);
pfyT=newArray(1800);
k=newArray(L);
for (i=1;i<P;i++){
        xPOT[i] = xC;
        yPOT[i] = yC;
```

```
                xPIT[i] = (xC-(a+L/2))+(2*a+L)*((i-1)/(P-2));
                yPIT[i] = -(pow((1-pow(((xPIT[i]-xC)/(a+L/2)),2))*pow((b+L/2),2),1/2))+yC;
                makeLine(xPOT[i], yPOT[i], xPIT[i], yPIT[i]);
                run("Plot Profile");
                Plot.getValues(xT, yT);
                j = 0;
                        for (k=0; k<(yT.length-2);k++){
                                fyT[k] = yT[k]+yT[k+1]+yT[k+2];
                                        if (fyT[k]>=510){
                                                pfyT[j] = fyT[k];
                                                setResult(""+i+"",j, pfyT[j]);
                                                j++;}}
        close();
}
saveAs("Results","C:\\Users\\6000459\\Desktop\\Research\\Students\\Lewis\\Cap thickness ms\\Raw and Processed Imaging Data\\Rashidi Algo\\Plot Values_S7_2.0A-sec_10nm_001.xls");
```

APPENDIX 4.1

MATLAB code to implement the Brownian dynamics simulation on two-layer coated Janus particle.

```
%  Aidin Rashidi - CSU
% Last Modified 05/21/2019
%~~~~~~THIS CODE REQUIRES USER-MADE FUNCTIONS~~~~~~
% function: TetaConv_mesh.m

rng('shuffle')
%%%   File Name Detection
%%%   Particle Size/Material/zpA/zpB/zs/Electrolit C/ N of
Iteration/Mesh/Date
%%%   6PS-50 10 50-1-240-101-110316

%%%% Middle height %%%%%%%%%%%%%%%%%%%%%%%%%%%%%%%%%%%%%%%%%%%%%%%%%%%
disp('Have you changed the file name')
string=input('If yes please enter "y" else enter "N" ');

if string ~= 'y'
    return
end

tic
clc;
clear all;

Meshf=101;          % Number of Meshes (Meshf * Meshf)

nTheta=90;

a=3E-6;            % Particle Radius [m]

N=4800000;           % Number of Iterations

dt=5E-3;           % delta t or time sequence [second]
zpA=-5E-3;         % Stern potential of particle A which we replace
with zeta potential [V]
zpB=-50E-3;        % Stern potential of particle B which we replace
with zeta potential [V]
zs= -50E-3  ;      % Stern potential of substrate which we replace
with zeta potential [V]
C=1E-3;            % Electrolyte concentration [Molar]
```

```
RohCap_1=4500;      % Cap Density (Kg/m^3) -  Gold = 19320  /  Silica
= 2650 / Chromium = 7200
RohCap_2=19320;     % Cap Density (Kg/m^3) -  Gold = 19320  /  Silica
= 2650 / Titanium = 4500
Cap_thick_1 = 2.5E-9;    % 2.5E-9;  % Inner layer
Cap_thick_2 = 10E-9;     % 37.5E-9; % Outer layer
%%
zp = -100E-3;       % Stern potential of particle which we replace
with zeta potential [V]

h0=20E-9;           % initial height [m]

K=1.38065*10.^-23; % 1.3806488E-23; % Boltzmann constant [J/K]
T= 298.15;          % Temperature [Kelvin]
Mu=  0.000887;      % Dynamic viscosity of water - µ - [N s/m^2]
Bins_N=500;

Rohp=1055;         % Particle Density(kg/m^3)
Rohf=991.57;       % 1000;        % Fluid Density(kg/m^3)

g=9.81;            % Specific gravity
NA=6.022E23;       % Avogadro's No.[1/mol]
e=1.602E-19;       % [colone]

z=1;
e0=8.854E-12;      % [colon^2/N/m^2] /// e=e0*er  e:dielectric
permittivity
er=78.304;         % Dielectric constant

D=zeros(N,1);          % Diffusion Coeifficient
DrTeta=zeros(N,1);     % Teta Diffusion Coeifficient
DrPHI=zeros(N,1);      % PHI Diffusion Coeifficient
dDdh=zeros(N,1);       % Derivative of the diffusion coeifficent
respect to height
h=zeros(N,1);          % height of the particle on the substrate [m]
Teta=zeros(N,1);       % Rotational Degree Function Teta
alpha=zeros(N,1);      % Degree for calculating Center of Mass
PHI=zeros(N,1);        % Rotational Degree Function PHI
hh=zeros(N,1);         % height of the particle on the substrate [nm]
F=zeros(N,1);          % Force on Particle ( Double Layer and
Gravitational Force )
H=zeros(N,1);          % Height Random Displacement
GT=zeros(N,1);         % Teta Rotationl Random Displacement
GP=zeros(N,1);         % PHI Rotationl Random Displacement
RNDH=zeros(N,1);
phi= zeros(N,1);       % potential energy
phi2= zeros(N,1);
Intensity= zeros(N,1);
torque_weight=zeros(N,1);
torque_sum_dlr=zeros(N,1);
Teta_Weight=zeros(N,1);
Teta_torque_weight=zeros(N,1);
Teta_torque_dlr=zeros(N,1);

MSD_h=zeros(N,1);

qq1_sum=zeros(nTheta,1);
hh_Theta_ave = zeros(nTheta,1);  % Average Height in each orientation
hh_Theta_prob_loc = zeros(nTheta,1);
```

```
hh_Theta_probable2 = zeros(nTheta,1);
hh_Theta_probable= zeros(nTheta,1);
hh_ave_sum= zeros(nTheta,1);     % Summation of the heights in each
individual orientation

Teta_A=zeros(Meshf,Meshf);    % Teta Location of A part of Janus
Particle
PHI_A=zeros(Meshf,Meshf);     % Phi Location of A part of Janus
Particle
Sphere_Area=zeros(100,100,3); % 3rd layer Area of particle in
99(teta)*199(phi) mesh scale - 1st layer A_Teta (ZA) - 2nd layer
A_Phi (ZB)
Sphere_meshA=zeros(Meshf,Meshf,3);
erf_m=zeros(Meshf,Meshf);     % electrostatic repulsion force in each
mesh
torque_edl=zeros(Meshf,Meshf);
%%
k=((2*1000*NA*e^2*C*z^2)/(e0*er*K*T))^0.5;  % Debye parameter [1/m]
ggg=1/k;  % Debye length [m]

I0=1;
Intensity(1)=I0;

Beta=1/83;            % Inverse decay length [1/nm] - incident angle
= 75 degree

B =
64*pi*er*e0*a*((K*T./e).^2)*tanh(e*zp./(4*K*T))*tanh(e*zs./(4*K*T));
% It is not valid for Janus Particle
% zp = atanh( B /tanh(e*zs./(4*K*T))/ 64/pi/er/e0/a/((K*T./e).^2))
*(4*K*T)/e

Weight_Cap_1 = ( 4/3*pi*(a+Cap_thick_1)^3 - 4/3*pi*a^3 )/2 *
(RohCap_1-Rohf) *9.81;   %  Weight of 1st layer Cap
Weight_Cap_2 = ( 4/3*pi*(a+Cap_thick_1+Cap_thick_2)^3 -
4/3*pi*(a+Cap_thick_1)^3 )/2 * (RohCap_2-Rohf) *9.81;   %  Weight of
1st layer Cap
Weight_Cap= Weight_Cap_1+Weight_Cap_2;
Gg=((4/3)*pi*a^3*(Rohp-Rohf)*9.81)+ Weight_Cap;      % Net Weight of
Particle
Gg_PS_hem=((4/3)*pi*a^3*(Rohp-Rohf)*9.81)/2;    % Net Weight of
Particle hemisphere core

Hm=(1/k)*log(k*B/Gg);                    % Calculating hm for Direct
Potential Calculation
phim= (B*exp(-k*(Hm))+ (Gg)*Hm) /(K*T);  % Calculating Potential for
Direct Potential Calculation
i=1;
h(1)=h0;

Teta_A0 =linspace(0,pi,Meshf);           % dividing zpA
PHI_A0 =linspace(0,pi,Meshf);            % dividing zpA
% PHI_A0 =linspace(pi/2,3*pi/2,Meshf);  % dividing zpA


Teta(1)=Teta_A0((Meshf-1)/2+1);          % Initial middle Position of
the Particle Respect to Substrate (zpA)
PHI(1)=PHI_A0((Meshf-1)/2+1);            % Initial middle Position of
the Particle Respect to Substrate (zpA)
```

```
%%% Teta_Area=linspace(pi/2,pi,51); % teta Area meshing {the lower
halfsphere is mentioned} (teta degree)
%%% Phi_Area=linspace(0,2*pi,101);  % Area meshing (phi degree)

 for i=1:Meshf
     Teta_A(i,:)=Teta_A0(i); %%%%(Teta_A0(i+1)+Teta_A0(i))/2;
 end

for i=1:Meshf
     PHI_A(:,i)=PHI_A0(i); %%%% ((PHI_A0(i+1)+PHI_A0(i))/2)';
 end

    ii=0;
    jj=0;

Sphere_meshA(:,:,1)= Teta_A;  % Theta degree
Sphere_meshA(:,:,2)= PHI_A;   % Phi degree

%%%% A11=@(teta_cal) a*pi/100*cos( asin( ( (sin(teta_cal+pi/200) )-
(sin(teta_cal-pi/200) ) )/2 ) );  %finding alpha for calculating
surface of part pf sphere
%%%% A22=@(teta_cal) A11(teta_cal)/2*a*pi/100*(
(sin(teta_cal+pi/200))    + (sin(teta_cal-pi/200))  );  % straight
calculation of surface

 %%%%% A22=@(teta_cal) a^2*(pi/50)*(cos(teta_cal+pi/100)-
cos(teta_cal-pi/100));  % Finding real sphere surface area

A22=@ (teta_cal) pi*a^2/(2*(Meshf-1))*abs(((sin(teta_cal))^2-
(sin(teta_cal-pi/(Meshf-1)))^2));  %%% Derjagun projected surface
area

%%%% A22=@(teta_cal) a^2*(pi/100)^2*(sin(teta_cal)); % Finding square
surface area

 % for p=2:201
  %      for j=2:201

  %           Sphere_meshA(p,j,3)=abs(A22(Sphere_meshA_temp));%%
abs(-sin(Sphere_meshA_temp-
pi/2)*a^2*(pi/100)^2*(sin(Sphere_meshA_temp))); %%%abs(-
sin(Sphere_meshA_temp-
pi/2)*a^2*(pi/100)*(cos(Sphere_meshA_temp+pi/200)-
cos(Sphere_meshA_temp-pi/200)));

  %   end
  % end

%%%%%%%%%%%%%%%%%%%
 F_Derjaguin= k*B*exp(-k*h0);
 erp_A = @(h)
64*1000*NA*C*(K*T)*tanh(e*zpA./(4*K*T))*tanh(e*zs./(4*K*T))*exp(-
k*h); % Electrostatic Repultion Pressure
 erp_B = @(h)
64*1000*NA*C*(K*T)*tanh(e*zpB./(4*K*T))*tanh(e*zs./(4*K*T))*exp(-
k*h); % Electrostatic Repultion Pressure
```

```
 hh_check=0;
%%
for i=1:N-1

    i


D(i)=K*T*((6*h(i)^2+2*a*h(i))/(6*h(i)^2+9*a*h(i)+2*a^2))/(6*pi*Mu*a);
%%%% [m^2/s]

  %%% DrTeta(i)= K*T/(8*pi*Mu*a^3)/(1+ (5/16)*(a/(a+h(i)))^3);  %%%%
[m/s] Ref[20]

  h_over_a=h(i)/a;
  if h_over_a <= 0.6
    DrTeta(i)= K*T/(8*pi*Mu*a^3)/(0.9641*(h(i)/a)^-0.1815);   %%%%
fitting and numerical method from Goldman (h/a) <= 0.6
  else
      if h_over_a > 0.6 && h_over_a  <=2
          DrTeta(i)= K*T/(8*pi*Mu*a^3)/(1.056*(h(i)/a)^-0.07286);
%%%% fitting and numerical method from Goldman 0.6 <(h/a) <= 2
      else
           DrTeta(i)= K*T/(8*pi*Mu*a^3)/(1);
      end
  end

  % DrTeta_test(i)= K*T/(8*pi*Mu*a^2)*(0.9641*(h(i)/a)^-0.1815);
  %%%%%%  DrPHI(i)= K*T/(8*pi*Mu*a^3)*(1-1/8*(a/(a+h(i)))^3-
3/256*(a/(a+h(i)))^8); %%%%  Ref[20]

  dDdh(i)=K*T/(6*pi*Mu*a)*((((2*a + 12*h(i))*(2*a^2 + 9*a*h(i) +
6*h(i)^2)) - ((6*h(i)^2 + 2*a*h(i))*(9*a + 12*h(i))))/(2*a^2 +
9*a*h(i) + 6*h(i)^2)^2);

  variance_H=2*D(i)*dt;
  H(i)=sqrt(abs(variance_H))*randn(1,1);  % Random displacement
calculations

  [Sphere_meshA(:,:,1)]=TetaConv_mesh( Sphere_meshA(:,:,1) , Meshf );
% Converting the Theta values to values inside of [0 2*pi]

    for p=2:Meshf
        for j=2:Meshf

            Sphere_meshA_temp=Sphere_meshA(p,j,1);

           if (  (   (pi/2<=Sphere_meshA_temp) &&
(Sphere_meshA_temp<3*pi/2)  ) || (   (-3*pi/2<Sphere_meshA_temp) &&
(Sphere_meshA_temp<-pi/2 )  )       )
              %%%
erf_m(p,j)=erp_A(a*(1+cos(Sphere_meshA_temp))+h(i))*abs(-
cos(Sphere_meshA_temp)*Sphere_meshA(p,j,3));%% abs(-
sin(Sphere_meshA_temp-pi/2)*a^2*(pi/100)^2*(sin(Sphere_meshA_temp)));
%%%abs(-sin(Sphere_meshA_temp-
pi/2)*a^2*(pi/100)*(cos(Sphere_meshA_temp+pi/2/200)-
cos(Sphere_meshA_temp-pi/200)));
                    if  abs(cos(Sphere_meshA_temp))>
abs(cos(Sphere_meshA_temp-pi/(Meshf-1))) %%% Region 1 & 3
counterclockwise
```

```
                        erf_m(p,j)=erp_A(   a*(   1-abs(  cos(
Sphere_meshA_temp- pi/(2*(Meshf-1))  )  )  +h(i)
)*abs(A22(Sphere_meshA_temp));
                       % BB(p,j)=
64*pi*er*e0*a*((K*T./e).^2)*tanh(e*zpA./(4*K*T))*tanh(e*zs./(4*K*T));
                        %%% erp(p,j)= erp_A(  a*  (  1-abs(  cos(
Sphere_meshA_temp - pi/(2*(Meshf-1))   )  )  +h(i)  );
                        torque_edl(p,j)=  - erf_m(p,j)* a * sin(
Sphere_meshA_temp- pi/(2*(Meshf-1))) * abs(sin(Sphere_meshA(p,j,2)));

                  else            %%% region 2&4 clockwise
                        erf_m(p,j)=erp_A(  a*(  1-abs(  cos(
Sphere_meshA_temp-  pi/(Meshf-1)  + pi/(2*(Meshf-1))  )  )   )  +h(i)
)*abs(A22(Sphere_meshA_temp));
                       %  BB(p,j)=
64*pi*er*e0*a*((K*T./e).^2)*tanh(e*zpA./(4*K*T))*tanh(e*zs./(4*K*T));
                        %%% erp(p,j)= erp_A(  a*  (  1-abs(  cos(
Sphere_meshA_temp - pi/(2*(Meshf-1))   )  )  +h(i)  );
                        torque_edl(p,j)= - erf_m(p,j)* a *
sin(Sphere_meshA_temp-  pi/(Meshf-1) + pi/(2*(Meshf-
1)))*abs(sin(Sphere_meshA(p,j,2)));
                  end

          else
            %%%%  erf_m(p,j)=erp_B(a*(1-
cos(Sphere_meshA_temp))+h(i))*abs(-
cos(Sphere_meshA_temp)*Sphere_meshA(p,j,3));%%%%%%%abs(-
cos(Sphere_meshA_temp)*a^2*(pi/100)^2*(sin(Sphere_meshA_temp)));
%%%abs(-
cos(Sphere_meshA_temp)*a^2*(pi/100)*(cos(Sphere_meshA_temp+pi/200)-
cos(Sphere_meshA_temp-pi/200)));

                 if  abs(cos(Sphere_meshA_temp))>
abs(cos(Sphere_meshA_temp-pi/(Meshf-1)))  %%% Region 1 & 3
counterclockwise
                     erf_m(p,j)=erp_B(  a*  (  1-abs(  cos(
Sphere_meshA_temp - pi/(2*(Meshf-1))   )  )  +h(i)
)*abs(A22(Sphere_meshA_temp));
                      % BB(p,j)=
64*pi*er*e0*a*((K*T./e).^2)*tanh(e*zpB./(4*K*T))*tanh(e*zs./(4*K*T));
                      %%% erp(p,j)= erp_B(  a*  (  1-abs(  cos(
Sphere_meshA_temp - pi/(2*(Meshf-1))   )  )  +h(i)  );
                      torque_edl(p,j)=   - erf_m(p,j)* a*
sin(Sphere_meshA_temp+ pi - Sphere_meshA_temp - pi/(2*(Meshf-1))
)*abs(sin(Sphere_meshA(p,j,2)));
                 else   %%% region 2&4 clockwise
                     erf_m(p,j)=erp_B(  a*(  1-abs(  cos(
Sphere_meshA_temp - pi/(Meshf-1) + pi/(2*(Meshf-1))  )  )  )   +h(i)
)*abs(A22(Sphere_meshA_temp));
                     % BB(p,j)=
64*pi*er*e0*a*((K*T./e).^2)*tanh(e*zpB./(4*K*T))*tanh(e*zs./(4*K*T));
                     %%% erp(p,j)= erp_B(  a*  (  1-abs(  cos(
Sphere_meshA_temp - pi/(2*(Meshf-1))   )  )  +h(i)  );
                     torque_edl(p,j)=  - erf_m(p,j)*a* sin(
Sphere_meshA_temp+ pi - pi/(Meshf-1) + pi/(2*(Meshf-1))
)*abs(sin(Sphere_meshA(p,j,2)));
                 end
          end
        end
    end
```

```
    % dlr(i)=sum(sum(erf_m));
    torque_sum_dlr(i)=sum(sum(torque_edl));
    F(i)=sum(sum(erf_m))- Gg;

    h(i+1)=h(i)+dDdh(i)*dt+D(i)/(K*T)*F(i)*dt+H(i);

     while h(i+1) < 0
       hh_check=hh_check+1;
       i_value(hh_check)= i;
       H(i)=sqrt(abs(variance_H))*randn(1,1);  % Random displacement
calculations
       h(i+1)=h(i)+dDdh(i)*dt+D(i)/(K*T)*F(i)*dt+H(i);
    end

      %%%%%% Weight Calculation %%%%%%%%%
      Teta_Weight(i) = TetaConv_mesh( Teta(i) , 1 );
      Weight_percent= Teta_Weight(i)+pi/2;
      if Weight_percent >= pi
        Weight_percent = abs (Weight_percent-(2*pi));
      end
       Weight_percent = Weight_percent/pi;

      Weight_R = 2/3*pi*a^3*(Rohp-Rohf) * 9.81 + Weight_Cap *
Weight_percent ;
      Weight_L = 2/3*pi*a^3*(Rohp-Rohf) * 9.81 + Weight_Cap * (1 -
Weight_percent) ;

      ConvertedTeta=Teta_Weight(i);
      if ConvertedTeta>0 && ConvertedTeta<=pi/2
         alpha(i) = ConvertedTeta;
      elseif ConvertedTeta>pi/2 && ConvertedTeta<=3*pi/2
         alpha(i) = abs(pi-ConvertedTeta);
      else
         alpha(i) = abs(ConvertedTeta-2*pi);
      end

      Weight_R_Cap =  Weight_Cap * Weight_percent ;
      Weight_L_Cap =  Weight_Cap * (1 - Weight_percent) ;
      weight_2alpha= Weight_R_Cap - Weight_L_Cap;

      CM = 2*(a+Cap_thick_1+Cap_thick_2/2)/pi*  ( alpha(i) /2 + (
sin(2*alpha(i) )/4 ) )   /sin(alpha(i) );
      if CM > a || CM < -a
          CM=a;
      end

      torque_weight(i) = weight_2alpha * CM ;

      Teta_torque_weight(i)= DrTeta(i)*dt* torque_weight(i)/(K*T);

% % % % Weight_Cap_1 = ( 4/3*pi*(a+Cap_thick_1)^3 - 4/3*pi*a^3 )/2 *
(RohCap_1-Rohf) *9.81;   %  Weight of 1st layer Cap
% % % % Weight_Cap_2 = ( 4/3*pi*(a+Cap_thick_1+Cap_thick_2)^3 -
4/3*pi*(a+Cap_thick_1)^3 )/2 * (RohCap_2-Rohf) *9.81;   %  Weight of
1st layer Cap
% % % % Weight_Cap= Weight_Cap_1+Weight_Cap_2;
% % % % Gg=((4/3)*pi*a^3*(Rohp-Rohf)*9.81)+ Weight_Cap;      % Net
Weight of Particle
```

```
% % % % Gg_PS_hem=((4/3)*pi*a^3*(Rohp-Rohf)*9.81)/2;     % Net Weight
of Particle hemisphere core

      %%%%% Teta Rotational Calculation %%%%%-------------------
         variance_RT=2*DrTeta(i)*dt;
         RND_RT=sqrt(abs(variance_RT))*randn(1,1);
         GT(i)= RND_RT;
         Teta_torque_dlr(i)= DrTeta(i)*dt* torque_sum_dlr(i)/(K*T);

         Teta(i+1)=Teta(i)+DrTeta(i)*dt*
torque_weight(i)/(K*T)+DrTeta(i)*dt* torque_sum_dlr(i)/(K*T)+GT(i);
         %%%%% Phi Rotational Calculation %%%%%-------------------
         variance_RP=2*DrPHI(i)*dt;
         RND_RP=sqrt(abs(variance_RP))*randn(1,1);
         GP(i)= RND_RP;
         PHI(i+1)=PHI(i)+GP(i);

    %%%%% ..................... %%%%%-------------------


Sphere_meshA(:,:,1)=Sphere_meshA(:,:,1)+Teta_torque_weight(i)+Teta_to
rque_dlr(i)+GT(i);
    % Sphere_meshA(:,:,2)=Sphere_meshA(:,:,2)+GP(i);

 phi(i+1)= ((B*exp(-k*(h(i+1)))+ (Gg)*h(i+1)))/(K*T)- (phim);
 phi2(i+1)= ((exp(-k*(h(i+1)-Hm))-1))/(K*T*k)*Gg + Gg/(K*T)*((h(i+1)-
Hm));

%  for p=2:Meshf
%         for j=2:Meshf
%            erf_weight(p-1,j-1)= erf_m(p,j)/dlr(i);
%            BB_effective(p-1,j-1)=BB(p,j)*erf_weight(p-1,j-1);
%         end
%     end
%
%   BB_mean = sum(sum(BB_effective));

hh(i+1)=1E9*h(i+1);
Intensity(i+1)=I0*exp(-Beta*hh(i+1));

end
 Intensity(1)=I0*exp(-Beta*h(1)*1E9);

%% Calculating Number of Observation according to the position of A
and B respect to the Surface

TetaC=TetaConversion( Teta , N );
qq1=histcounts2(TetaC,hh,[nTheta round(max(hh))]);
nTheta_half=nTheta/2;
Nof_B_down=sum(sum(qq1(1:nTheta_half,:)));
nTheta_half2=nTheta_half+1;
Nof_A_down=sum(sum(qq1(nTheta_half2:nTheta,:)));
```

APPENDIX 5.1

MATLAB code to track spherical particle in a TIRM system and calculate scattered light integration

```
%<<<<<IMPORTANT POINT>>>>>>>>>
%<<<< THE X AND Y POSITION IN ImageJ OR FijiJ MUST BE INVERT IN
MATLAB
%CALCULATIONS---- row(MATLAB) = Y in ImageJ & column(MATLAB) = X in
ImageJ
% Modifid on 05/05/2019
% Code developer: Aidin Rashidi
clear all;clc;

double TotalIntensity;
double Background;
i=1;
j=1;
Beta= 0.0044;
%% Reading vsi or btif files
FileTif_VSI='Movie_JY_149.btf';
InfoImage=imfinfo(FileTif_VSI);
X_Image=InfoImage(1).Width;
Y_Image=InfoImage(1).Height;
NumberImages=length(InfoImage);

t=zeros(1,1000);
PixelLimit=20;  % This number represent the pixels which should be
counted as part of Moon Area.
FrameArea=0;   % This number represent the Number of pixels which are
involved in the Moon Area.
TotalIntensity=0;
MoonFrameArea=0;
%%

 % row(MATLAB) = Y in ImageJ & column(MATLAB) = X in ImageJ

% vid = VideoReader('Aidin_044.avi'); % Reading the file (should be
the target video file)

Intensity=zeros(NumberImages,1);
MSD_X=zeros(NumberImages,1) ;
MSD_Y=zeros(NumberImages,1) ;
MSD_R=zeros(NumberImages,1) ;
Lagtime=zeros(NumberImages,1) ;

qq=0;
```

```
%% Provide boundary for the Background
rr1=25;
rr2=25;
cc1=25;
cc2=25;
%% ------------------------------------------------------------
sss=0;
max_check=1;

for iFrame = 1:NumberImages

    iFrame

% % %   selectedframe= FinalImage(:,:,iFrame);
  selectedframe=imread(FileTif_VSI,'Index',iFrame);
  selectedframe = double(selectedframe);
  [Frame_Y_Size, Frame_X_Size] = size(selectedframe);
  FrameSize=Frame_Y_Size*Frame_X_Size;
  maximum=max(max(selectedframe)); %Finding center of the particle in
the selected file
  [rowM,columnM]=find(selectedframe==maximum);% finding index of
maximum pixel value in the selected file - y=rowM,x=columnM
   % PixelLimit= 0.2*maximum;

    SizeofMaximum=size([rowM,columnM]);          % If the maximum
ocupies more than
                                        %  one pixel, we will set the
Row and Column in one pixel

  if (SizeofMaximum(1,1)>1)
    RCofM=[rowM,columnM];
    RowofMax=ceil((SizeofMaximum(1,1)/2));
    rowM = RCofM(RowofMax,1);
    columnM = RCofM(RowofMax,2);
  end

  SizeofMaximum=size([rowM,columnM]);          % If the maximum
ocupies more than
                                        %  one pixel, we will set the
Row and Column in one pixel

      if iFrame>1
        max_check= abs(columnM+ rowM-columnM_old-rowM_old );
      end

if max_check<10
     rowM_old=rowM;
     columnM_old=columnM;

                                        if rowM <rr1 + 10
                                            rowM = rowM + rr1+10;
                                            sss=sss+1;
                                        end

                                         if  rowM > Frame_Y_Size -rr1
-10

                                             rowM = rowM - rr1-10;
                                            sss=sss+1;
                                         end
```

```
                                        if columnM <cc1 + 10
                                           ColumnM = columnM +
cc1+10;
                                           sss=sss+1;
                                       end

                                        if  columnM > Frame_X_Size -
cc1 -10
                                            columnM = columnM - cc1-
10;
                                           sss=sss+1;
                                        end


  %% Background
  % row(MATLAB) = Y in ImageJ & column(MATLAB) = X in ImageJ
 Background=0;

  for i=columnM-cc1 : -1:columnM-cc1-4
     Background=Background+double(selectedframe(rowM,i));
      % Calculation Background intensity in 4 loop in 4 different
direction
 end

 for i=columnM+cc2 : +1:columnM+cc2+4
     Background=Background+double(selectedframe(rowM,i));
 end


 for j=rowM-rr1 :-1: rowM-rr1-4
     Background=Background+double(selectedframe(j,columnM));
 end

% j=rowM+15;
 for j=rowM+rr2 :+1: rowM+rr2+4  %j=rowM+30 :+1: rowM+39
    Background=Background+double(selectedframe(j,columnM));
 end

    Background=Background/20;
    PixelLimit = 2*Background;
%%

  PixelValue = maximum;
  %formerPV = maximum;
  xm1=columnM;

while(PixelValue>PixelLimit)%# && PixelValue<=formerPV)# %Finding the
up and down pixel Boundary for intensity calculation in each frame
       %formerPV=PixelValue;
    xm1=xm1-1;
    if (xm1<1)
        break
    end

    PixelValue=selectedframe(rowM,xm1);
end
    xm1=xm1+1;
```

```
    PixelValue = maximum;
    xm2=columnM;
    while(PixelValue>PixelLimit)%### && PixelValue<=formerPV)
      xm2=xm2+1;
      if (xm2>Frame_X_Size)
          break
      end
      PixelValue=selectedframe(rowM,xm2);
    end
      xm2=xm2-1;

    PixelValue = maximum;
    ym1=rowM;
while(PixelValue>PixelLimit) %## && PixelValue<=formerPV)
     ym1=ym1-1;
     if (ym1<1)
         break
     end
     PixelValue=selectedframe(ym1,columnM);
end
  ym1=ym1+1;

    PixelValue = maximum;
    ym2=rowM;
while(PixelValue>PixelLimit) %### && PixelValue<=formerPV)
     ym2=ym2+1;
     if (ym2>Frame_Y_Size)
          break
      end
     PixelValue=selectedframe(ym2,columnM);
end
    ym2=ym2-1;

 Intensity=0;
 FrameArea=0;

for j=xm1 : xm2
for i=ym1 : ym2
          NewPixelValue=selectedframe(i,j);

             if (NewPixelValue > PixelLimit)
                 FrameArea=FrameArea+1;
                 Intensity= Intensity+ NewPixelValue;
             end
end
end

Intensity_Check=0;
ab_new=0;
ab_old=10000000;
for j=xm1 : xm2
     for i=ym1 : ym2
       Intensity_Check= Intensity_Check + double(selectedframe(i,j));
       ab_new=selectedframe(i,j);
       if ab_new < ab_old
           ab_old=ab_new;
       end
     end
end
```

```
    Intensity_Value_min=ab_old;

   % TotalIntensity(iFrame)=Intensity- FrameArea *
Intensity_Value_min;
    TotalIntensity(iFrame)=Intensity- FrameArea*Background;
    TotalIntensity_Check(iFrame)= Intensity_Check - double(((xm1-
xm2+1)*(ym1-ym2+1))* Intensity_Value_min);

    MoonFrameArea(iFrame)=FrameArea;
end

    if max_check>10
        TotalIntensity(iFrame)=0;
    end

end

TotalIntensity=TotalIntensity';

figure
plot(1:NumberImages, TotalIntensity);

title ('Scattering Intensity over time')
xlabel('Frame Number @30fps')
ylabel('Scattering Intensity')
```

APPENDIX 5.2

MATLAB code to find the directionality and AR of scattered light by 2D gaussian function

```
%% Fit a 2D gaussian function to data

%% PURPOSE:  Fit a 2D gaussian centroid to simulated data
% Uses lsqcurvefit to fit
%
% INPUT:
%
%   MdataSize: Size of nxn data matrix
%   x0 = [Amp,x0,wx,y0,wy,fi]: Inital guess parameters
%   x = [Amp,x0,wx,y0,wy,fi]: simulated centroid parameters
%   noise: noise in % of centroid peak value (x(1)
%   InterpolationMethod = 'nearest' or 'linear' or 'spline' or
'cubic'
%       used to calculate cross-section along minor and major axis
%
%
%
% NOTE:
%   The initial values in x0 must be close to x in order for the fit
%   to converge to the values of x (especially if noise is added)
%
% OUTPUT:  non
%
% CREATED: G. Nootz  May 2012
%
%  Modifications:
%  Sergio Dominguez Medina February 2020
clear all
close all
%% ---------User Input----------------------
%Input simulation file
%frame = imread('C:\Users\Lydia\Desktop\MyDrive\EW
Simulation\Simulations\012320\012320_08.tif','Index',1);
 %% Read tiff format
FileTif_VSI='030520_18.tif';                %          tif RGB
InfoImage=imfinfo(FileTif_VSI);             %          tif RGB
X_Image=InfoImage(1).Width;                 %          tif RGB
Y_Image=InfoImage(1).Height;                %          tif RGB
NumberImages=length(InfoImage);             %          tif RGB
particle=imread(FileTif_VSI,'Index',1);     %          tif RGB
grayimage = particle;
 % grayimage = rgb2gray(particle);          %          tif RGB
 frame=double(grayimage);
 mesh(grayimage)
```

```
  %%  Read Jpeg format
% particle = imread('1580.jpg'); %         JPEG RGB
% grayimage = rgb2gray(particle); %                JPEG RGB
% grayimage=double(grayimage);
% frame=double(grayimage);
 %% --------------------------------
zdata=frame; %double(rgb2gray(frame)); %Converting RGB simulation
image to grayscale
MdataSize = length(zdata); % Size of nxn data matrix

%This is to clean the borders of the simulation image
for i=1:MdataSize
zdata(1,i)=0;
zdata(i,MdataSize)=0;
zdata(i,1)=0;
end

%Initial guesses for the 2D-Gaussian fit are imported directly from
the simulation
%image
Amplitude = max(max(zdata));
[y0,xi0] = find(zdata==Amplitude);
y0 = median(y0);
xi0 = median(xi0);
sigmax = 5;
sigmay = 5;
angle =1;

% parameters are: [Amplitude, x0, sigmax, y0, sigmay, angel(in rad)]
%x0 = [255,175,5,137,5,0.5]; %Inital guess parameters
%x0 = [255,175,5,118,5,0.5]; %Inital guess parameters

%Initial guesses for the 2D-Gaussian fit
x0 = [Amplitude, xi0, sigmax, y0, sigmay, angle];
x = 0; %[2,2.2,7,3.4,4.5,+0.02*2*pi]; %centroid parameters
noise = 0; %10; % noise in % of centroid peak value (x(1))
InterpolationMethod = 'nearest'; %
'nearest','linear','spline','cubic'
FitForOrientation = 0; % 0: fit for orientation. 1: do not fit for
orientation

%% ---Generate centroid to be fitted--------------------------------
-----
xin = x;
noise = noise/100 * x(1);
x=[1:1:MdataSize];
y=[1:1:MdataSize];
[X,Y] = meshgrid(x,y); %meshgrid(-MdataSize/2:MdataSize/2); where x
and y a vectors with your x an y axis points
xdata = zeros(size(X,1),size(Y,2),2);
xdata(:,:,1) = X;
xdata(:,:,2) = Y;
%[Xhr,Yhr] = meshgrid(linspace(-MdataSize/2,MdataSize/2,300)); %
generate high res grid for plot
%[Xhr,Yhr] = meshgrid(linspace(1,MdataSize,300)); % generate high res
grid for plot
[Xhr,Yhr]= meshgrid(linspace(1,MdataSize,MdataSize));
%xdatahr = zeros(300,300,2);
xdatahr = zeros(MdataSize,MdataSize,2);
xdatahr(:,:,1) = Xhr;
```

```
xdatahr(:,:,2) = Yhr;
%---Generate noisy centroid---------------------
% frame = imread('C:\Users\Lydia\Desktop\MyDrive\EW
Simulation\Simulations\012320\012320_07.tif','Index',1);
% zdata=double(rgb2gray(frame));
% for i=1:MdataSize
% zdata(1,i)=0;
% zdata(i,MdataSize)=0;
% zdata(i,1)=0;
% end
Z = zdata; %where zdata is a length(x) by length(y) matrix with the
data you wish to fit such that zdata(i,j)=z(x_i,y_j).
%Z=Z;
%Z = Z + noise*(rand(size(X,1),size(Y,2))-0.5);

%% --- Fit----------------------
if FitForOrientation == 0
    % define lower and upper bounds [Amp,xo,wx,yo,wy,fi]
    %lb = [0,-MdataSize/2,0,-MdataSize/2,0,-pi/4];
    lb = [0,1,1,1,1,-pi];
    %ub =
[realmax('double'),MdataSize/2,(MdataSize/2)^2,MdataSize/2,(MdataSize
/2)^2,pi/4];
    ub = [255,344,344/10,344,344/10,pi];
    [x,resnorm,residual,exitflag] =
lsqcurvefit(@D2GaussFunctionRot,x0,xdata,Z,lb,ub);
else
    x0 =x0(1:5);
    xin(6) = 0;
    x =x(1:5);
    lb = [0,-MdataSize/2,0,-MdataSize/2,0];
    ub =
[realmax('double'),MdataSize/2,(MdataSize/2)^2,MdataSize/2,(MdataSize
/2)^2];
    [x,resnorm,residual,exitflag] =
lsqcurvefit(@D2GaussFunction,x0,xdata,Z,lb,ub);
    x(6) = 0;
end

%% ---------Plot 3D Image-------------
figure(1)
C = del2(Z);
mesh(X,Y,Z,C) %plot data
hold on
surface(Xhr,Yhr,D2GaussFunctionRot(x,xdatahr),'EdgeColor','none')
%plot fit
%axis([-MdataSize/2-0.5 MdataSize/2+0.5 -MdataSize/2-0.5
MdataSize/2+0.5 -noise noise+x(1)])
alpha(0.2)
hold off

%% -----Plot profiles----------------
hf2 = figure(2);
%set(hf2, 'Position', [20 20 950 900])
alpha(0)
subplot(4,4, [5,6,7,9,10,11,13,14,15])
%imagesc(X(1,:),Y(:,1)',Z)
imagesc(X(1,:),Y(:,1)',Z)
%imagesc(Z);
%set(gca,'YDir','reverse')
```

```
axis image
colormap('default')

string1 = ['       Amplitude','    X-Coordinate', '    X-Width','
Y-Coordinate','    Y-Width','     Angle'];
%string2 = ['Set     ',num2str(xin(1), '% 100.3f'),'
',num2str(xin(2), '% 100.3f'),'         ',num2str(xin(3), '%
100.3f'),'          ',num2str(xin(4), '% 100.3f'),'
',num2str(xin(5), '% 100.3f'),'     ',num2str(xin(6), '% 100.3f')];
string3 = ['Fit      ',num2str(x(1), '% 100.3f'),'
',num2str(x(2), '% 100.3f'),'         ',num2str(x(3), '% 100.3f'),'
',num2str(x(4), '% 100.3f'),'        ',num2str(x(5), '% 100.3f'),'
',num2str(x(6), '% 100.3f')];

%text(-MdataSize/2*0.9,+MdataSize/2*1.15,string1,'Color','red')
text(10,MdataSize*1.10,string1,'Color','red')
%text(-MdataSize/2*0.9,+MdataSize/2*1.2,string2,'Color','red')
text(10,MdataSize*1.15,string3,'Color','red')
Result = [ x(3)  x(5) x(6)];
%% -----Calculate cross sections-------------
% generate points along horizontal axis
m = -tan(x(6));% Point slope formula
b = (-m*x(2) + x(4));
%xvh = -MdataSize/2:MdataSize/2;
xvh = 1:MdataSize;
yvh = xvh*m + b;
hPoints = interp2(X,Y,Z,xvh,yvh,InterpolationMethod);
% generate points along vertical axis
mrot = -m;
brot = (mrot*x(4) - x(2));
%yvv = -MdataSize/2:MdataSize/2;
yvv = 1:MdataSize;
xvv = yvv*mrot - brot;
vPoints = interp2(X,Y,Z,xvv,yvv,InterpolationMethod);

hold on % Indicate major and minor axis on plot

% % plot pints
% plot(xvh,yvh,'r.')
% plot(xvv,yvv,'g.')

% plot lines
plot([xvh(1) xvh(size(xvh))],[yvh(1) yvh(size(yvh))],'r')
plot([xvv(1) xvv(size(xvv))],[yvv(1) yvv(size(yvv))],'g')
xlim([1 MdataSize])
hold off
```

APPENDIX 5.3

In-house made MATLAB code to apply quadrant method on 4-binning images.

```
%  Aidin Rashidi - CSU

% Ellipsoid Mapping - Picture analysis - Quadrant Method
% 08/22/2019
% Last Modified 04/20/2019
% (y ~ row) - (x ~ Column)
% [Ycenter , Xcenter]
%~~~~~~THIS CODE REQUIRES USER-MADE FUNCTIONS~~~~~~
% function: choosemode.m
clear all
clc
% read the image
 %% Read tiff format
FileTif_VSI='1543_B2.tif';                  %          tif RGB
InfoImage=imfinfo(FileTif_VSI);             %          tif RGB
X_Image=InfoImage(1).Width;                 %          tif RGB
Y_Image=InfoImage(1).Height;                %          tif RGB
NumberImages=length(InfoImage);             %          tif RGB
particle=imread(FileTif_VSI,'Index',1);     %          tif RGB
grayimage = particle;
  grayimage = rgb2gray(particle);          %          tif RGB
 grayimage=double(grayimage);               %
%%  Read Jpeg format
% particle = imread('68_0576.jpg'); %         JPEG RGB
% grayimage = rgb2gray(particle); %               JPEG RGB
% grayimage=double(grayimage);
%% Read AVI format
% vid = VideoReader('Ellipse_0038-1.avi');   avi RGB
% particle = read(vid, 1);                   avi RGB
% grayimage = rgb2gray(particle);            avi RGB
% grayimage=double(grayimage);


%%
%convert the image to grayscale, extract relevant information

[Y_size,X_size] = size(grayimage); %index values [rows,columns]

Y_index_in=[1:1:Y_size];
X_index_in=[1:1:X_size];

maxintensity = max(max(grayimage)); %finds max intensity among the
rows and columns
[Y_max,X_max] = find(grayimage==maxintensity); %finds coordinates of
maximum intensities
```

```
%finding the center
Xcenter = choosemode(X_max); %see user function "choosemode.m"
[rrmax,~] = find(X_max==Xcenter); %find all values of y along this x
yprospect = Y_max(rrmax);
if rem(length(yprospect),2) == 0 %if number of prospective y's is
even
    sort(yprospect);
    middle = length(yprospect)/2;
    yavg = mean(yprospect);
    if middle < yavg
        Ycenter = yprospect(floor(middle));
    else
        Ycenter = yprospect(ceil(middle));
    end
else %if number of prospective y's is odd
    Ycenter = median(yprospect); %find the median value out of these
values
end

origin = [Ycenter , Xcenter]; % this is our new reference point from
the center of the scattering image
                              % xcenter and ycenter are based on the
real
                              % coordinate system but their nameing are
                              % difernt at MATLAB matrix syste.
fprintf('The center is at row %d, column %d, where the intensity
value is %d\n',Ycenter,Xcenter,grayimage(Ycenter,Xcenter));
  %% Background
  % row(MATLAB) = Y in ImageJ & column(MATLAB) = X in ImageJ
  % Provide boundary for the Background
%   rr1=5;
%   rr2=5;
%   cc1=5;
%   cc2=5;

  rr1=15;
  rr2=15;
  cc1=15;
  cc2=15;


 Background=0;
 BackGround_Num=0;

  for i=Xcenter-cc1 : -1:Xcenter-cc1-4
          Background=Background+double(grayimage(Ycenter,i));
          if double(grayimage(Ycenter,i)) > 0
              BackGround_Num=BackGround_Num+1;
          end
      % Calculation Background intensity in 4 loop in 4 different
direction
 end

 for i=Xcenter+cc2 : +1:Xcenter+cc2+4
     Background=Background+double(grayimage(Ycenter,i));
     if double(grayimage(Ycenter,i)) > 0
              BackGround_Num=BackGround_Num+1;
     end
 end
```

```
 for j=Ycenter-rr1 :-1: Ycenter-rr1-4
     Background=Background+double(grayimage(j,Xcenter));
     if double(grayimage(j,Xcenter)) > 0
               BackGround_Num=BackGround_Num+1;
     end
 end

% j=rowM+15;
 for j=Ycenter+rr2 :+1: Ycenter+rr2+4  %j=rowM+30 :+1: rowM+39
    Background=Background+double(grayimage(j,Xcenter));
    if double(grayimage(j,Xcenter)) > 0
               BackGround_Num=BackGround_Num+1;
    end
 end

 if BackGround_Num==0
     BackGround_Num=1;
 end
  Background=Background/BackGround_Num;
 % Background=7;
% % % wwww(1:FrameSize) = selectedframe;
% % % FrameSort = sort(wwww);
% % % Background_Limit = round(0.1*FrameSize);
% % % Background = mean (FrameSort(1:Background_Limit));
    PixelLimit = 1.5 * Background;
   % PixelLimit=20;
    %%
   Y_index_new = Ycenter - Y_index_in;  % Define new axis values
   X_index_new = X_index_in - Xcenter;  % Define new axis value
   %% Finding scatterd pixels - Scattered_Pixel_1 is all values in
the image which their pixel values are samller than Pixel_limit
                            % - Scattered_Pixel_2 is all values
before
                            % shadow or start of changing pixel value
trend
   Y_limit_Filter_1=0;    % Y index of scattered pixels
   X_limit_Filter_1=0;    % X index of scattered pixels

   for i=1:X_size    % Add 1st filter (Finding Valid pixels which are
bigger than pixel Limit)
   for j=1:Y_size    % Add 1st filter
            if grayimage(j,i) > PixelLimit
                Y_limit_Filter_1=Y_limit_Filter_1+1;
                X_limit_Filter_1=X_limit_Filter_1+1;
                pixel_index_X_Filter_1(X_limit_Filter_1) = i;     %
Finding index of valid scattered pixels after applying 1st Filter
                pixel_index_Y_Filter_1(Y_limit_Filter_1) = j;     %
Finding index of valid scattered pixels after applying 1st Filter
                Scattered_Pixel_Filter_1(j,i)= grayimage(j,i);
            end
   end
   end

    [Y_Bound_index,X_Bound_index]=size(Scattered_Pixel_Filter_1); %
Dimensiom of new pixel values including .....
                                                          % valid
pixels after applying 1st Filter (just bigger than the limit)

   Y_limit_Filter_2=0;
```

```
   X_limit_Filter_2=0;


   for j=1:1:Y_Bound_index    % Add 2nd_Right filter to find pixels
which are not in the shadow and decrease continiusly
            i=Xcenter+1;
            Scattered_Pixel_limit=Scattered_Pixel_Filter_1(j,i)+1;
            while i<X_Bound_index && Scattered_Pixel_limit >=
Scattered_Pixel_Filter_1(j,i)-1 && Scattered_Pixel_limit>PixelLimit
                Scattered_Pixel_Filter_2(j,i)=
Scattered_Pixel_Filter_1(j,i);
                Scattered_Pixel_limit=Scattered_Pixel_Filter_1(j,i);

                i=i+1;
            end
   end

   for j=1:1:Y_Bound_index    % Add 2nd_Right filter to find pixels
which are not in the shadow and decrease continiusly
            i=Xcenter-1;
            Scattered_Pixel_limit=Scattered_Pixel_Filter_1(j,i)+1;
            while Scattered_Pixel_limit >=
Scattered_Pixel_Filter_1(j,i)-1 && i>2 &&
Scattered_Pixel_limit>PixelLimit
                Scattered_Pixel_Filter_2(j,i)=
Scattered_Pixel_Filter_1(j,i);
                Scattered_Pixel_limit=Scattered_Pixel_Filter_1(j,i);

                i=i-1;
            end
   end

            j=Ycenter;    % Fill the pixels in the center and
perpendicular to it which was not counted in the 2nd Filter
            i=Xcenter;
            Scattered_Pixel_limit=Scattered_Pixel_Filter_1(j,i)+1;
            while Scattered_Pixel_limit >=
Scattered_Pixel_Filter_1(j,i)-1 && i>2 &&
Scattered_Pixel_limit>PixelLimit
                Scattered_Pixel_Filter_2(j,i)=
Scattered_Pixel_Filter_1(j,i);
                Scattered_Pixel_limit=Scattered_Pixel_Filter_1(j,i);

                j=j-1;
            end

            j=Ycenter;    % Fill the pixels in the center and
perpendicular to it which was not counted in the 2nd Filter
            i=Xcenter;
            Scattered_Pixel_limit=Scattered_Pixel_Filter_1(j,i)+1;
            while Scattered_Pixel_limit >=
Scattered_Pixel_Filter_1(j,i)-1 && i>2
                Scattered_Pixel_Filter_2(j,i)=
Scattered_Pixel_Filter_1(j,i);
                Scattered_Pixel_limit=Scattered_Pixel_Filter_1(j,i);

                if Scattered_Pixel_limit<PixelLimit || j+1
>Y_Bound_index
                    break
```

```
                end
                j=j+1;
            end

   [Y_Bound_index_2,X_Bound_index_2]=size(Scattered_Pixel_Filter_2);


  for i=1:1:X_Bound_index_2    % Add 2nd filter
            j=Ycenter+1;
            Scattered_Pixel_limit=Scattered_Pixel_Filter_2(j,i)+1;
            while j<Y_Bound_index_2 && Scattered_Pixel_limit >=
Scattered_Pixel_Filter_2(j,i)-1 &&
Scattered_Pixel_Filter_2(j,i)>PixelLimit
                Scattered_Pixel_2nd(j,i)=
Scattered_Pixel_Filter_2(j,i);
                Scattered_Pixel_limit=Scattered_Pixel_Filter_2(j,i);

                Y_limit_Filter_2=Y_limit_Filter_2+1;
                X_limit_Filter_2=X_limit_Filter_2+1;
                Index_X_Filter_2(X_limit_Filter_2) = i;     % Finding
index of valid scattered pixels
                Index_Y_Filter_2(Y_limit_Filter_2) = j;     % Finding
index of valid scattered pixels

                j=j+1;
            end
   end


   for i=1:1:X_Bound_index_2    % Add 2nd filter
            j=Ycenter-1;
            Scattered_Pixel_limit=Scattered_Pixel_Filter_2(j,i)+1;
            while Scattered_Pixel_limit >=
Scattered_Pixel_Filter_2(j,i)-1 && j>2 &&
Scattered_Pixel_Filter_2(j,i)>PixelLimit
                Scattered_Pixel_2nd(j,i)=
Scattered_Pixel_Filter_2(j,i);
                Scattered_Pixel_limit=Scattered_Pixel_Filter_2(j,i);

                Y_limit_Filter_2=Y_limit_Filter_2+1;
                X_limit_Filter_2=X_limit_Filter_2+1;
                Index_X_Filter_2(X_limit_Filter_2) = i;     % Finding
index of valid scattered pixels
                Index_Y_Filter_2(Y_limit_Filter_2) = j;     % Finding
index of valid scattered pixels

                j=j-1;
            end
   end

            j=Ycenter;    % define the center area
            i=Xcenter;
            Scattered_Pixel_limit=Scattered_Pixel_Filter_2(j,i)+1;
            while Scattered_Pixel_limit >=
Scattered_Pixel_Filter_2(j,i)-1 && i>2 &&
Scattered_Pixel_Filter_2(j,i)>PixelLimit
                Scattered_Pixel_2nd(j,i)=
Scattered_Pixel_Filter_2(j,i);
                Scattered_Pixel_limit=Scattered_Pixel_Filter_2(j,i);
```

```
                Y_limit_Filter_2=Y_limit_Filter_2+1;
                X_limit_Filter_2=X_limit_Filter_2+1;
                Index_X_Filter_2(X_limit_Filter_2) = i;      % Finding
index of valid scattered pixels
                Index_Y_Filter_2(Y_limit_Filter_2) = j;      % Finding
index of valid scattered pixels

                i=i-1;
            end

            j=Ycenter;    % define the center area
            i=Xcenter;
            Scattered_Pixel_limit=Scattered_Pixel_Filter_2(j,i)+1;
            while  i<=X_Bound_index_2 && Scattered_Pixel_limit >=
Scattered_Pixel_Filter_2(j,i)-1 &&
Scattered_Pixel_Filter_2(j,i)>PixelLimit
                Scattered_Pixel_2nd(j,i)=
Scattered_Pixel_Filter_2(j,i);
                Scattered_Pixel_limit=Scattered_Pixel_Filter_2(j,i);

                Y_limit_Filter_2=Y_limit_Filter_2+1;
                X_limit_Filter_2=X_limit_Filter_2+1;
                Index_X_Filter_2(X_limit_Filter_2) = i;      % Finding
index of valid scattered pixels
                Index_Y_Filter_2(Y_limit_Filter_2) = j;      % Finding
index of valid scattered pixels

                i=i+1;
            end

  % Total Intensity when there is no shadow ------------
 Intensity_1=0;

for j=1 : X_Bound_index
for i=1 : Y_Bound_index

     Intensity_1= Intensity_1+ Scattered_Pixel_Filter_1(i,j);

end
end
   % ---------------------------------------------

   % Total Intensity when there is no shadow ------------
 Intensity_NoShadow_2=0;

for j=1 : X_Bound_index_2
for i=1 : Y_Bound_index_2

     Intensity_NoShadow_2= Intensity_NoShadow_2+
Scattered_Pixel_Filter_2(i,j);

end
end
   % ---------------------------------------------


Pixel_modified_Shadow=modified_nonzero_matrix(Scattered_Pixel_Filter_
```

```
1);  % Find eliminate zero values of main matrix and shrinkage it
(Just based on Pixel_Limit)

Pixel_modified_NoShadow=modified_nonzero_matrix(Scattered_Pixel_2nd);
% Find eliminate zero values of main matrix and shrinkage it (Based
on Pixel_Limit and shadow)

%% Find pixel values perpendicular and horizontal to the center


   for i=1:1:X_Bound_index

       if Scattered_Pixel_Filter_1(Ycenter,i) > PixelLimit
           lower_X_bond=i;
           break
       end

   end

   for j=1:1:Y_Bound_index

       if Scattered_Pixel_Filter_1(j , Xcenter) > PixelLimit
           lower_Y_bond=j;
           break
       end

   end


   for k=lower_Y_bond:1:Y_Bound_index

    Pixel_Perpendicular(k)= Scattered_Pixel_Filter_1(k,Xcenter);
    k=k+1;

end

   for k=lower_X_bond:1:X_Bound_index

    Pixel_Horizontal(k)= Scattered_Pixel_Filter_1(Ycenter ,k);
    k=k+1;

   end

   %%  Calculate Pixel value distribution in Shadow Condition (All
data are considered and decreasing values are neglected)

   Index_X_new_Shadow = pixel_index_X_Filter_1 - Xcenter;  %
Calculating new index of scattered pixels
   Index_Y_new_Shadow = Ycenter - pixel_index_Y_Filter_1 ; %
Calculating new index of scattered pixels

   Scat_Shadow_1st=0;
   Scat_Shadow_2nd=0;
   Scat_Shadow_3rd=0;
   Scat_Shadow_4th=0;

   Intensity_Shadow_1st=0;
```

```
   Intensity_Shadow_2nd=0;
   Intensity_Shadow_3rd=0;
   Intensity_Shadow_4th=0;

    for i=1:X_limit_Filter_1

            if Index_X_new_Shadow(i) > 0 && Index_Y_new_Shadow(i) > 0
                Intensity_Shadow_1st= Intensity_Shadow_1st+
grayimage(Ycenter - Index_Y_new_Shadow(i) ,
Index_X_new_Shadow(i)+Xcenter ) - Background;
                Scat_Shadow_1st=Scat_Shadow_1st+1;
            end

            if Index_X_new_Shadow(i) < 0 && Index_Y_new_Shadow(i) > 0
                Intensity_Shadow_2nd= Intensity_Shadow_2nd+
grayimage(Ycenter - Index_Y_new_Shadow(i) ,
Index_X_new_Shadow(i)+Xcenter  ) - Background;
                Scat_Shadow_2nd=Scat_Shadow_2nd+1;
            end

            if Index_X_new_Shadow(i) < 0 && Index_Y_new_Shadow(i) < 0
                Intensity_Shadow_3rd= Intensity_Shadow_3rd+
grayimage(Ycenter - Index_Y_new_Shadow(i),
Index_X_new_Shadow(i)+Xcenter ) - Background;
                Scat_Shadow_3rd=Scat_Shadow_3rd+1;
            end

            if Index_X_new_Shadow(i) > 0 && Index_Y_new_Shadow(i) < 0
                Intensity_Shadow_4th= Intensity_Shadow_4th+
grayimage( Ycenter - Index_Y_new_Shadow(i) ,
Index_X_new_Shadow(i)+Xcenter ) - Background;
                Scat_Shadow_4th=Scat_Shadow_4th+1;
            end

    end

    Pixel_dist_axes_Shadow= [Scat_Shadow_1st Scat_Shadow_2nd
Scat_Shadow_3rd Scat_Shadow_4th];
    Pixel_dist_axes_Shadow_Total=sum(Pixel_dist_axes_Shadow);


Pixel_1st_Shadow_PC=Pixel_dist_axes_Shadow(1)/Pixel_dist_axes_Shadow_
Total*180;

Pixel_2nd_Shadow_PC=Pixel_dist_axes_Shadow(2)/Pixel_dist_axes_Shadow_
Total*180;

Pixel_3rd_Shadow_PC=Pixel_dist_axes_Shadow(3)/Pixel_dist_axes_Shadow_
Total*180;

Pixel_4th_Shadow_PC=Pixel_dist_axes_Shadow(4)/Pixel_dist_axes_Shadow_
Total*180;
    Pixel_PC_Shadow=[Pixel_1st_Shadow_PC Pixel_2nd_Shadow_PC
Pixel_3rd_Shadow_PC Pixel_4th_Shadow_PC];

    Intensity_Dis_Shadow= [Intensity_Shadow_1st Intensity_Shadow_2nd
Intensity_Shadow_3rd Intensity_Shadow_4th];
    max_Intensity_axes_Shadow=max(Intensity_Dis_Shadow);
```

```
    [section_max] =
find(Intensity_Dis_Shadow==max_Intensity_axes_Shadow); %finds index
(section) of maximum distribution


Intensity_1st_Shadow_PC=Intensity_Dis_Shadow(1)/sum(Intensity_Dis_Sha
dow)*180;

Intensity_2nd_Shadow_PC=Intensity_Dis_Shadow(2)/sum(Intensity_Dis_Sha
dow)*180;

Intensity_3rd_Shadow_PC=Intensity_Dis_Shadow(3)/sum(Intensity_Dis_Sha
dow)*180;

Intensity_4th_Shadow_PC=Intensity_Dis_Shadow(4)/sum(Intensity_Dis_Sha
dow)*180;
    Intensity_PC_Shadow=[Intensity_1st_Shadow_PC
Intensity_2nd_Shadow_PC Intensity_3rd_Shadow_PC
Intensity_4th_Shadow_PC];

    %%% New Method to Calculate SD (Shadow Degree) - Vector Method
    xx_Positive = Intensity_1st_Shadow_PC*cosd(45) +
Intensity_4th_Shadow_PC * cosd(45);
    xx_Negative = Intensity_2nd_Shadow_PC*cosd(45) +
Intensity_3rd_Shadow_PC * cosd(45);
    yy_Positive = Intensity_1st_Shadow_PC*sind(45) +
Intensity_2nd_Shadow_PC * sind(45);
    yy_Negative = Intensity_3rd_Shadow_PC*sind(45) +
Intensity_4th_Shadow_PC * sind(45);
    XX = xx_Positive - xx_Negative;
    YY = yy_Positive - yy_Negative;
    Phi = atand(XX / YY);

     if ( XX>0 && YY>0 ) || ( XX>0 && YY<0 )
         Scatter_degree_Shadow_New = Phi;

     elseif XX<0 && YY>0
         Scatter_degree_Shadow_New = 180 - Phi;
        elseif XX<0 && YY<0
         Scatter_degree_Shadow_New = 180 + Phi;
     end

    %%%


     if section_max==1
        % Scatter_degree_Shadow = 45 +  Intensity_2nd_Shadow_PC -
Intensity_4th_Shadow_PC;
         Scatter_degree_Shadow = 45 +  (Intensity_2nd_Shadow_PC -
Intensity_4th_Shadow_PC)*45/Intensity_1st_Shadow_PC;

         Int_Shadow_Opposit_Cover=
Intensity_3rd_Shadow_PC/Intensity_1st_Shadow_PC;

     end

     if section_max==2
         %Scatter_degree_Shadow = 135 +  Intensity_3rd_Shadow_PC -
Intensity_1st_Shadow_PC;
```

```
         Scatter_degree_Shadow = 135 +  (Intensity_3rd_Shadow_PC -
Intensity_1st_Shadow_PC)*45/Intensity_2nd_Shadow_PC;


Int_Shadow_Opposit_Cover=Intensity_4th_Shadow_PC/Intensity_2nd_Shadow
_PC;
     end

      if section_max==3
         %Scatter_degree_Shadow = 225 +  Intensity_4th_Shadow_PC -
Intensity_2nd_Shadow_PC;
         Scatter_degree_Shadow = 225 +  (Intensity_4th_Shadow_PC -
Intensity_2nd_Shadow_PC)*45/Intensity_3rd_Shadow_PC;


Int_Shadow_Opposit_Cover=Intensity_1st_Shadow_PC/Intensity_3rd_Shadow
_PC;
     end

      if section_max==4
         %Scatter_degree_Shadow = 315 +  Intensity_1st_Shadow_PC -
Intensity_3rd_Shadow_PC;
         Scatter_degree_Shadow = 315 +  (Intensity_1st_Shadow_PC -
Intensity_3rd_Shadow_PC)*45/Intensity_4th_Shadow_PC;


Int_Shadow_Opposit_Cover=Intensity_2nd_Shadow_PC/Intensity_4th_Shadow
_PC;
      end

      Intensity_Shadow_PC_Limit_STD= std(Intensity_PC_Shadow);
      Intensity_Total_Limit_Shadow=sum(Intensity_Dis_Shadow);
      Pixel_Shadow_PC_Limit_STD= std(Pixel_PC_Shadow);

Result=[Scatter_degree_Shadow,Intensity_PC_Shadow,Intensity_Shadow_PC
_Limit_STD,Intensity_Total_Limit_Shadow,Int_Shadow_Opposit_Cover,Pixe
l_PC_Shadow,Pixel_dist_axes_Shadow_Total,Pixel_Shadow_PC_Limit_STD,];
      www=0; % Main Results for Mapping
```

APPENDIX 6.1

Copyright permission for dissertation pages

Highly Stabilized Foam by Adding Amphiphilic Janus Particles for Drilling a High-Temperature and High-Calcium Geothermal Well

Author: Lili Yang, Tengda Wang, Xiao Yang, et al
Publication: Industrial & Engineering Chemistry Research
Publisher: American Chemical Society
Date: Jun 1, 2019

Bulk Synthesis of Metal–Organic Hybrid Dimers and Their Propulsion under Electric Fields

Author: Sijia Wang, Fuduo Ma, Hui Zhao, et al
Publication: Applied Materials
Publisher: American Chemical Society
Date: Mar 1, 2014

AIP PUBLISHING LICENSE
TERMS AND CONDITIONS

Apr 15, 2020

This Agreement between Mr. Aidin Rashidi ("You") and AIP Publishing ("AIP Publishing") consists of your license details and the terms and conditions provided by AIP Publishing and Copyright Clearance Center.

License Number	4810260854250
License date	Apr 15, 2020
Licensed Content Publisher	AIP Publishing
Licensed Content Publication	Journal of Chemical Physics
Licensed Content Title	Motion of a Janus particle very near a wall
Licensed Content Author	Aidin Rashidi, Christopher L. Wirth
Licensed Content Date	Dec 14, 2017
Licensed Content Volume	147
Licensed Content Issue	22
Type of Use	Thesis/Dissertation
Requestor type	Author (original article)
Format	Print and electronic
Portion	Excerpt (> 800 words)

Will you be translating?	No
Title	Mr.
Institution name	Cleveland State University
Expected presentation date	Apr 2020
Order reference number	https://doi.org/10.1063/1.4994843
Portions	Most part of the paper
Requestor Location	Mr. Aidin Rashidi 27693 remingtron drive WESTLAKE, OH 44145 United States Attn: Mr. Aidin Rashidi
Total	0.00 USD

Terms and Conditions

AIP Publishing -- Terms and Conditions: Permissions Uses

AIP Publishing hereby grants to you the non-exclusive right and license to use and/or distribute the Material according to the use specified in your order, on a one-time basis, for the specified term, with a maximum distribution equal to the number that you have ordered. Any links or other content accompanying the Material are not the subject of this license.

1. You agree to include the following copyright and permission notice with the reproduction of the Material:"Reprinted from [FULL CITATION], with the permission of AIP Publishing." For an article, the credit line and permission notice must be printed on the first page of the article or book chapter. For photographs, covers, or tables, the notice may appear with the Material, in a footnote, or in the reference list.
2. If you have licensed reuse of a figure, photograph, cover, or table, it is your responsibility to ensure that the material is original to AIP Publishing and does not contain the copyright of another entity, and that the copyright notice of the figure, photograph, cover, or table does not indicate that it was reprinted by AIP Publishing, with permission, from another source. Under no circumstances does AIP Publishing purport or intend to grant permission to reuse material to which it does not hold appropriate rights.
   You may not alter or modify the Material in any manner. You may translate the

Material into another language only if you have licensed translation rights. You may not use the Material for promotional purposes.

3. The foregoing license shall not take effect unless and until AIP Publishing or its agent, Copyright Clearance Center, receives the Payment in accordance with Copyright Clearance Center Billing and Payment Terms and Conditions, which are incorporated herein by reference.
4. AIP Publishing or Copyright Clearance Center may, within two business days of granting this license, revoke the license for any reason whatsoever, with a full refund payable to you. Should you violate the terms of this license at any time, AIP Publishing, or Copyright Clearance Center may revoke the license with no refund to you. Notice of such revocation will be made using the contact information provided by you. Failure to receive such notice will not nullify the revocation.
5. AIP Publishing makes no representations or warranties with respect to the Material. You agree to indemnify and hold harmless AIP Publishing, and their officers, directors, employees or agents from and against any and all claims arising out of your use of the Material other than as specifically authorized herein.
6. The permission granted herein is personal to you and is not transferable or assignable without the prior written permission of AIP Publishing. This license may not be amended except in a writing signed by the party to be charged.
7. If purchase orders, acknowledgments or check endorsements are issued on any forms containing terms and conditions which are inconsistent with these provisions, such inconsistent terms and conditions shall be of no force and effect. This document, including the CCC Billing and Payment Terms and Conditions, shall be the entire agreement between the parties relating to the subject matter hereof.

This Agreement shall be governed by and construed in accordance with the laws of the State of New York. Both parties hereby submit to the jurisdiction of the courts of New York County for purposes of resolving any disputes that may arise hereunder.

V1.2

Questions? customercare@copyright.com or +1-855-239-3415 (toll free in the US) or +1-978-646-2777.

Local Measurement of Janus Particle Cap Thickness

Author: Aidin Rashidi, Marola W. Issa, Ina T. Martin, et al
Publication: Applied Materials
Publisher: American Chemical Society
Date: Sep 1, 2018

PERMISSION/LICENSE IS GRANTED FOR YOUR ORDER AT NO CHARGE

This type of permission/license, instead of the standard Terms & Conditions, is sent to you because no fee is being charged for your order. Please note the following:

- Permission is granted for your request in both print and electronic formats, and translations.
- If figures and/or tables were requested, they may be adapted or used in part.
- Please print this page for your records and send a copy of it to your publisher/graduate school.
- Appropriate credit for the requested material should be given as follows: "Reprinted (adapted) with permission from (COMPLETE REFERENCE CITATION). Copyright (YEAR) American Chemical Society." Insert appropriate information in place of the capitalized words.
- One-time permission is granted only for the use specified in your request. No additional uses are granted (such as derivative works or other editions). For any other uses, please submit a new request.

BACK CLOSE WINDOW

American Physical Society
Reuse and Permissions License

29-Apr-2020

This license agreement between the American Physical Society ("APS") and Aidin Rashidi ("You") consists of your license details and the terms and conditions provided by the American Physical Society and SciPris.

Licensed Content Information

License Number:	**RNP/20/APR/025306**
License date:	29-Apr-2020
DOI:	10.1103/PhysRevE.101.042606
Title:	Influence of cap weight on the motion of a Janus particle very near a wall
Author:	Aidin Rashidi, Sepideh Razavi, and Christopher L. Wirth
Publication:	Physical Review E
Publisher:	American Physical Society
Cost:	USD $ 0.00

Request Details

Does your reuse require significant modifications: No

Specify intended distribution locations:	United States
Reuse Category:	Reuse in a thesis/dissertation
Requestor Type:	Author of requested content
Items for Reuse:	Whole Article
Format for Reuse:	Electronic and Print
Total number of print copies:	Up to 1000

Information about New Publication:

University/Publisher:	Cleveland state University
Title of dissertation/thesis:	Dynamics and surface forces experienced by an anisotropic particle near a boundary
Author(s):	
Expected completion date:	May. 2020

License Requestor Information

Name:	Aidin Rashidi
Affiliation:	Individual
Email Id:	aidin86@yahoo.com
Country:	United States

American Physical Society
Reuse and Permissions License

TERMS AND CONDITIONS

The American Physical Society (APS) is pleased to grant the Requestor of this license a non-exclusive, non-transferable permission, limited to Electronic and Print format, provided all criteria outlined below are followed.

1. You must also obtain permission from at least one of the lead authors for each separate work, if you haven't done so already. The author's name and affiliation can be found on the first page of the published Article.
2. For electronic format permissions, Requestor agrees to provide a hyperlink from the reprinted APS material using the source material's DOI on the web page where the work appears. The hyperlink should use the standard DOI resolution URL, http://dx.doi.org/{DOI}. The hyperlink may be embedded in the copyright credit line.
3. For print format permissions, Requestor agrees to print the required copyright credit line on the first page where the material appears: "Reprinted (abstract/excerpt/figure) with permission from [(FULL REFERENCE CITATION) as follows: Author's Names, APS Journal Title, Volume Number, Page Number and Year of Publication.] Copyright (YEAR) by the American Physical Society."
4. Permission granted in this license is for a one-time use and does not include permission for any future editions, updates, databases, formats or other matters. Permission must be sought for any additional use.
5. Use of the material does not and must not imply any endorsement by APS.
6. APS does not imply, purport or intend to grant permission to reuse materials to which it does not hold copyright. It is the requestor's sole responsibility to ensure the licensed material is original to APS and does not contain the copyright of another entity, and that the copyright notice of the figure, photograph, cover or table does not indicate it was reprinted by APS with permission from another source.
7. The permission granted herein is personal to the Requestor for the use specified and is not transferable or assignable without express written permission of APS. This license may not be amended except in writing by APS.
8. You may not alter, edit or modify the material in any manner.
9. You may translate the materials only when translation rights have been granted.
10. APS is not responsible for any errors or omissions due to translation.
11. You may not use the material for promotional, sales, advertising or marketing purposes.
12. The foregoing license shall not take effect unless and until APS or its agent, Aptara, receives payment in full in accordance with Aptara Billing and Payment Terms and Conditions, which are incorporated herein by reference.
13. Should the terms of this license be violated at any time, APS or Aptara may revoke the license with no refund to you and seek relief to the fullest extent of the laws of the USA. Official written notice will be made using the contact information provided with the permission request. Failure to receive such notice will not nullify revocation of the permission.
14. APS reserves all rights not specifically granted herein.
15. This document, including the Aptara Billing and Payment Terms and Conditions, shall be the entire agreement between the parties relating to the subject matter hereof.